FINAL TECHNICAL REPORT

AWARD NUMBER: G14AP00008

Magnitude Estimates for the 1811-1812 New Madrid Seismic Zone Earthquakes using Large Scale Numerical Simulations: Implications for the Seismic Hazard in Urban Areas around the Mississippi Embayment

Principal Investigator(s):

Mehrdad Hosseini, Paul Somerville, Andreas Skarlatoudis, and Jeff Bayless

URS Group, Inc.
915 Wilshire Boulevard
Los Angeles, CA 90017

April 5, 2016

"Research supported by the U.S. Geological Survey (USGS), Department of the Interior, under USGS award number G14AP00008. The views and conclusions contained in this document are those of the authors and should not be interpreted as necessarily representing the official policies, either expressed or implied, of the U.S. Government."

TABLE OF CONTENTS

1. Abstract

The earthquake magnitudes whose values range between 7.1 and 8.0 (Petersen et al., 2008), controlling ground motion levels in the New Madrid Seismic Zone have large uncertainties, and are based on controversial magnitude estimates of the 1811-1812 earthquakes in the region. Improvements in our knowledge of the historical sequence's magnitudes and associated ground motions, made using large scale simulations, offer an alternative to previous work on the seismic hazard at regional and city levels by reducing uncertainties associated with the ground motion variability.

This project had the objective of providing improved estimates of the magnitudes of the three main shocks of the sequence by using broadband simulations generated at sites with reported MMIs, and comparing MMI values derived from the simulations with the observed intensities. Our work builds on the work of Ramirez-Guzman et al. (2015), who used 3D simulations out to distances of about 500 km. We used 1D simulations out to 1,800 km to span the entire region over which MMI intensities were reported.

We used the Southern California Earthquake Center (SCEC) Broadband Simulation Platform (BBP) to perform the simulations. We used the Atkinson and Kaka (2007) and Dangkua and Cramer (2011) ground motion intensity correlation equations to estimate MMI from the ground motion simulations so that they could be compared with the observed intensities. We compared simulations of magnitude 7 earthquakes with simulations of larger events. For the larger magnitudes, the NM1 scenarios (December 16, 1811) had a magnitude of 7.7, the NM2 scenarios (January 23, 1812) had a magnitude of 7.4, and the NM3 scenarios (February 7, 1812) had a magnitude of 7.6. Although there is a large degree of discrepancy between the observed and simulated intensities, there is a slight preference for the larger magnitudes, which are systematically higher than those described by Hough and Page (2011) and comparable to those reported by Cramer and Boyd (2014).

The dispersion in the observed MMI intensity for NM3, the central thrust faulting event, is much larger in the distance range of 200 to 1200 km than it is for the two strike-slip events (NM1 and NM2). Despite this difference between the events in the observations, we do not see this difference between the events in our simulations. Similarly, we do not see evidence for this difference between NM3 and NM1 in the results of Ramirez-Guzman et al. (2015). We conclude that there may be factors influencing the observed MMI intensities of the three events that our simulations are not modeling.

2. Introduction

According to some authors (e.g. Johnston, 1996), the 1811-1812 earthquakes are among the largest events in any of the Stable Continental Regions (SCR) around the world, as defined by Kanter (1994). Moreover, based on geological evidence (Tuttle et al., 2002), the number of damage and felt accounts, and the extent of the large 1811-1812 sand blow field still visible today, support plausible scenarios of very strong shaking with an average recurrence rate of 500 years in the area. Reports of this sequence of earthquakes exist as far north as Canada, and they were documented extensively by the population of the East Coast of the United States. These reports, together with the extensive area of liquefaction, landslides, and changes in the geomorphology of the region, provide constraints for the study of the size of the three main earthquakes.

Several research groups have studied the magnitude of these earthquakes. Nuttli (1973) made the first magnitude estimates of the three main shocks, NM1 (December 16 1811), NM2 (January 23, 1812) and NM3 (February 7, 1812), whose suggested locations are displayed in Figure 1.

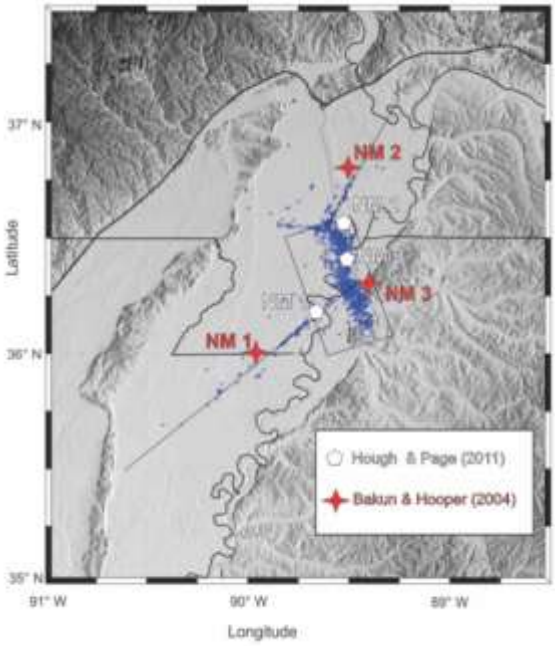

Figure 1. New Madrid Seismic Zone, showing the location of the 1811-1812 sequence mainshocks. Source: Ramirez-Guzman et al. (2015).

3. Reported Intensities

Nuttli's (1973) early assessments of m_{Lg} 7.1, 7.2 and 7.4 for NM1, NM2 and NM3, were based on the recorded ground motion of the November 9, 1968, Illinois earthquake and other earthquakes in eastern North America, together with the interpretation of newspaper reports of the severity of the earthquakes throughout the Central Eastern United States (CEUS) using Modified Mercalli Intensity (MMI) values. Later, Johnston (1996) obtained Mw values ranging from 7.8 to 8.1 based on an isoseismal approach to interpreting MMI. Following Johnston's (1996) method, Hough et al. (2000) re-examined the felt reports

and included a correction for site response. The analysis indicated lower magnitude values, from 7 to 7.5, for the mainshocks. Bakun and Hopper (2004), using the method of Bakun and Wentworth (1997) and Bakun et al. (2002) for MMI assignment, computed higher magnitudes, 7.5 to 7.8, than those reported by Hough et al. (2000). In contrast to the isoseismal approach, the method used by Bakun and Wentworth (1997) is based on individual intensity reports, which reduce the uncertainty of the estimation. More recently, Hough and Page (2011) re-evaluated the Bakun et al (2004) work using MMI values interpreted by four different experts using the attenuation models derived with the original Bakun and Hooper (2002) MMI assignment procedure. The mean magnitudes were substantially lower than any previous assessment, ranging from 6.8 to 7.2, which added to the debate about the seismic potential of the NMSZ.

We used the Hough and Page (2011) reported MMIs in this report. They reported intensities at 116 unique stations for the three events NM1, NM2, NM3. The intensities were interpreted by four experts. A list of these stations is provided in Table 1 and plotted in Figure 2. Observed intensities as reported by Hough and Page (2011) are plotted in Figure 3. The MMI calculated from the average of four experts' interpretations are used in this study, which is shown in the bottom row of Figure 3. Mueller et al. (2004) associated the three historic events with different branches of the New Madrid fault by studying the stress-field of different scenarios. Event NM1 is associated with the Cottonwood Grove fault, the southern segment of New Madrid fault striking northeast. Event NM3 is associated with the west-dipping Reelfoot fault, the central segment of the New Madrid fault. Location of NM2 is not certain as it is associated with the northern segment of New Madrid fault and also with an area outside of the NMSZ (Mueller et al. 2004). The three branches of the New Madrid fault are shown in Figures 2 and 9, and their relevant information is provided in Table 2.

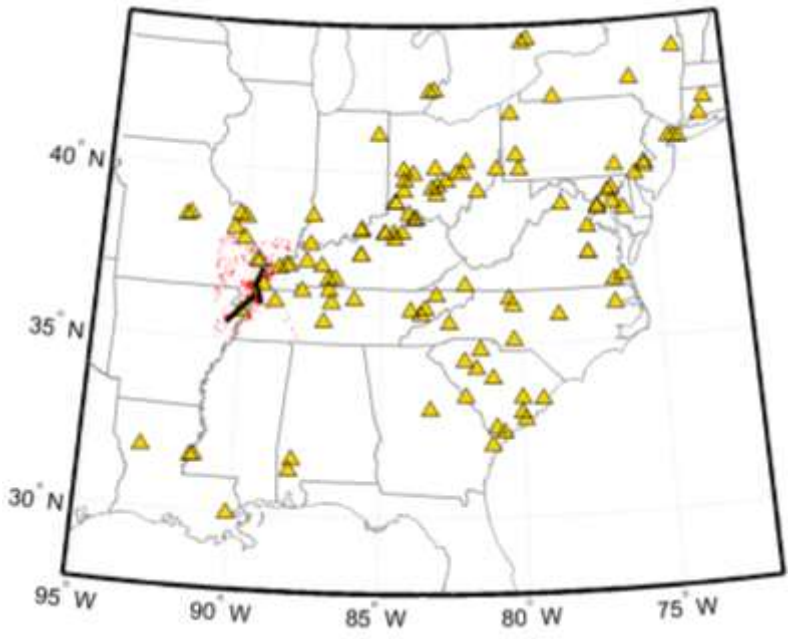

Figure 2. Stations (triangles) with MMI reported by Hough and Page (2011). Seismicity in the New Madrid Zone is shown with red dots. Solid lines show the hypothetical location of New Madrid fault.

Table 1. List of unique stations with reported intensity.

No	Longitude ^{0}	Latitude ^{0}	Vs30 (m/s)	No	Longitude ^{0}	Latitude ^{0}	Vs30 (m/s)	No	Longitude ^{0}	Latitude ^{0}	Vs30 (m/s)	No	Longitude ^{0}	Latitude ^{0}	Vs30 (m/s)
1	-72.69	41.76	224	31	-79.89	40.02	396	61	-83.15	39.51	278	91	-87.04	35.62	386
2	-72.93	41.3	267	32	-79.94	32.8	242	62	-83.24	33.09	317	92	-87.15	37.22	292
3	-73.71	43.32	280	33	-79.98	40.44	476	63	-83.24	42.31	191	93	-87.53	38.68	214
4	-73.81	40.69	228	34	-80.03	33.43	223	64	-83.42	36.02	396	94	-87.59	37.84	332
5	-74	40.73	238	35	-80.05	33	205	65	-83.57	35.87	359	95	-87.7	37.35	284
6	-74.17	40.74	325	36	-80.14	41.65	509	66	-83.74	38.64	475	96	-87.84	36.49	375
7	-75.16	39.95	266	37	-80.26	35.1	337	67	-83.81	38.61	187	97	-87.98	31.6	339
8	-75.18	40.04	303	38	-80.26	36.1	337	68	-83.84	39.93	279	98	-88.05	31.27	205
9	-75.49	42.51	501	39	-80.4	36.3	347	69	-83.92	35.98	289	99	-88.33	37.22	399
10	-75.55	39.75	364	40	-80.67	32.43	243	70	-84	38.77	403	100	-88.45	37.22	355
11	-76.08	38.77	252	41	-80.72	40.06	405	71	-84.19	39.74	360	101	-88.69	37.14	290
12	-76.28	36.85	225	42	-80.94	32.59	263	72	-84.2	40.04	207	102	-88.79	36.16	246
13	-76.3	40.04	308	43	-81.04	34	373	73	-84.21	39.43	353	103	-89.24	36.62	180
14	-76.49	39.39	390	44	-81.09	32.06	262	74	-84.25	38.21	257	104	-89.42	37.31	213
15	-76.49	38.98	243	45	-81.46	39.42	383	75	-84.5	39.09	311	105	-89.52	37.31	362
16	-76.58	36.73	222	46	-81.47	34.84	257	76	-84.51	38.04	259	106	-89.99	38.55	254
17	-76.6	36.07	198	47	-81.61	34.28	293	77	-84.52	39.1	352	107	-90	35.83	184
18	-76.63	39.29	327	48	-81.86	40.27	280	78	-84.56	38.21	319	108	-90.02	37.95	358
19	-77.03	38.89	322	49	-81.98	36.71	358	79	-84.87	38.2	340	109	-90.07	29.97	344
20	-77.04	38.81	259	50	-81.99	33.47	292	80	-84.88	38.21	267	110	-90.22	38.63	315
21	-77.46	38.3	271	51	-82.01	39.94	351	81	-85.15	41.05	236	111	-90.38	38.23	361
22	-77.48	37.53	321	52	-82.02	34.5	280	82	-85.73	38.31	282	112	-91.3	31.58	226
23	-77.48	37.55	321	53	-82.26	39.95	325	83	-85.74	37.57	275	113	-91.4	31.56	454
24	-78.37	38.99	376	54	-82.56	35.59	416	84	-85.75	37.57	279	114	-92.03	38.55	278
25	-78.49	42.09	255	55	-82.6	39.71	247	85	-85.78	38.25	187	115	-92.2	38.5	369
26	-78.65	35.79	270	56	-82.95	39.59	245	86	-85.96	36.26	480	116	-93.1	31.76	272
27	-79.31	33.38	214	57	-82.99	39.33	479	87	-86.66	36.88	237				
28	-79.42	43.77	267	58	-83.02	36.4	479	88	-86.78	36.17	329				
29	-79.63	43.68	191	59	-83.02	40.09	378	89	-86.87	36.52	282				
30	-79.88	40.02	396	60	-83.05	42.33	317	90	-86.89	36.85	286				

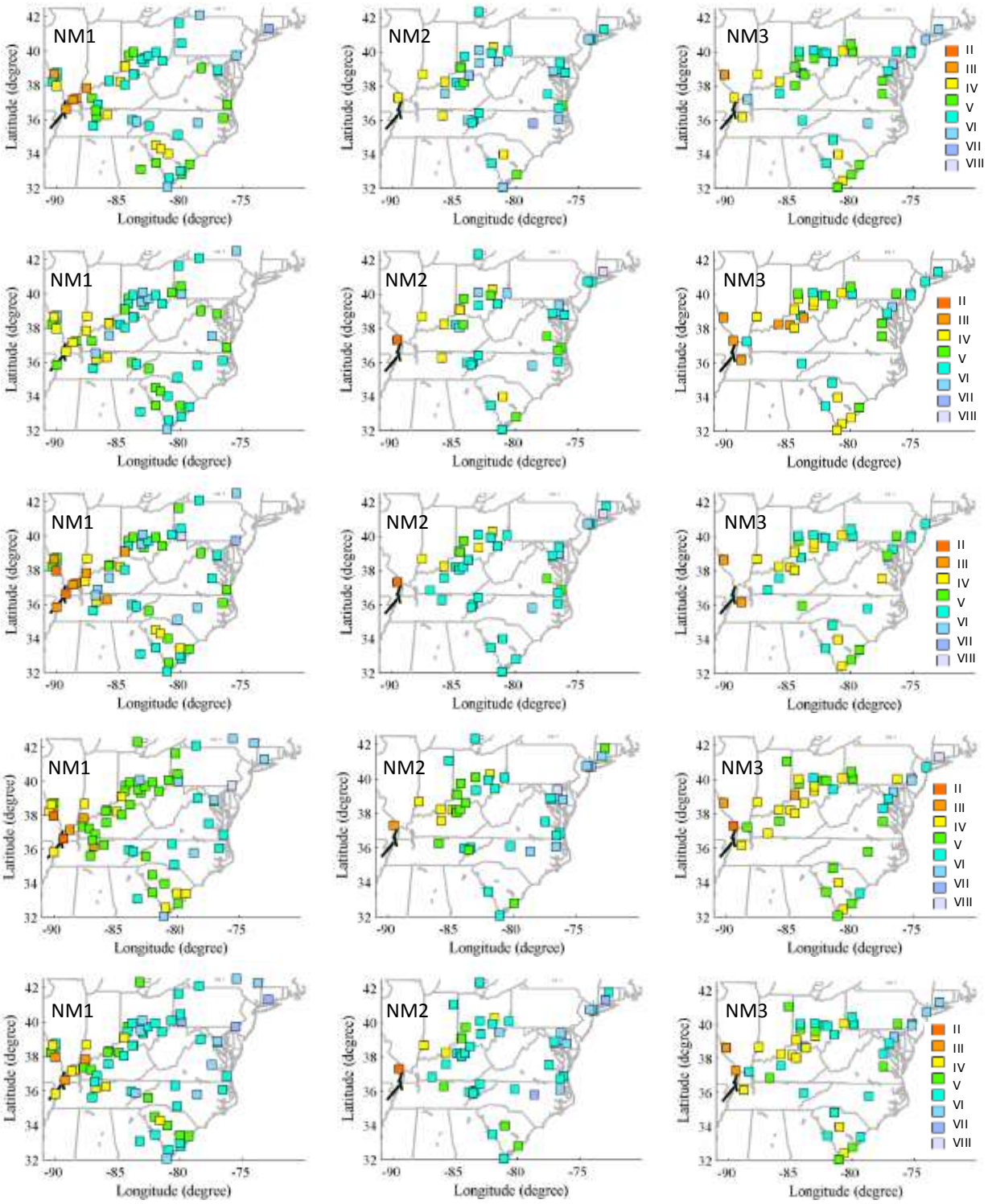

Figure 3. Observed intensities reported by Hough and Page (2011). The first, second and third columns show the data for the NM1 (December 16 1811), NM2 (January 23, 1812) and NM3 (February 7, 1812) respectively. The first four rows show the interpreted intensity from each of four experts. The bottom row shows the average intensity reported by the four experts.

3.1 Intensity Decay with Distance

We used the Bakun and Hopper (2004) model 3 (BH04) and the Atkinson and Wald (2007) (AW07) models to assess the attenuation of intensities with distance. These models describe intensity as function of distance and magnitude. Figure 4 shows the observed intensities for three events NM1 (top panel), NM2 (middle panel), and NM3 (bottom panel) plotted against the median BH04 (blue) and AW07 (red) attenuation models. Two magnitudes are considered for each attenuation model; a higher magnitude for different segments of the fault and a magnitude 7.0 scenario used by the USGS (personal communication with Robert Graves, 2015). We can see that the observed dispersion in MMI for NM3, the central thrust faulting event, is much larger in the distance range of 200 to 1200 km than it is for the two strike-slip events (NM1 and NM2). Figure 4 shows that AW07 better describes the median decay of intensity with distance for these three events. For this reason, we have selected the AW07 attenuation model (equation 1) in the following analyses using the coefficient set for Central and Eastern United States (Atkinson and Wald, 2007):

$$MMI = c_1 + c_2(M-6) + c_3(M-6)^2 + c_4 \log R + c_5 R + c_6 B + c_7 M \log R$$
$$\text{where } R = \sqrt{D^2 + h^2} \qquad (1)$$
$$B = \begin{cases} 0 & R \le R_t \\ \log R / R_t & R > R_t \end{cases}$$

3.2 Effect of site-conditions on the observed intensities

Hough and Page (2011) corrected their intensity estimates for site conditions. We checked their data for possible remaining effects of local site amplification by inspecting the variation of the observed intensities with the associated local time-averaged shear-wave velocity down to 30m (V_{S30}). For estimating V_{S30} values, we used the method developed by Wald et al. (2004) and Wald and Allen (2007) that derives seismic site conditions using topographic slope as a proxy. They correlated V_{S30} measurements against topographic slope and developed sets of coefficients for active tectonic and stable continental regions. These coefficients have been applied to the continental U.S. by Wald and Allen (2007), and in other regions around the world. The USGS website provides an online application where V_{S30} maps can be requested for an arbitrary geographical region. We used the estimated V_{S30} at the location of the intensity observations.

To study the potential impact of site-conditions, we corrected the Hough and Page (2011) intensity estimates for distance dependence using the AW07 intensity attenuation equation. Then we studied the trend of corrected intensities with V_{S30}. Residuals are defined as:

$$R = MMI - AW07 \qquad (2)$$

where MMI is the observed intensity and AW07 is the prediction of intensity using the Atkinson and Wald (2007) intensity attenuation prediction equation. A positive residual means that the observed intensity is higher than predicted and is potentially related to a lower V_{S30}.

Figure 5 shows the observed intensities (average of four experts) overlain on the contour plot of V_{S30}. Appendix A provides the same figures (A1 through A3) of observed intensities for each expert, separately overlain on V_{S30} map for historic events NM1, NM2, and NM3.

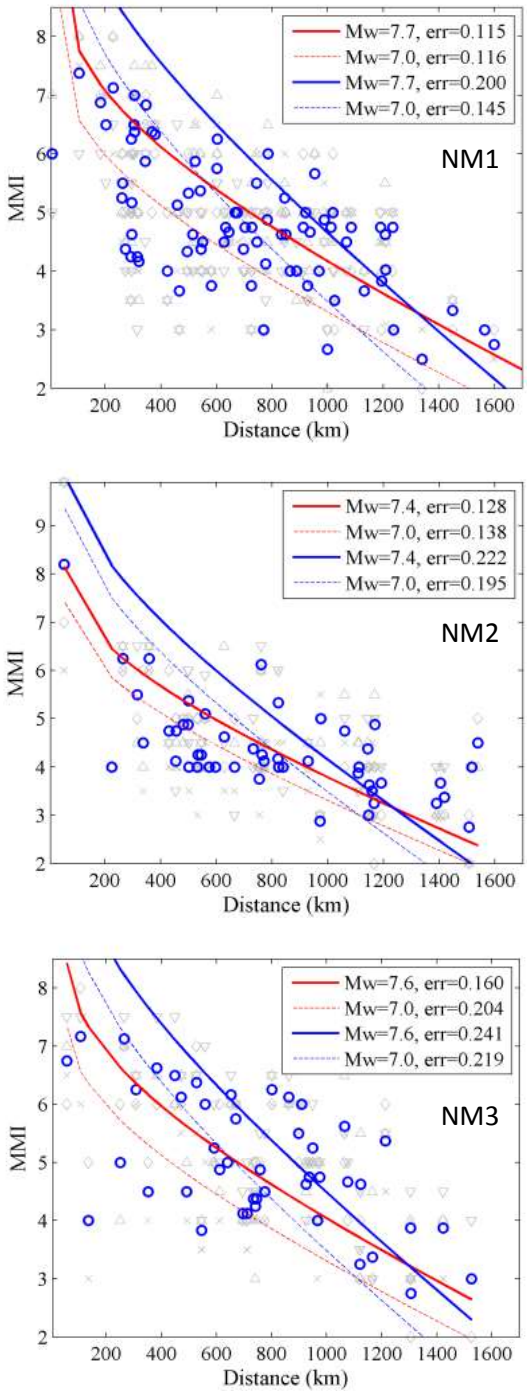

Figure 4. Observed intensities reported by Hough and Page (2011). Each panel represents the observed intensities reported by four experts (grey circles, triangles, and crosses) and the average of the four experts (blue circles) for three events; NM1 (top December 16 1811), NM2 (middle; January 23, 1812) and NM3 (bottom; February 7, 1812). Observed intensities are plotted against BH04 (blue) and AW07 (red) attenuation models. Two magnitudes are considered for each attenuation model; a larger magnitude 7.7, 7.4, and 7.6 for events NM1 through NM3 (solid) and a magnitude 7.0 (dashed).

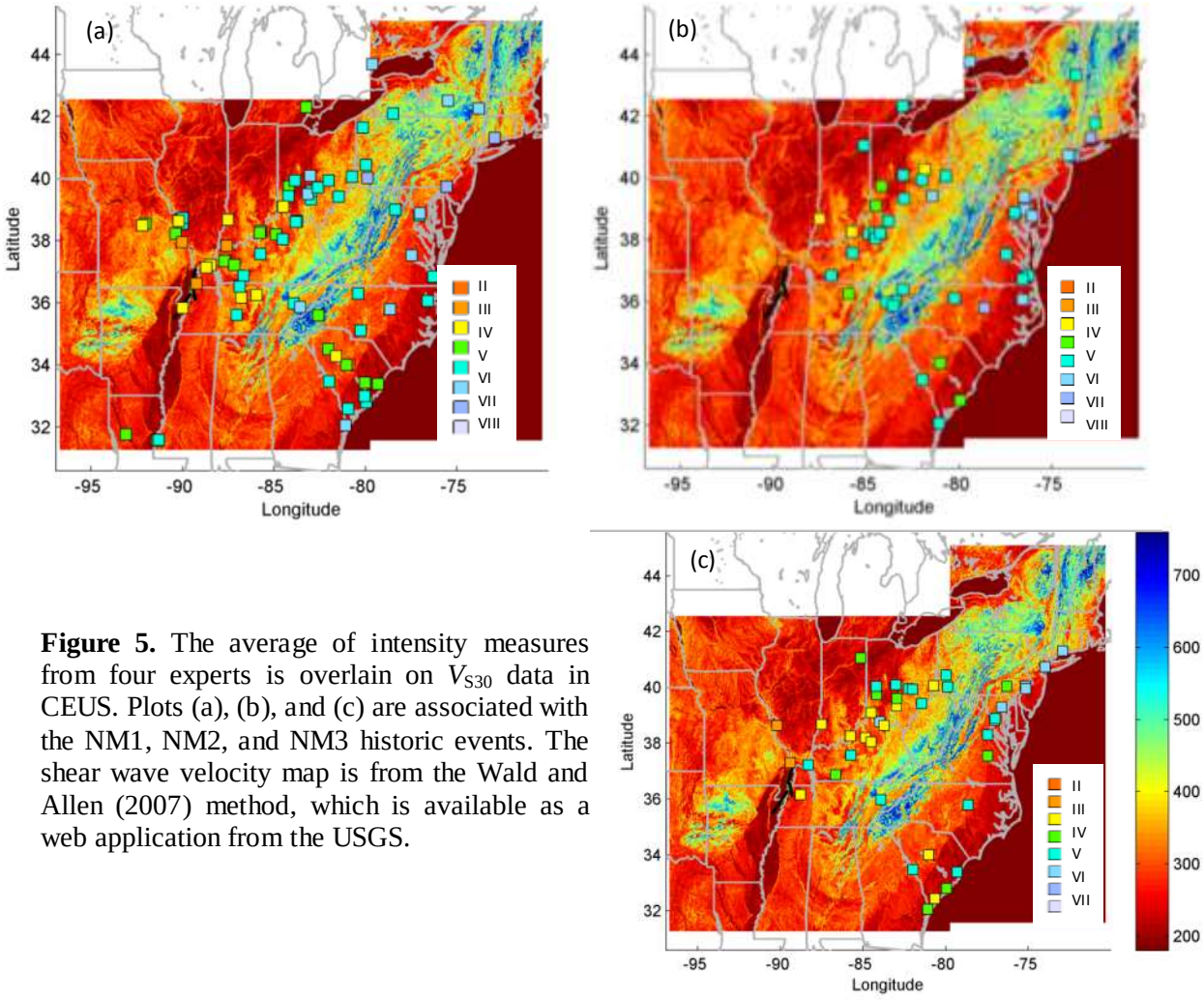

Figure 5. The average of intensity measures from four experts is overlain on V_{S30} data in CEUS. Plots (a), (b), and (c) are associated with the NM1, NM2, and NM3 historic events. The shear wave velocity map is from the Wald and Allen (2007) method, which is available as a web application from the USGS.

Figures 6 through 8 show the intensity residuals (Equation 2) plotted versus V_{S30} and also plotted on a map for the average of the four intensity estimates. V_{S30} data were independently inspected for any sign of regional correlation with distance, to assess the potential presence of a broad regional trend of site amplification, e.g. decreasing away from the New Madrid earthquakes, which all occurred within the Mississippi Embayment. We did not find any trend of decreasing residuals with increasing V_{S30} or of V_{S30} increasing with increasing distance from the NMSZ. Based on this residual analysis, we conclude that Hough and Page (2011) have effectively accounted for the effects of local soil conditions on the intensities.

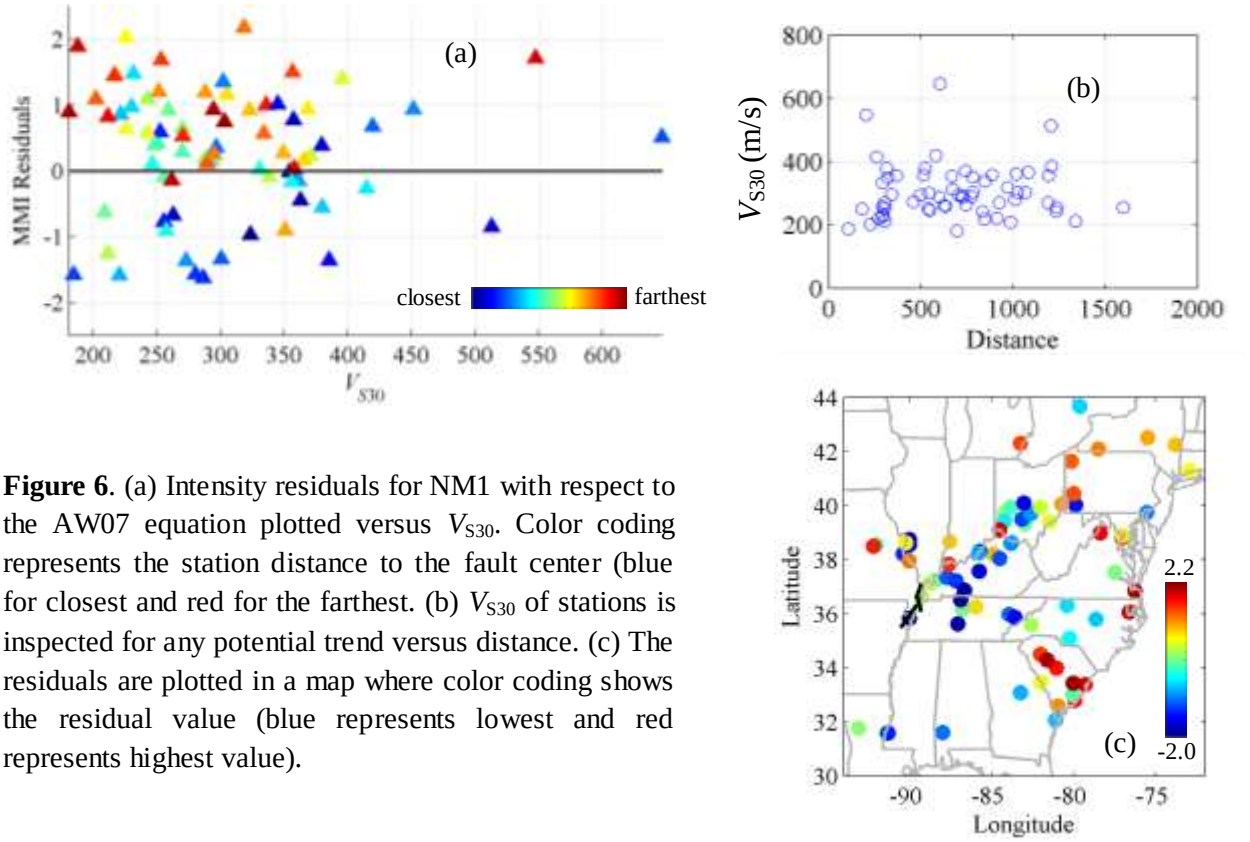

Figure 6. (a) Intensity residuals for NM1 with respect to the AW07 equation plotted versus V_{S30}. Color coding represents the station distance to the fault center (blue for closest and red for the farthest. (b) V_{S30} of stations is inspected for any potential trend versus distance. (c) The residuals are plotted in a map where color coding shows the residual value (blue represents lowest and red represents highest value).

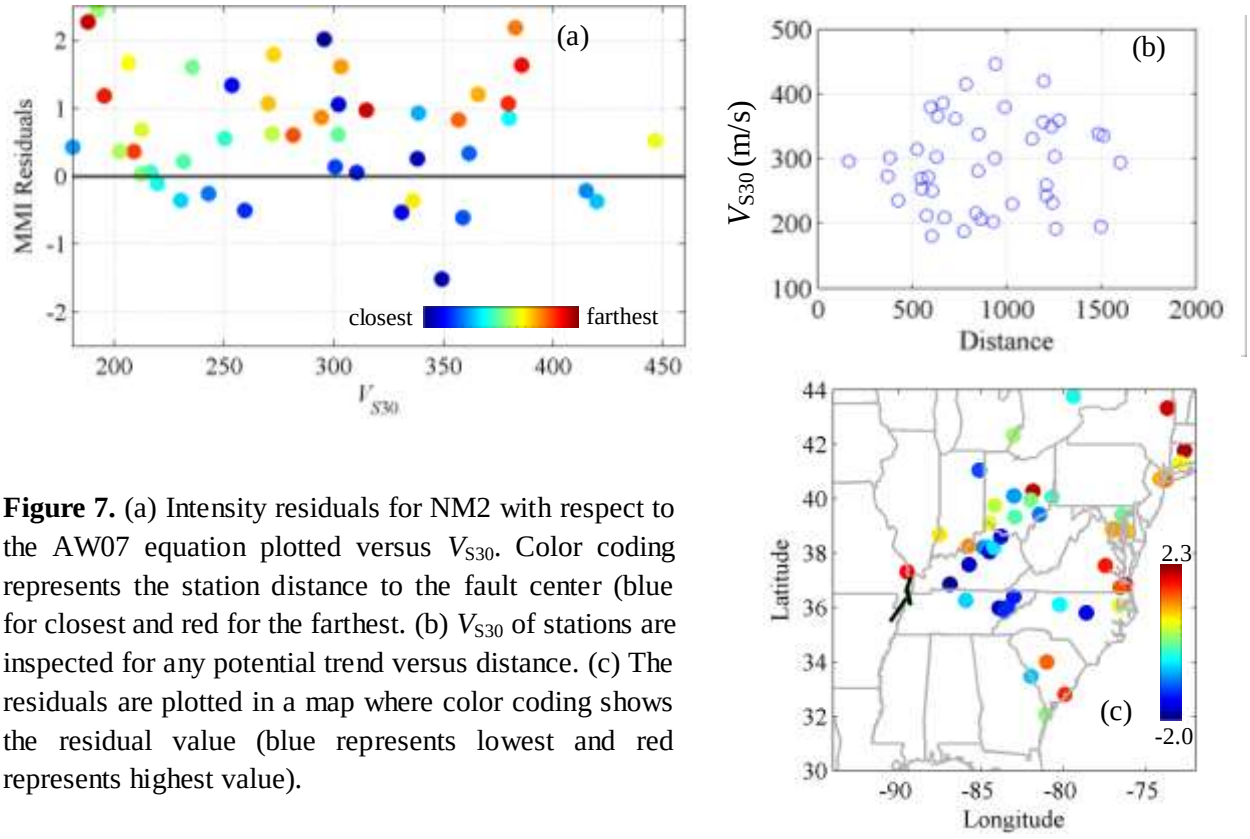

Figure 7. (a) Intensity residuals for NM2 with respect to the AW07 equation plotted versus V_{S30}. Color coding represents the station distance to the fault center (blue for closest and red for the farthest. (b) V_{S30} of stations are inspected for any potential trend versus distance. (c) The residuals are plotted in a map where color coding shows the residual value (blue represents lowest and red represents highest value).

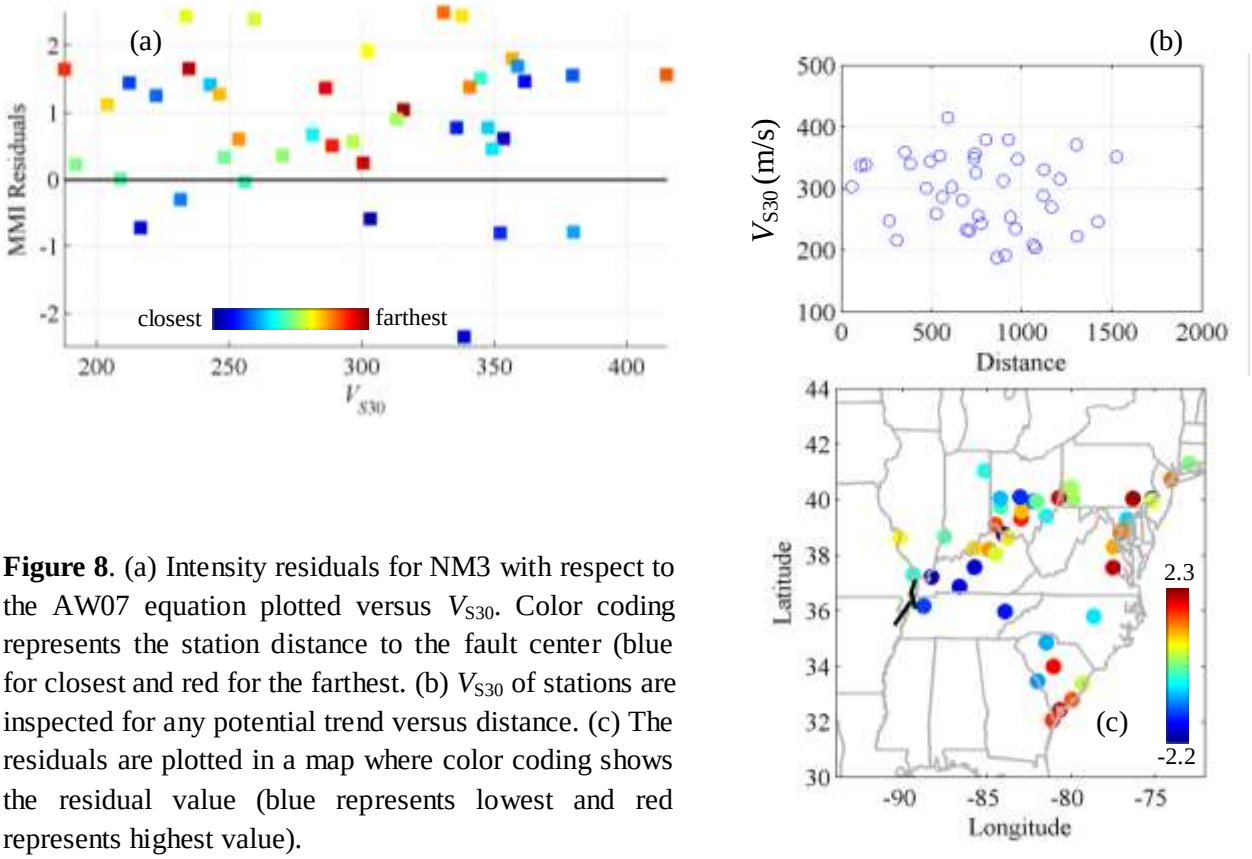

Figure 8. (a) Intensity residuals for NM3 with respect to the AW07 equation plotted versus V_{S30}. Color coding represents the station distance to the fault center (blue for closest and red for the farthest. (b) V_{S30} of stations are inspected for any potential trend versus distance. (c) The residuals are plotted in a map where color coding shows the residual value (blue represents lowest and red represents highest value).

4. Estimation of Intensities from Simulations

We used the Graves and Pitarka (2010) method, as implemented in the SCEC Broadband Simulation Platform (Maechling et al., 2015; BBP) to simulate 1D ground motions. We then converted selected ground motion intensity measures to Modified Mercalli Intensity (MMI) using appropriate conversion equations. The selected PGA, PGV, and spectral response at different periods were converted to MMI estimates using the Dangkua and Cramer (2011) and Atkinson and Kaka (2007) ground motion - intensity correlation equations (GMICEs). We refer to these two GMICEs as DC11 and AK07. The observed intensities together with the converted intensity values derived from simulations for a set of probable rupture scenarios are used to estimate the most likely earthquake magnitudes of the 1811-1812 NMSZ sequence.

To gain insight into the variability of the intensity patterns associated with different rupture scenarios for each of the three main events, we used a suite of scenarios that spans different magnitudes, hypocenters, and fault geometries. Considering the stochastic nature of the kinematic rupture model, we repeated nine simulations for a fixed magnitude, hypocenter, and fault geometry to assess the sensitivity of ground motion parameters to the stochasticity in the source model as well. We used two GMICEs, each with five different ground motion parameters to predict the intensity. The combination of different hypocenter

location, fault geometry, magnitude, and type of GMICE, provides an opportunity to study the variability of predicted intensities. The following sections provide the details used in the ground motion simulation process and intensity prediction equations.

4.1 Modeling of the New Madrid Fault Zone

Figure 9 shows the fault orientation considered for the 1811-12 earthquakes originally developed by Ramirez-Guzman et al. (2015) along with the seismicity in the New Madrid Seismic Zone. These geometries are similar to those proposed by Macpherson et al. (2010). For each fault there are two magnitudes assigned where the larger magnitude is similar to those used in the USGS National Seismic Hazard Maps, and the lower magnitude is equal to 7. Table 2 provides the fault parameters for three branches of the New Madrid fault shown in the Figure 9.

Table 2. Fault parameters for the 1811-1812 New Madrid scenarios, from Robert Graves (personal communication, 2014).

Segment	Top Center		Depth to top (km)	Length (km)	Width (km)	Strike (degree)	Dip (degree)	Average Rake (degree)	Mw
	Longitude (degree)	Latitude (degree)							
Southwest (NM1)	-90.0273	35.9036	0	140	22	229	90	180	7.7
	-89.8579	36.023	4	60	11	229	90	180	7.0
Central (NM3)	-89.383	36.3386	3	60	40	162	38.7	90	7.6
	-89.4644	36.4356	3	30	22	162	38.7	90	7.0
Northeast (NM2)	-89.4296	36.826	0	70	22	207	90	180	7.4
	-89.5069	36.7036	1	40	15	207	90	180	7.0

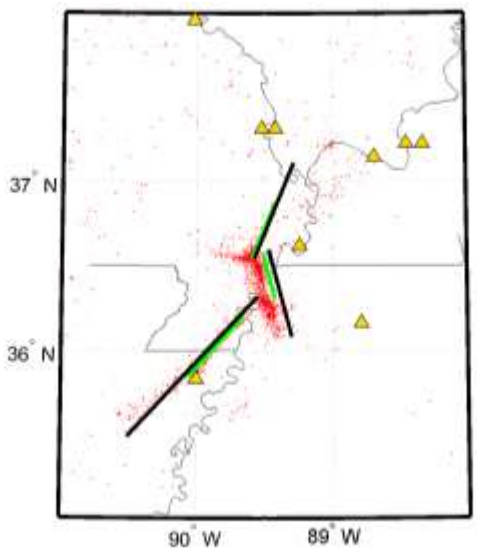

Figure 9. New Madrid region showing the surface projection of six proposed fault models for the 1811-1812 earthquakes. The black lines correspond to faults with the larger magnitude scenarios, whereas green lines to magnitude 7 scenarios. Background seismicity is shown in red.

The moment magnitude for each scenario in Table 2 is based on the Leonard (2010) magnitude-rupture area relationship developed for stable continental regions. The average rise time on the fault is calculated using the following relationship from Somerville et al. (2001) in which M_0 is the seismic moment:

$$T_r = 3.75 \times 10^{-9} M_0^{\frac{1}{3}} \quad (3)$$

4.2 Kinematic rupture models

There is little knowledge available regarding the 1811-12 New Madrid hypocenter location and distributions of slip on the fault. The near-source ground motion levels for large magnitude events are sensitive to the hypocenter location, particularly for the low frequencies (< 1Hz). The hypocenter location and selected magnitudes (as provided in Table 2) that we used to create our kinematic rupture models were recommended by Robert Graves (personal communication, 2015). Recommendations for higher magnitudes include three hypocenter locations for the Southwest segment, and two hypocenter locations for the Central and Northeast segments. For the magnitude 7, single hypocenter locations for the Southwest, Northeast, and the Central Segments are considered. This combination of hypocenters leads to ten scenarios for which we generated kinematic rupture models. The ten scenarios are listed in Table 3 and shown in Appendix B. The kinematic rupture model of a magnitude 7.6 scenario (scenario #1 in the Table 3) on the central segment (NM3) is shown as an example in Figure 10. Nine realizations were generated for each scenario except for Scenario #6 for which we generated eight realizations.

Table 3. Ten scenarios used in simulations

Scenario	Fault Segment	Magnitude M_W	Length (km)	Width (km)	Hypocenter Along Strike (km)*	Hypocenter Along Dip (km)*
1	Central	7.6	60	40	12	23
2	Central	7.6	60	40	-12	23
3	Central	7.0	30	22	0	16
4	Northern	7.4	70	22	-15	15
5	Northern	7.4	70	22	15	15
6	Northern	7.0	40	15	0	7.5
7	Southern	7.7	140	22	-55	15
8	Southern	7.7	140	22	0	15
9	Southern	7.7	140	22	55	15
10	Southern	7.0	40	15	0	8

* measured from top center of the fault segment defined in Table 3

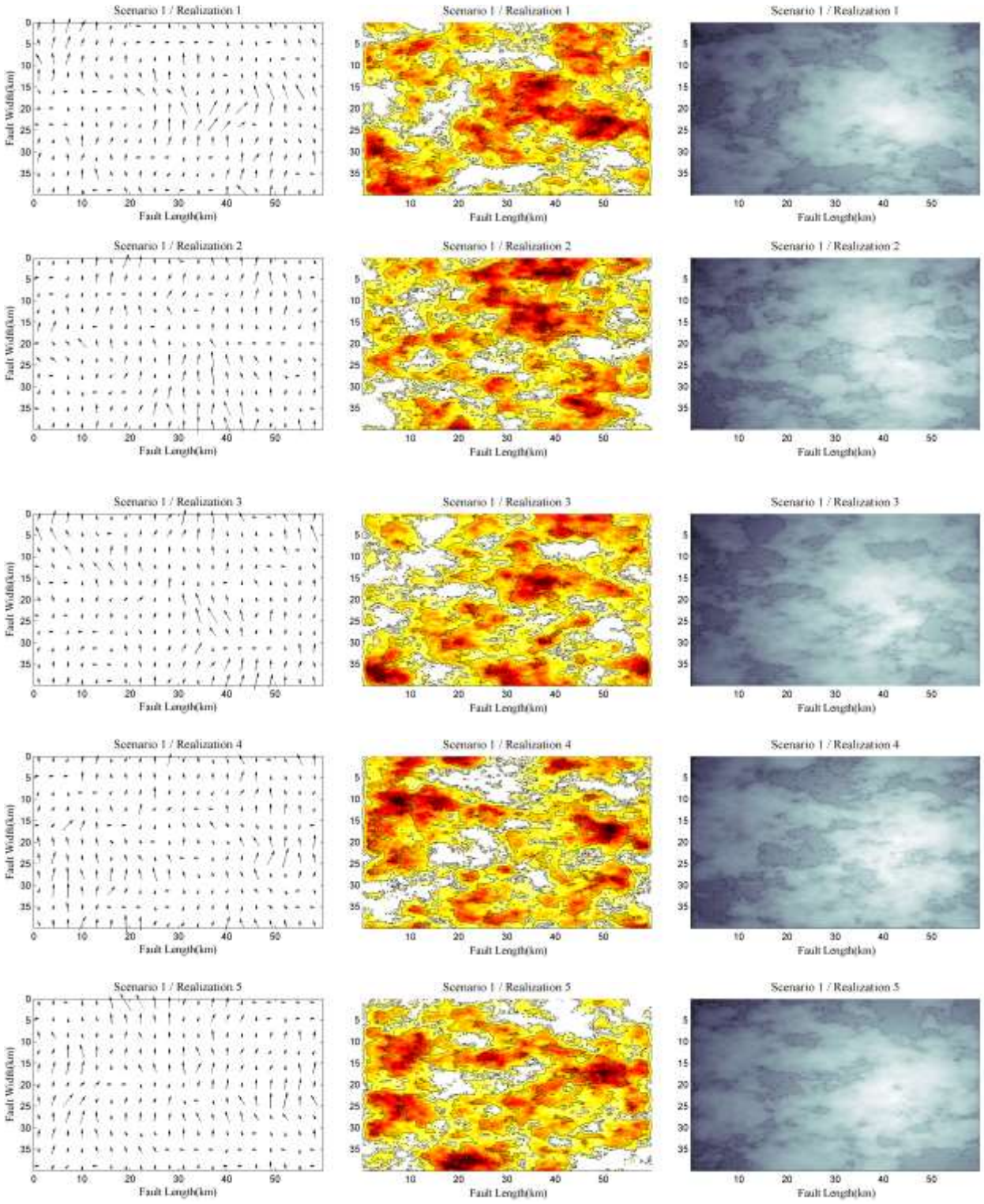

Figure 10. Kinematic rupture model developed for Central branch of New Madrid fault with **M**=7.6 (scenario 1). The left panel shows the distribution of average rake angles on each sub-fault over the fault plane. The middle panel shows the slip distribution with rupture front contours at 1 s intervals superimposed, and the right panel shows the distribution of slip rise time.

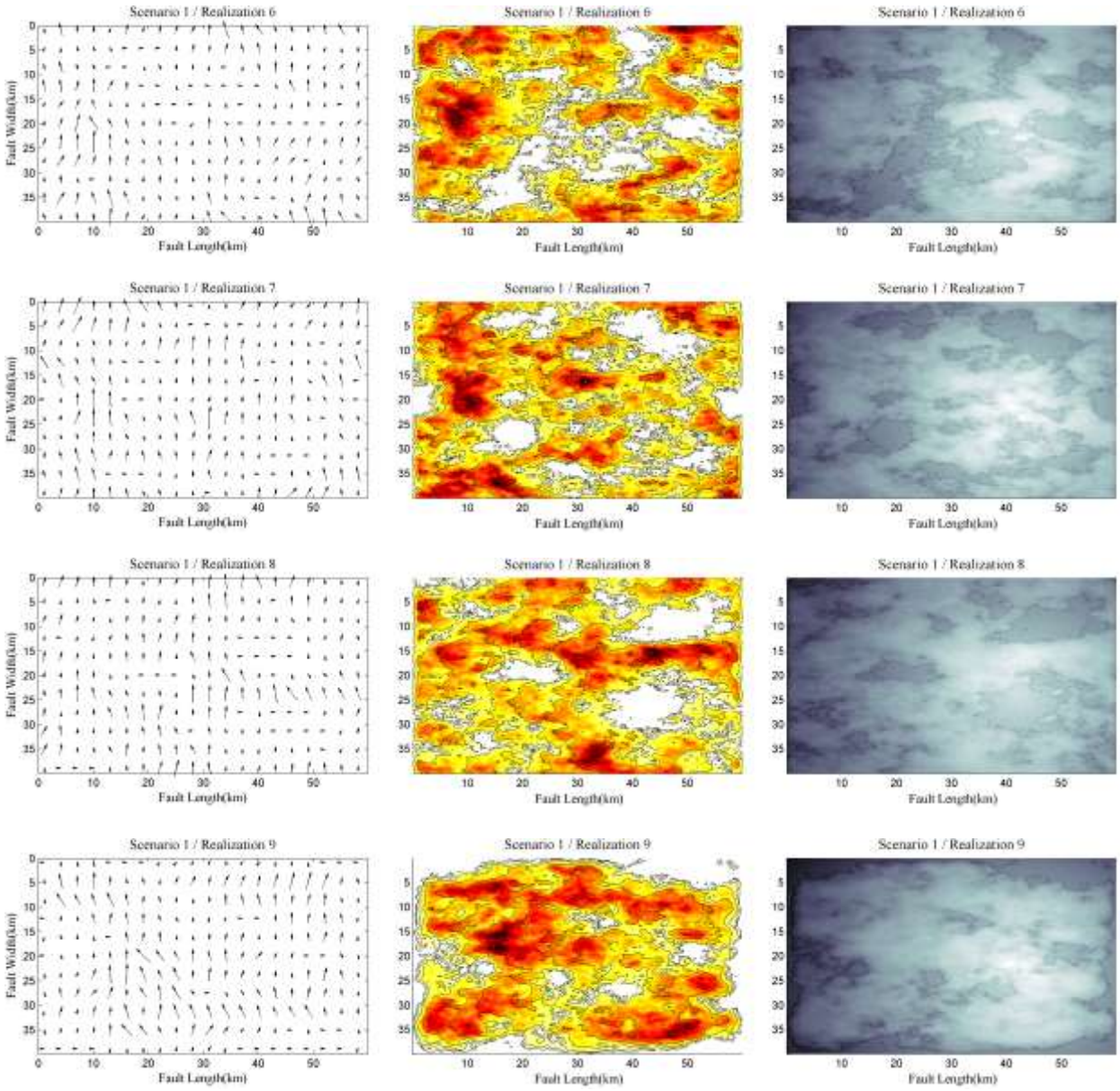

Figure 10. Continued.

4.3 Ground Motion Simulation Technique

Simulations are performed using the Graves and Pitarka (2010) method as implemented in the SCEC BBP at each location with intensity observations reported by Hough and Page (2011). The execution of the code was performed at the University of Southern California high performance computing system.

The implementation of the Graves and Pitarka (2010) method in the BBP enables the user to generate a finite-fault kinematic rupture model. The procedure then computes low frequency and high frequency synthetic time series which are combined together using a matched filter technique. Finite-fault rupture models in our study are generated for several fault models for each of the three branches of the New Madrid fault rupture, as described in Table 3. Each source model contains slip history information for each sub fault including total slip, rise time, and rake which together form the source time function of that sub fault. For the simulation of the low frequency portion of the ground motions, theoretical Green's functions (GFs) are pre-calculated for the required source-to-site distances and depths. Green's functions are generated using a representative 1D velocity model for the CEUS region, which is provided in the BBP package. The distance range for which CEUS GFs are computed in the standard release of the BBP package goes up to a distance of 1200 km. For the purpose of this study we computed additional Green's functions out to a distance of 1800 km in order to encompass all of the MMI intensity observations, while recognizing the large uncertainty involved in simulating ground motions out to this distance with a simple 1D seismic velocity model. A total of eight GFs corresponding to three different focal mechanisms (Wang and Herrmann, 1980) were generated for the distance range 1000 to 1800 km, every 10 km, and added to the BBP package. The additional GFs were generated with the wavenumber integration technique using Computer Programs in Seismology, a software package developed by Robert Herrmann at St. Louis University. These Greens functions are valid up to the Nyquist frequency of the simulations. They include all direct and scattered body waves and surface waves for a horizontally layered Earth model. The simulated wave-fields include both near and far field components. The velocity model used for computing the additional GFs is provided in Table 4. Figure 11 shows eight Green's functions generated at 1200 and 1500 km. The GFs naming convention used in Figure 11 is described in Wang and Herrmann (1980).

Table 4. Velocity model for Central Eastern United States used in BBP (version 15.3.0) for simulation using the Graves and Pitarka method.

#	Thickness (km)	V_P (km/s)	V_S (km/s)	Density (g/cc)	Q_P	Q_S
1	0.0307	1.73	1	2.0306	10	10
2	0.014	2.6832	1.551	2.1408	35.51	35.51
3	0.0553	3.1192	1.803	2.2766	38.03	38.03
4	1.833	5.19	3	2.6111	500	500
5	0.895	5.577	3.224	2.665	500	500
6	2.172	5.828	3.369	2.7	1500	1500
7	2.15	6.176	3.57	2.7568	2900	2900
8	7.5	6.18	3.57	2.7248	2900	2900
9	11	6.36	3.68	2.7811	2900	2900
10	8	7.12	4.12	3.066	2900	2900
11	1	7.15	4.13	3.052	2900	2900
12	1.2	7.26	4.2	3.0943	2900	2900
13	0.85	7.64	4.42	3.2331	2900	2900
14	0.2	7.97	4.61	3.3533	2900	2900
15	10	8.12	4.69	3.4059	2900	2900
16	10	8.35	4.7	3.4489	2900	2900
17	10	8.4	4.76	3.4775	2900	2900
18	10	8.41	4.78	3.4859	2900	2900
19	10	8.42	4.79	3.4909	2900	2900
20	10	8.42	4.81	3.4976	2900	2900
21	10	8.42	4.83	3.5043	2900	2900
22	10	8.42	4.85	3.5109	2900	2900
23	Half-space	8.43	4.87	3.5193	2900	2900

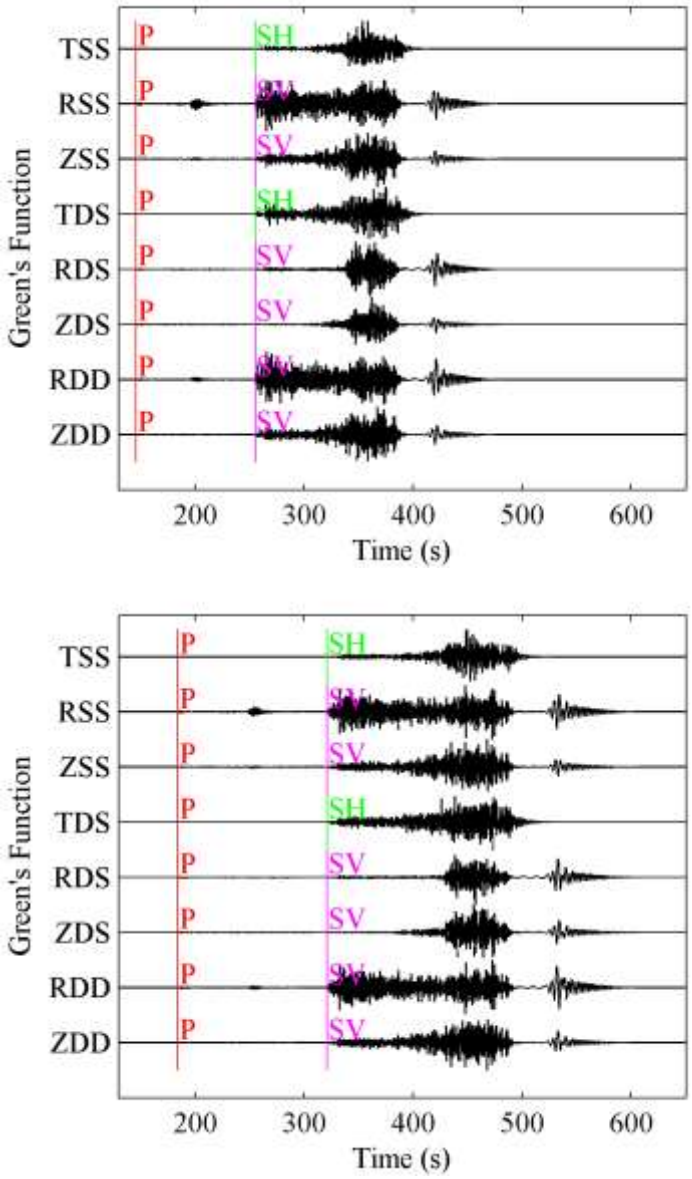

Figure 11. Green's functions at 1200 km (top) and 1500 km (bottom).

The high frequency simulation approach is based on a method formalized by Boore (1983). Its application to finite-fault simulations is described by many authors such as Frankel (1995), Beresnev and Atkinson (1997), and Hartzell et al. (1999). Details of the method that we used are described in Graves and Pitarka (2010). All methods for combining low and high frequency simulations into a broadband time series use some type of filtering and summation. The BBP package uses a set of "matched" 4^{th} order zero-phase Butterworth filters are used each with a corner frequency equal to 1Hz to combine the low and high frequencies.

We calibrated the parameters for CEUS simulations with results produced by Robert Graves for the same region (personal communication, 2016), and the work of Pezeshk et al. (2011) and Atkinson and Boore (2006). The BBP requires input parameters for both the low frequency and high frequency components of

the simulations. We selected appropriate values for these parameters based on the region, and our past experience with simulations in the CEUS. The default parameters in the BBP software package were modified according to Table 5.

As a code validation exercise, we repeated simulations for a CEUS scenario previously studied by Robert Graves (personal communication, 2015). Figures 12 and 13 show a comparison of the Fourier amplitude spectra between our simulations and those from Robert Graves at multiple stations (personal communication, 2015). In the simulations shown in Figure 12, the source rupture model from scenario 1, realization 9 (bottom row of plots at Figure 10) is used. Our simulation results are in fair agreement with those of Robert Graves as shown in Figure 14.

Figure 15 shows the simulated PGA versus distance for both horizontal components (shown with circle and cross), compared with median values from the PZT11 and AB06 GMPEs. It includes the ten scenarios shown in Figure 10, and Appendix B1 through B9. Figures 16, 17, and 18 show the simulated and empirical 5% damped response spectral accelerations at 0.3, 1, and 2 s. In Figures 15 through 18, PZT11 is based on National Earthquake Hazards Reduction Program site class A, $V_{S30} \geq 2000$ m/s and AB06 is calculated for rock site-conditions.

The simulated PGAs generally fall below the median GMPE predictions, especially at distances beyond 200km. There is closer agreement to the median GMPE values for longer response spectral amplitudes. This suggests that the low frequency component of the simulation better represents the expected ground motion in the CEUS, while the high frequency component might need additional calibration. In particular, the high frequency component does not appear to adequately replicate the flattening in the rate of attenuation between about 70 and 200 km in the GMPEs that is caused by critical reflections in the lower crust. Additional adjustments using different regional quality factors and different local kappa values based on geology may be required. Techniques for estimating kappa and quality factor are available (Hosseini et al. 2015) and could be applied in different regions in the CEUS.

Table 5. Graves and Pitarka simulation method parameter values used in the simulations.

Parameter Name	Value	Parameter Name	Value
Kappa	0.03	RISETIME_FAC	1
QFEXP	0.45	DEEP_RISETIME_FAC	1
C0	164	RVFRAC	0.8
C1	34	SHAL_RVFAC	1
SDROP	143	DEEP_RVFAC	1
DEFAULT_FCFAC	-0.4625	PATH_DUR_MODEL	2
RAYSET	[2,1,2]	RVSIG	0
RISETIME_COEF	3.75	VSMOHO	4.69
SHAL_VRUP	0.7		

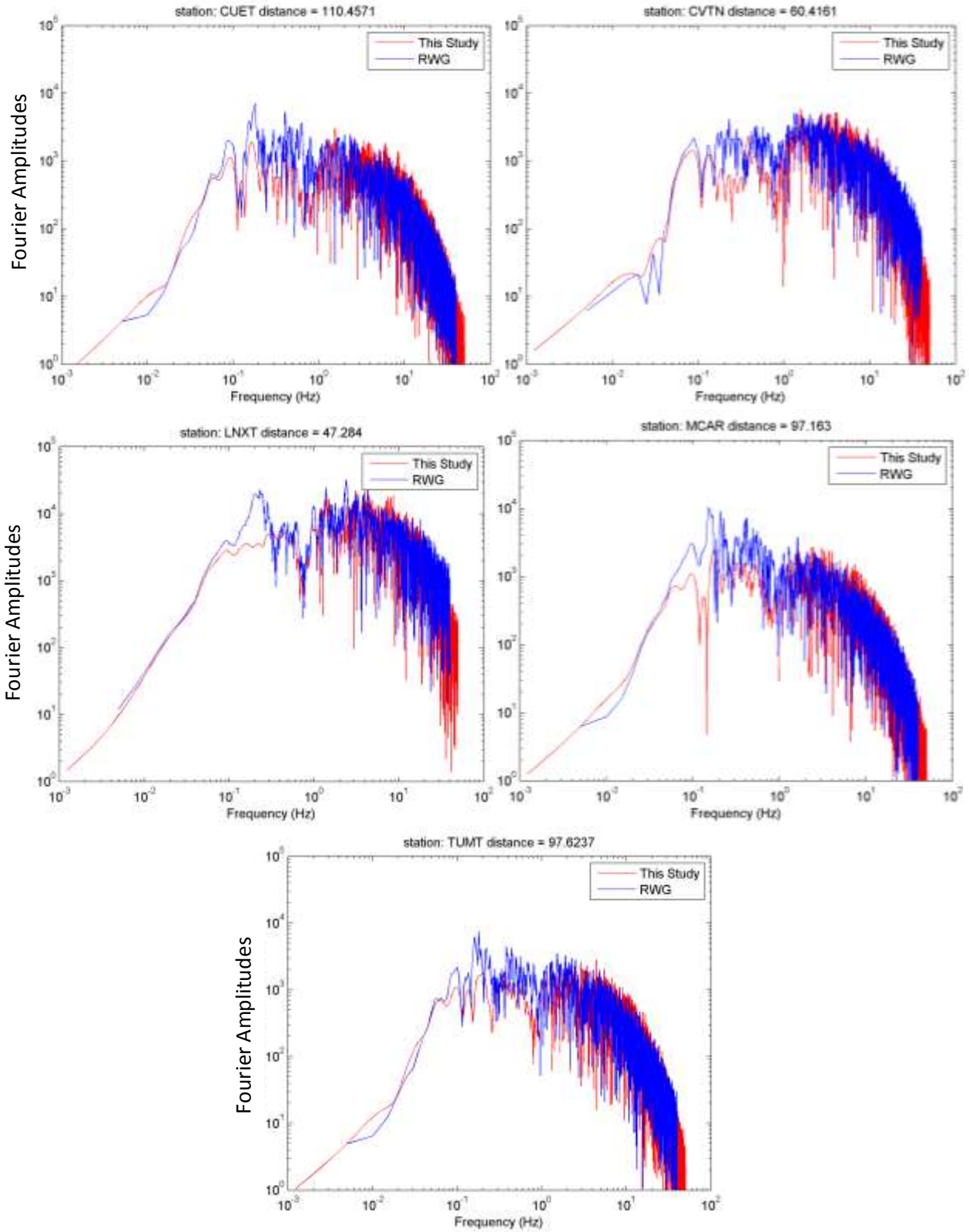

Figure 12. Calibration of our simulations with those from Robert Graves (RWG): five CERI stations.

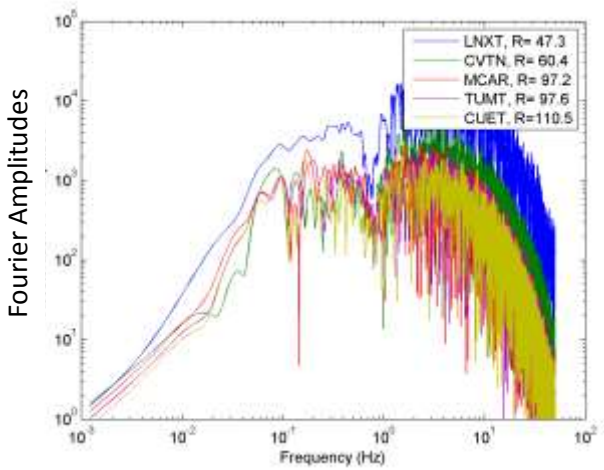

Figure 13. Simulation at the location of CERI stations showing the Fourier amplitude decay with distance.

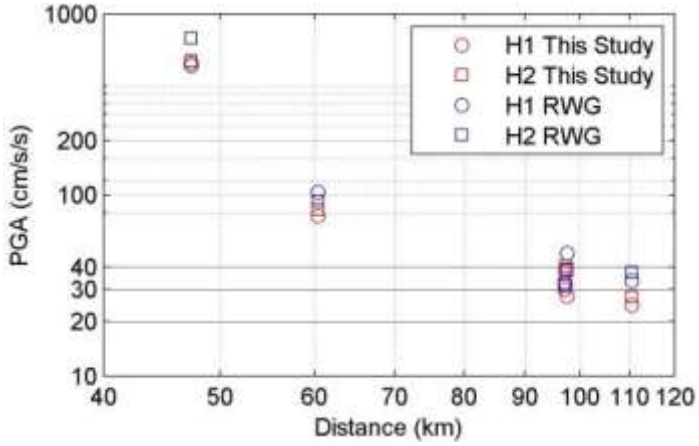

Figure 14. Calibration of our simulations with those from Robert Graves (RWG): PGA attenuation with distance.

Although limited to distances up to 180 km, the same trends are seen in the results obtained by Ramirez et al. (2015), as shown in Figure 19, even though Ramirez et al. (2015) used 3D simulations and ours are 1D. The flattening in attenuation is not evident in the PGA simulations, but it is evident in the simulations for response spectral acceleration at 2 seconds period, consistent with our results.

In view of the lack of a 3D seismic velocity of the entire region for which there are observed MMI intensities of the New Madrid earthquakes, and the large distance this region spans, it was impractical for us to use a 3D velocity model in our simulations, so we had to use 1D simulations. On the other hand, a 3D simulation of ground motion considers the effects of basins realistically and can better simulate the near fault effects. The near fault effects are strongly dependent on the slip and finite fault characteristics and they are not so important in the far field, so a 3D simulation can give a better outcome for the near fault stations which might improve the results. We are interested to use 3D ground motion simulation

technique in the future, when the USGS 3D velocity model covers a larger area in CEUS and source characteristics are better constrained.

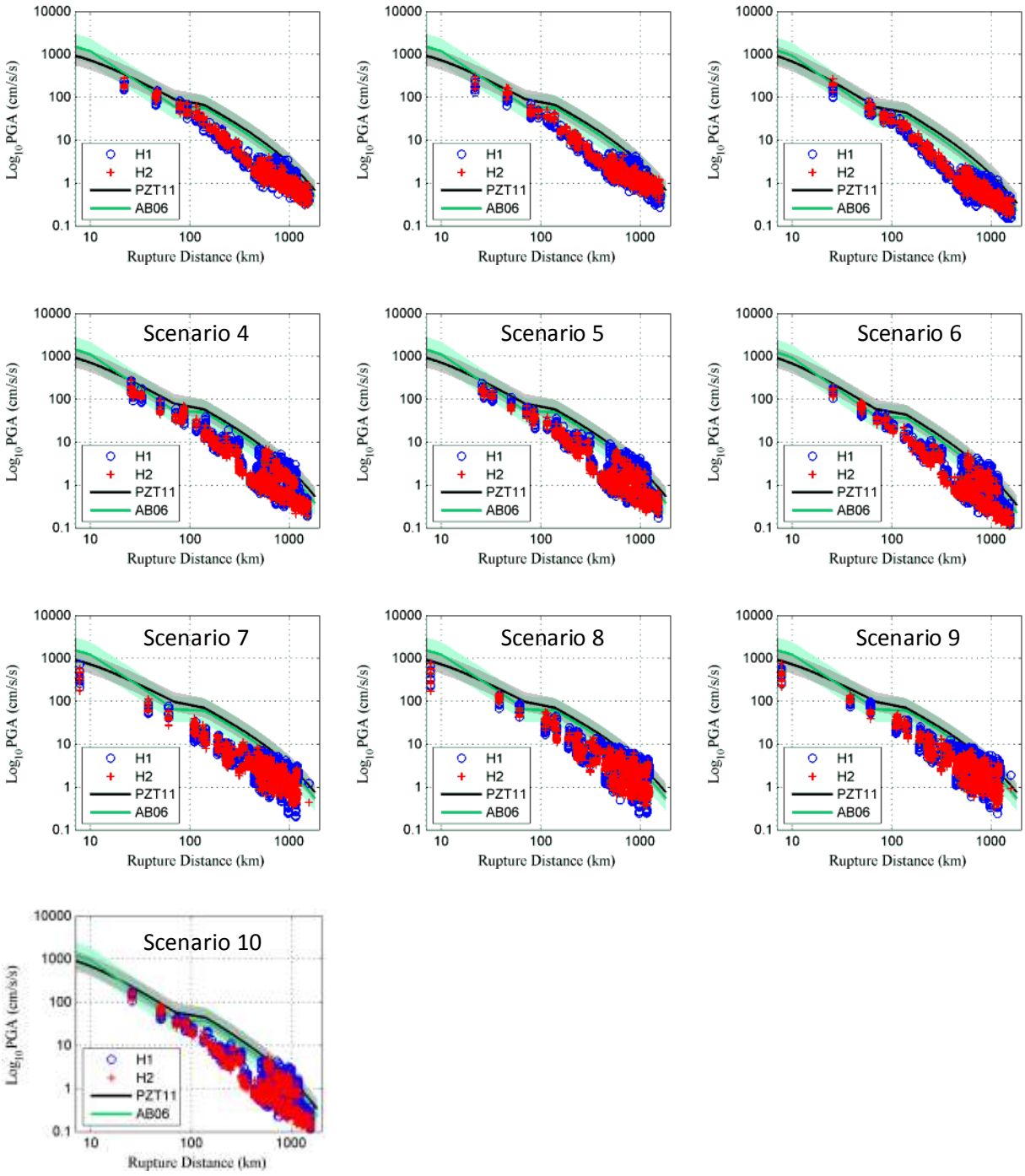

Figure 15. Simulated PGA values for two horizontal components (H1, H2) compared with Pezeshk et al. (2011) and Atkinson and Boore (2006) GMPE median predictions (black and green lines, respectively.) The shaded areas represent the aleatory variability of the GMPEs. The range shown is the median plus and minus one standard deviation.

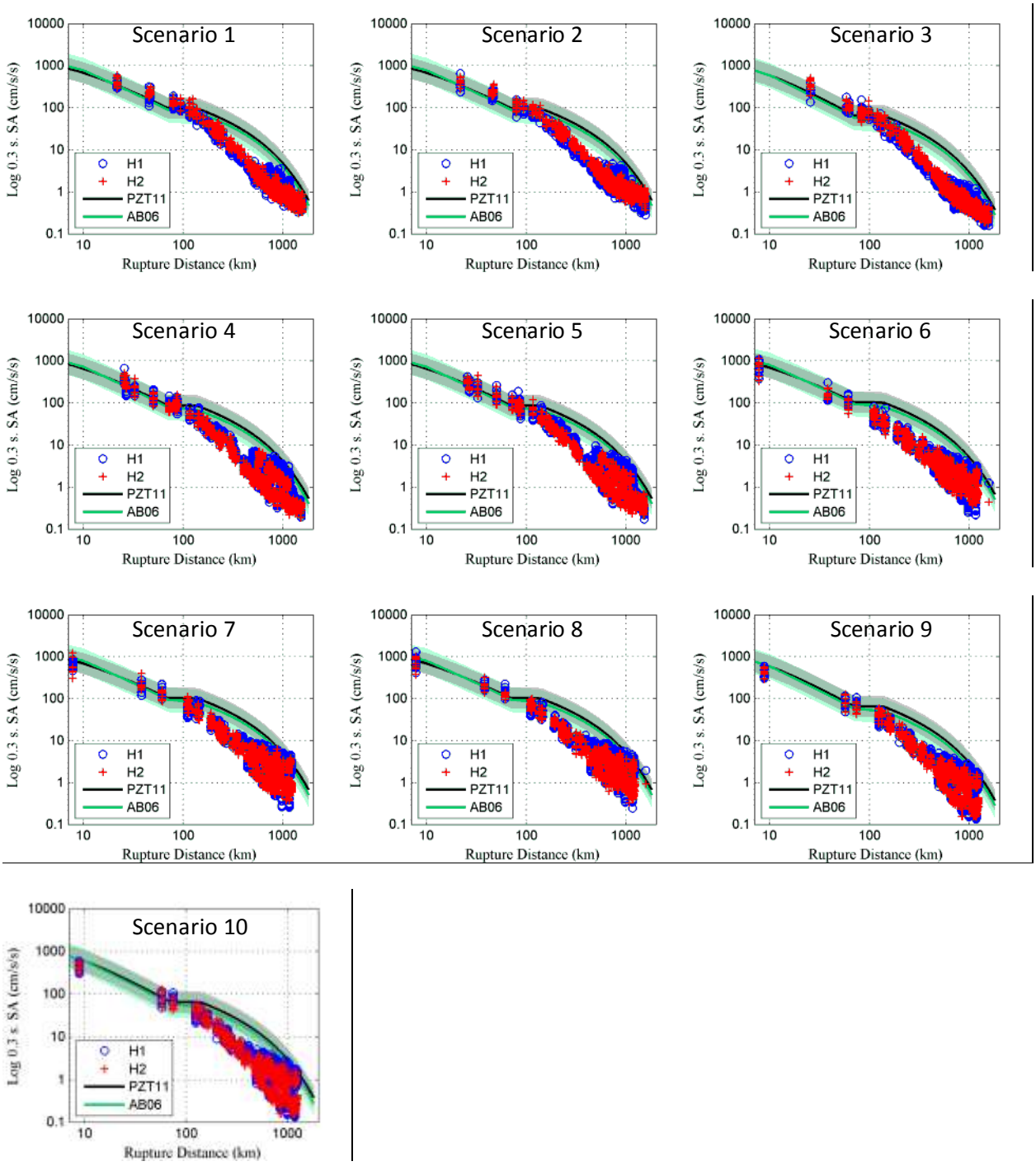

Figure 16. T = 0.3 s response spectral acceleration of the simulations for two horizontal components compared with Pezeshk et al. (2011) and Atkinson and Boore (2006) GMPE median predictions (black and green lines, respectively.) The shaded areas represent the aleatory variability of the GMPEs. The range shown is the median plus and minus one standard deviation.

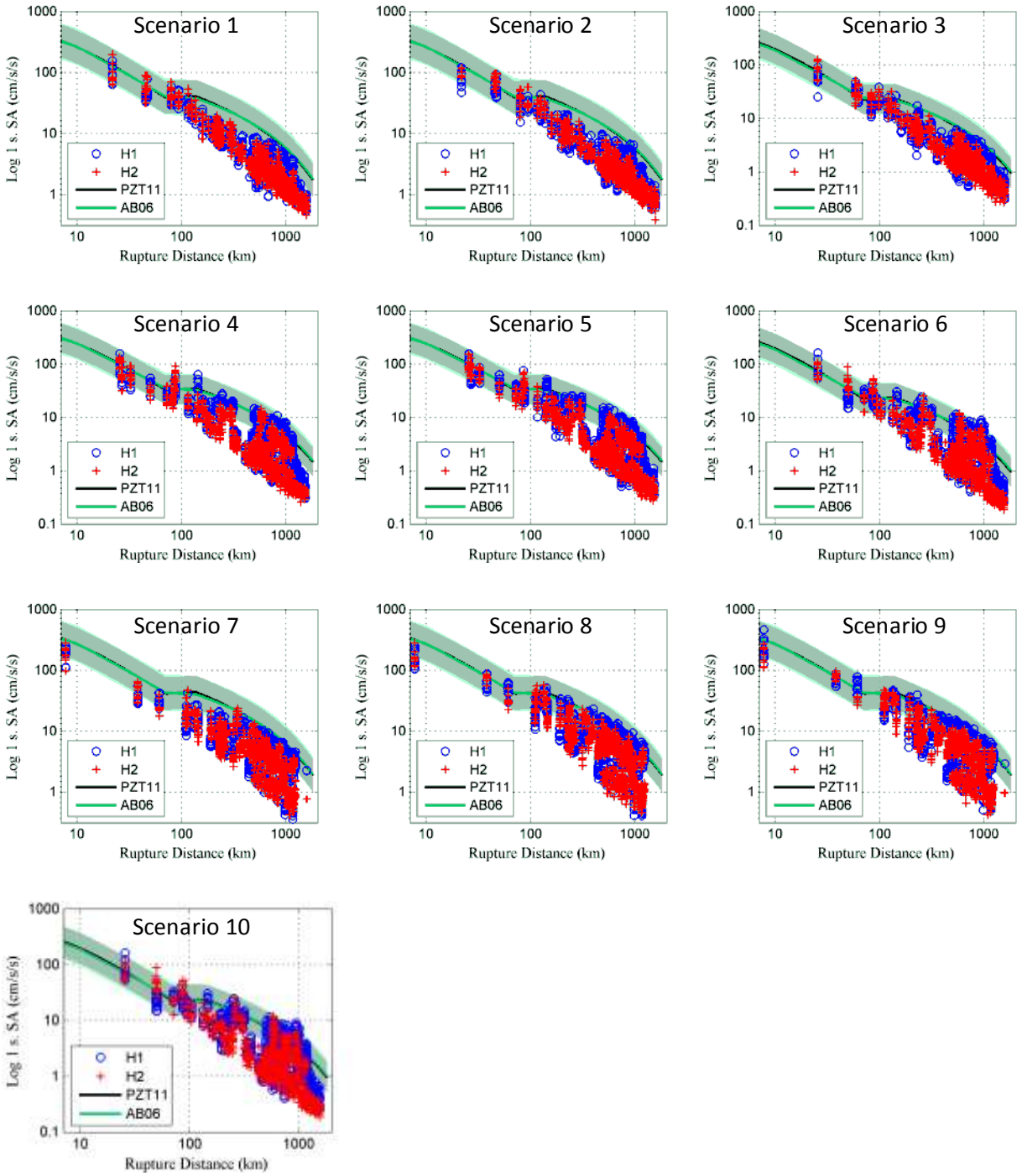

Figure 17. T = 1.0 s response spectral acceleration of the simulations for two horizontal components compared with Pezeshk et al. (2011) and Atkinson and Boore (2006) GMPE median predictions (black and green lines, respectively.) The shaded areas represent the aleatory variability of the GMPEs. The range shown is the median plus and minus one standard deviation.

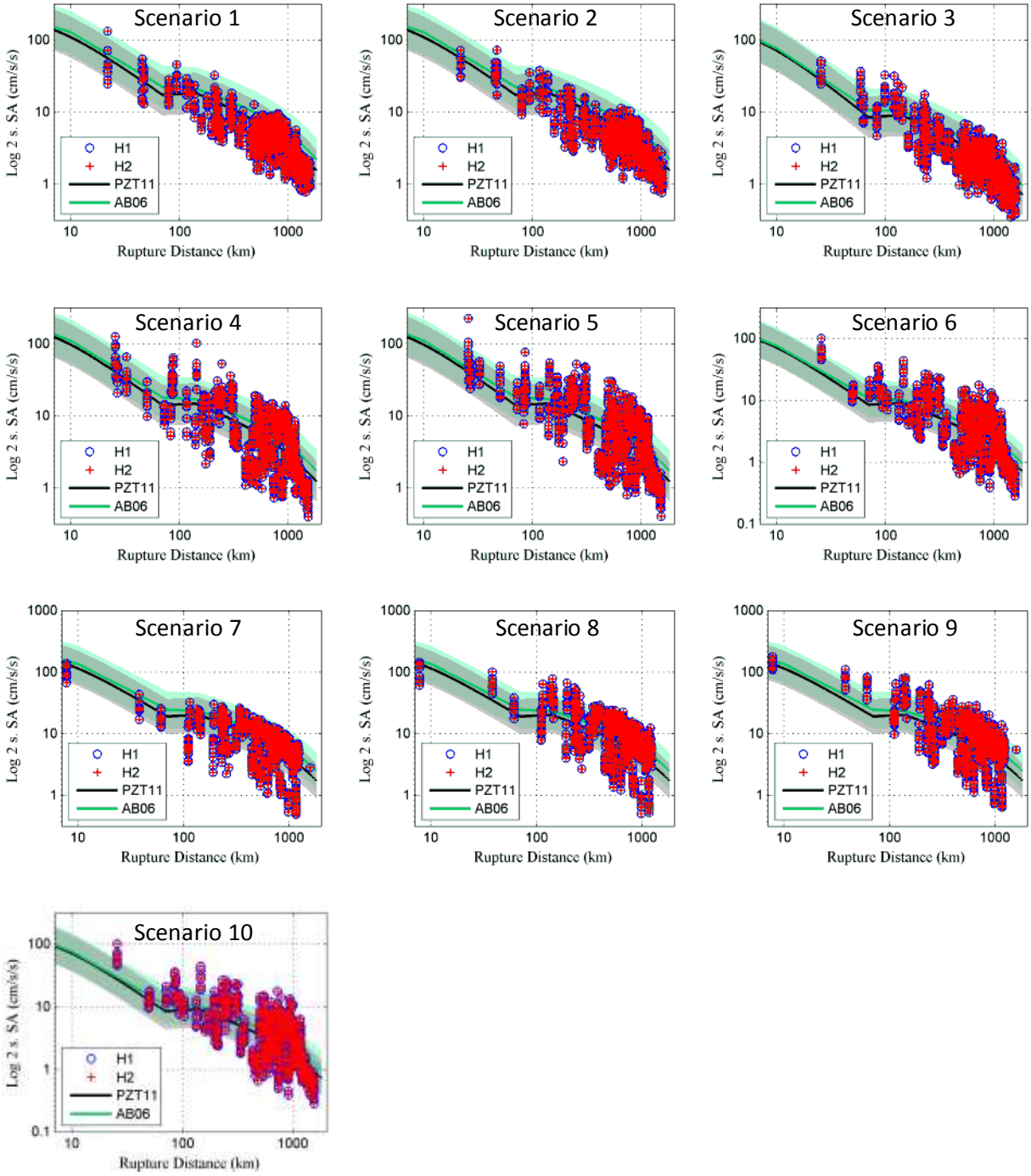

Figure 18. T = 2.0 s response spectral acceleration of the simulations for two horizontal components compared with Pezeshk et al. (2011) and Atkinson and Boore (2006) GMPE median predictions (black and green lines, respectively.) The shaded areas represent the aleatory variability of the GMPEs. The range shown is the median plus and minus one standard deviation.

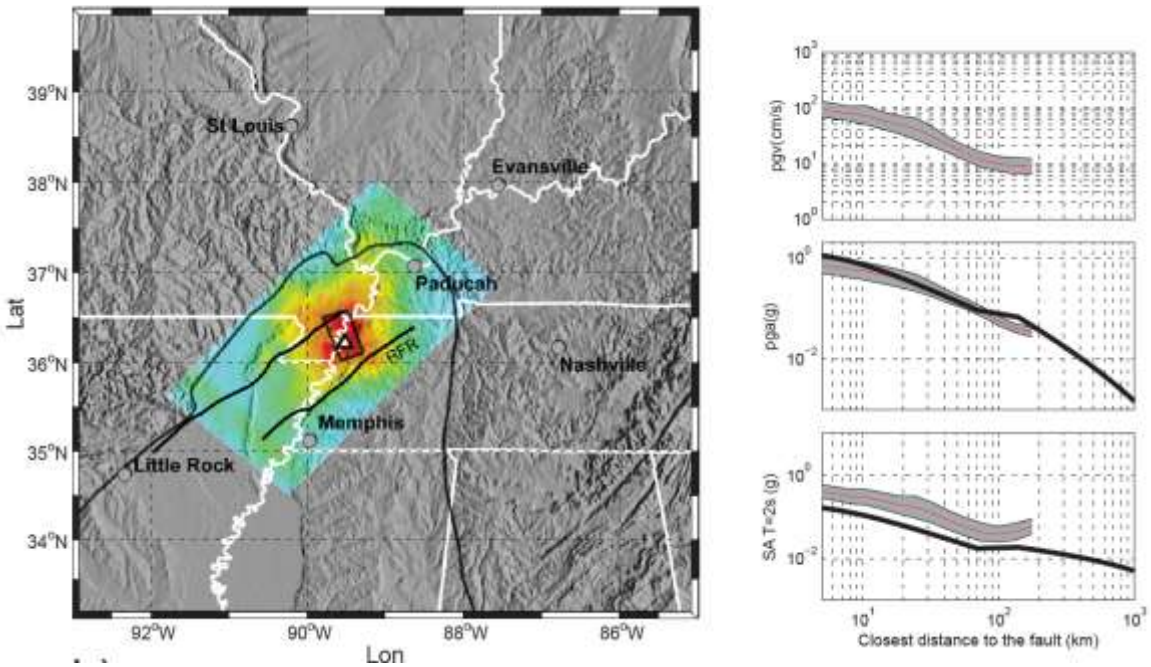

Figure 19. Left: Simulated PGV for an Mw 7.6 NM3 event. Right: Comparison of simulated PGV, PGA and 2 second spectral acceleration using the Graves and Pitarka method with the Pezeshk et al. (2011) GMPE. The flattening in attenuation is not evident in the PGA simulations, but it is evident in the simulations for response spectral acceleration at 2 seconds period. (Source: Ramirez-Guzman et al., 2015).

4.4 Estimation of Intensities from Ground Motion Simulations

MMIs can be estimated from several ground motion parameters such as peak ground acceleration (PGA), peak ground velocity (PGV), and spectral acceleration (SA) at various periods. PGV is ideal because it is the most readily available parameter from some seismographic networks and is most directly related to kinetic energy (Kaka and Atkinson, 2004). Only the horizontal components of the synthetics were converted to MMI. Considering the special attributes of ground motion propagation in the CUS and ENA we used the Atkinson and Kaka (2007) and Dangkua and Cramer (2011) empirical relations to convert the selected intensity measures to MMI. We refer to these GMICEs as AK07 and DC11 throughout this report. The geometric mean of the two horizontal components was used as input into these GMICEs. AK07 can be used to estimate the intensities using the ground motion intensity measure alone, or along with magnitude and distance. DC11 estimates the intensity based on the ground motion intensity measure, the earthquake magnitude and station distance. We did not use magnitude as an input parameter in the AK07 GMICE because magnitude is an unknown parameter that we are seeking to estimate; instead we used the magnitude-independent version of that GMICE.

4.5 Comparison of Simulation-Based and Observed Intensities

Examples of the results showing the comparison between observed and simulated intensities, and their residual distribution against distance, are given for four different spectral periods in Figures 20 through 27. These figures, which display DC11 for PGA, AK07 for PGV, and DC11 for T=1.0 sec and AK07 for T = 2.0 sec Sa, exhibit the best fit between the simulations and the observations. The complete set of results, showing simulated intensities calculated using the two GMICEs for each of several ground motion intensity measures, is provided in Appendix C.

To quantify the misfit between our simulated intensities, and those from observations and GMPEs, we calculated the root mean square (RMS) error for each intensity measure used as input to GMICE (PGA, PGV, SA at 0.3 s, SA at 1.0 s, SA at 2.0 s), and GMICE model (AK07 and DC11). The RMS errors are calculated from the residuals between observed and simulated intensities (type 1 RMS error, E_1, in odd numbered Figures 21 through 27 and even numbered Figures C2 through C12) and from the residuals between observed intensities and those predictions from the AW07 attenuation equation (type 2 RMS error, E_2) RMS error values are normalized by the number of observations to be appropriate for a direct comparison. The results are shown in Table 6 for the AK07 GMICE and in Table 7 for the DC11 GMICE.

The results for the five parameters through which MMI is calculated shown in Figures 20 through 27 are highlighted in Tables 6 and 7, with the best fitting scenarios shown in green. Best fitting scenarios are selected using the minimum average error of GMICE input parameters for each historic event. Average error is calculated for each scenario over five E_1 errors from different GMICE input parameters. For the average of all simulated intensity measures, the best fitting scenario earthquakes are 2 (Mw 7.6 for NM3), 4 or 5 (Mw 7.4 for NM2), and 7 or 9 (Mw 7.7 for NM1). The aggregate of the error analysis leads to Mw 7.7 for NM1, Mw 7.4 for NM2, and Mw 7.6 for NM3. Although there is a large degree of discrepancy between the observed and simulated intensities, there is a slight preference for the larger magnitudes, which are systematically higher than those described by Hough and Page (2011) and comparable to those estimated by Cramer and Boyd (2014). The RMS errors for NM3 are significantly larger than those of NM1 and NM2, reflecting the larger dispersion in the observed MMI intensities of NM3 as already noted.

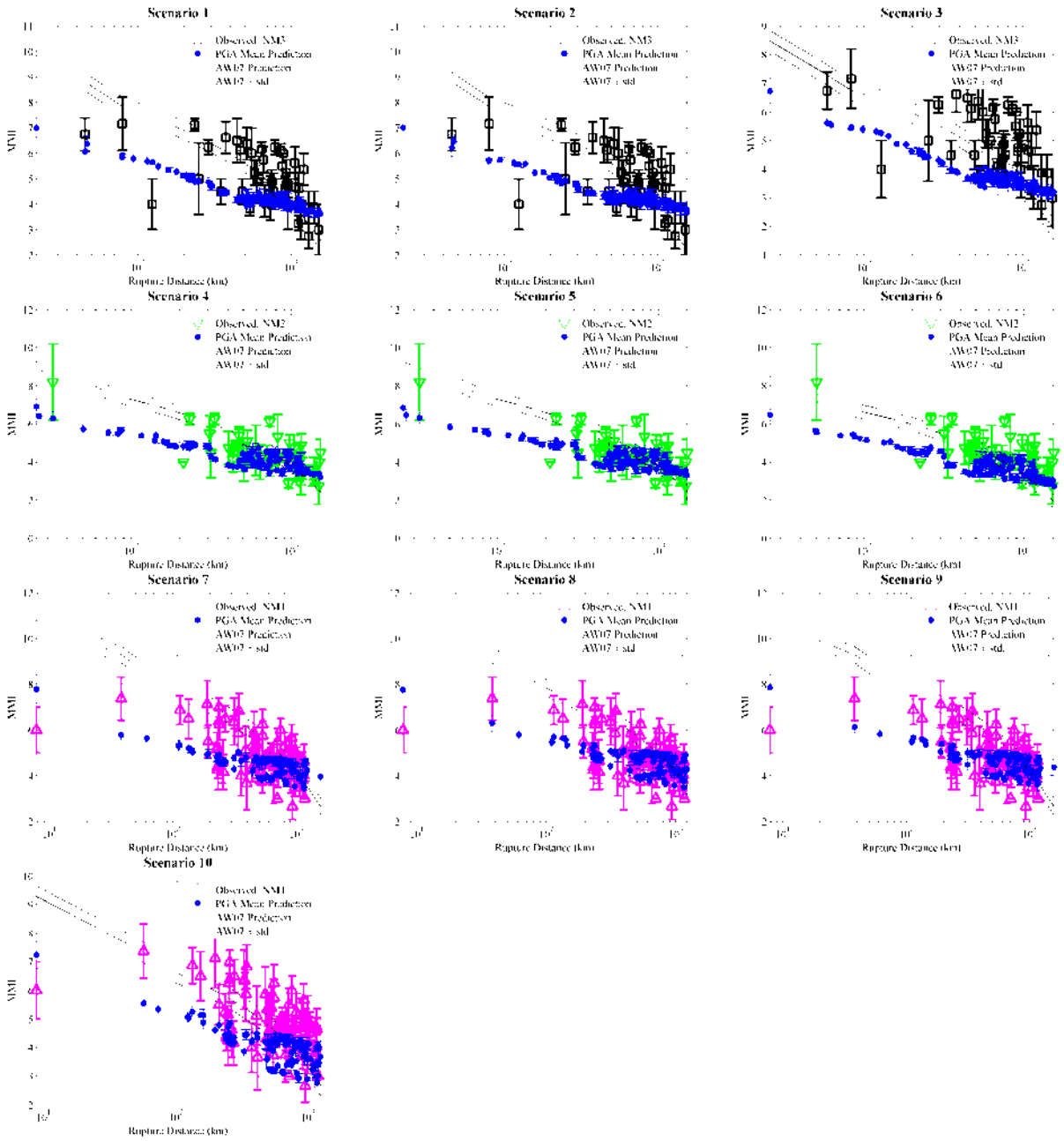

Figure 20. Converted MMI values for Scenarios 1 through 10 using simulated PGAs and the DC11 GMICE. The average and one standard deviation of the converted MMI values for the geometric mean of the two horizontal components are calculated at each site over multiple source realizations and shown with filled circle and vertical bars. The empirical MMI values using the AW07 GMPE plus and minus one standard deviation are shown with solid and dashed lines. The observed MMIs for the three New Madrid events are plotted in magenta, green, and black. The vertical bars in the observations correspond to the standard deviation of the average (as interpreted by the four experts) MMI values.

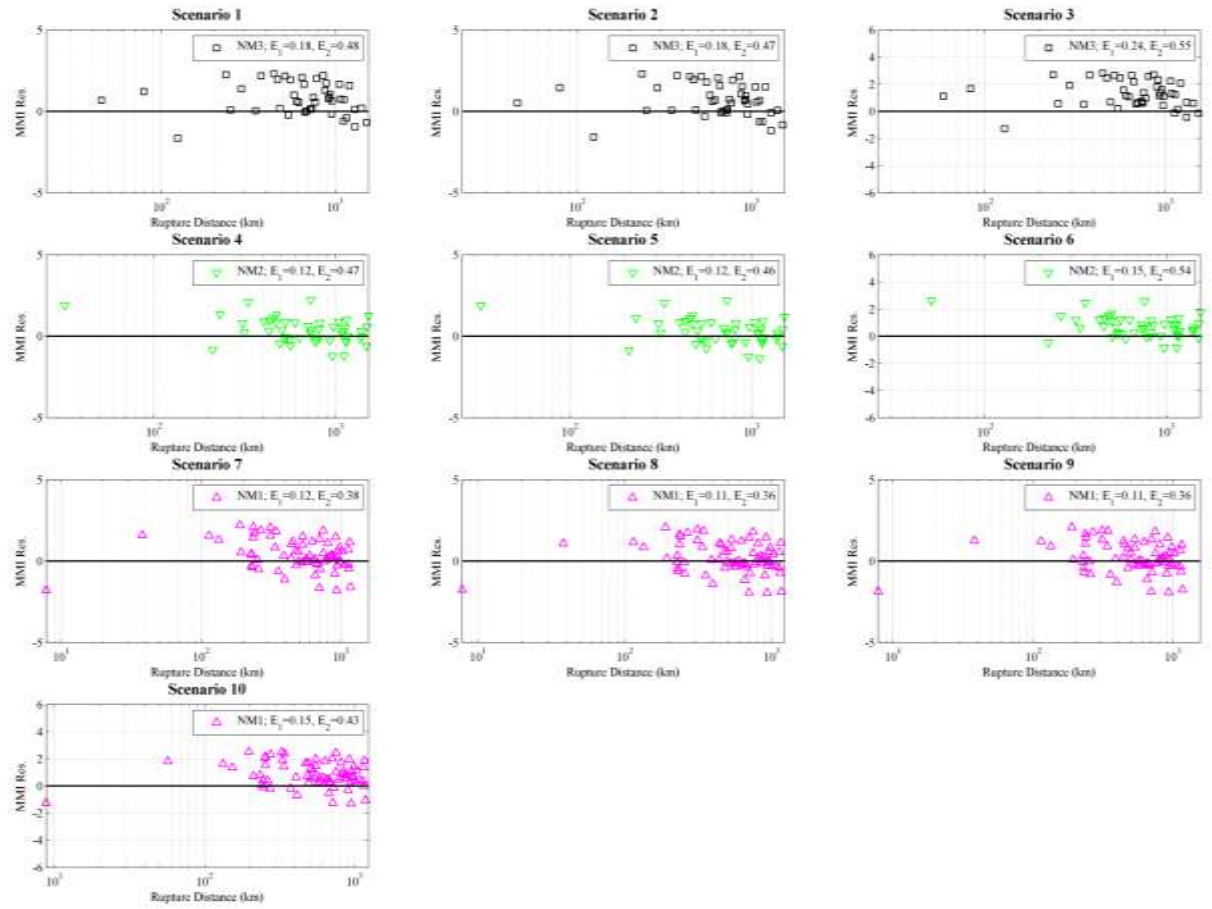

Figure 21. Residuals associated with Figure 20 showing the difference between observed intensities and median predicted ones for NM1, NM2, and NM3 events. The errors listed in the plots legends refer to the root mean square (RMS) error between observed and simulated intensities (E_1), and RMS error between observed intensities and prediction from the AW07 attenuation model (E_2).

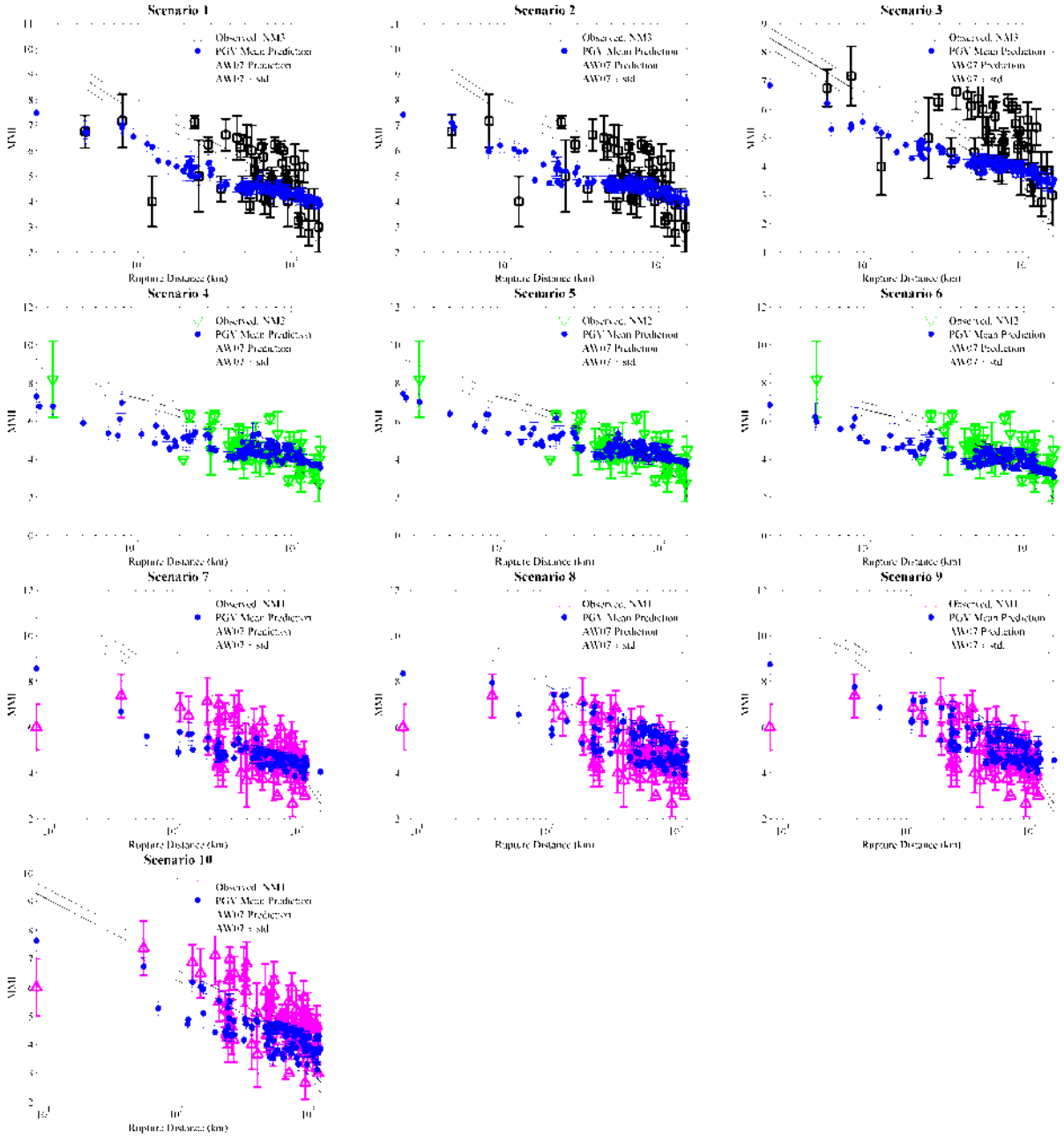

Figure 22. Converted MMI values for Scenarios 1 through 10 using simulated PGVs and the AK07 GMICE where magnitude is considered unknown. The average and one standard deviation of the converted MMI values for the geometric mean of the two horizontal components are calculated at each site over multiple source realizations and shown with filled circle and vertical bars. The empirical MMI values using the AW07 GMPE plus and minus one standard deviation are shown with solid and dashed lines. The observed MMIs for the three New Madrid events are plotted in magenta, green, and black. The vertical bars in the observations correspond to the standard deviation of the average (as interpreted by the four experts) MMI values.

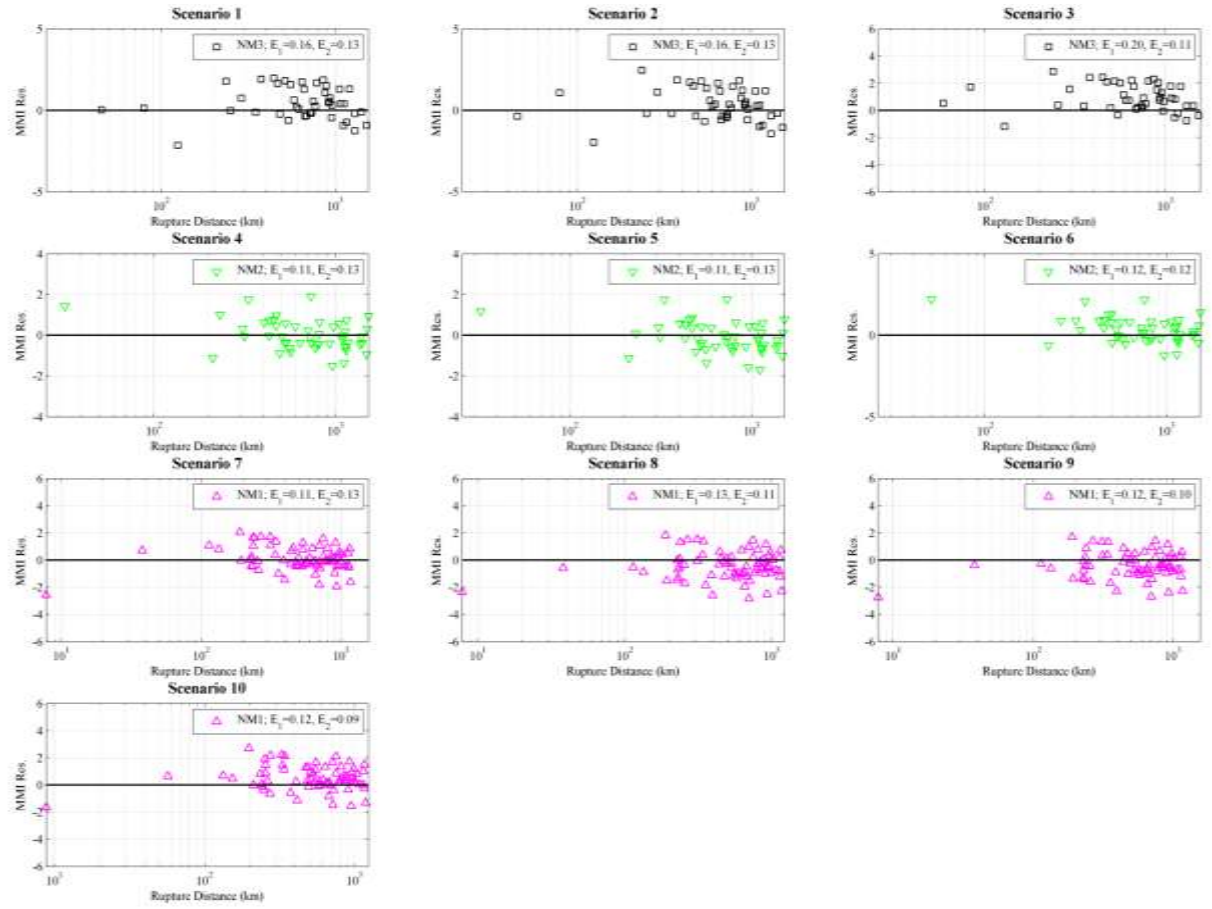

Figure 23. Residuals associated with Figure 22 showing the difference between observed intensities and median predicted ones for NM1, NM2, and NM3 events. The errors listed in the plots legends refer to the root mean square (RMS) error between observed and simulated intensities (E_1), and RMS error between observed intensities and prediction from the AW07 attenuation model (E_2).

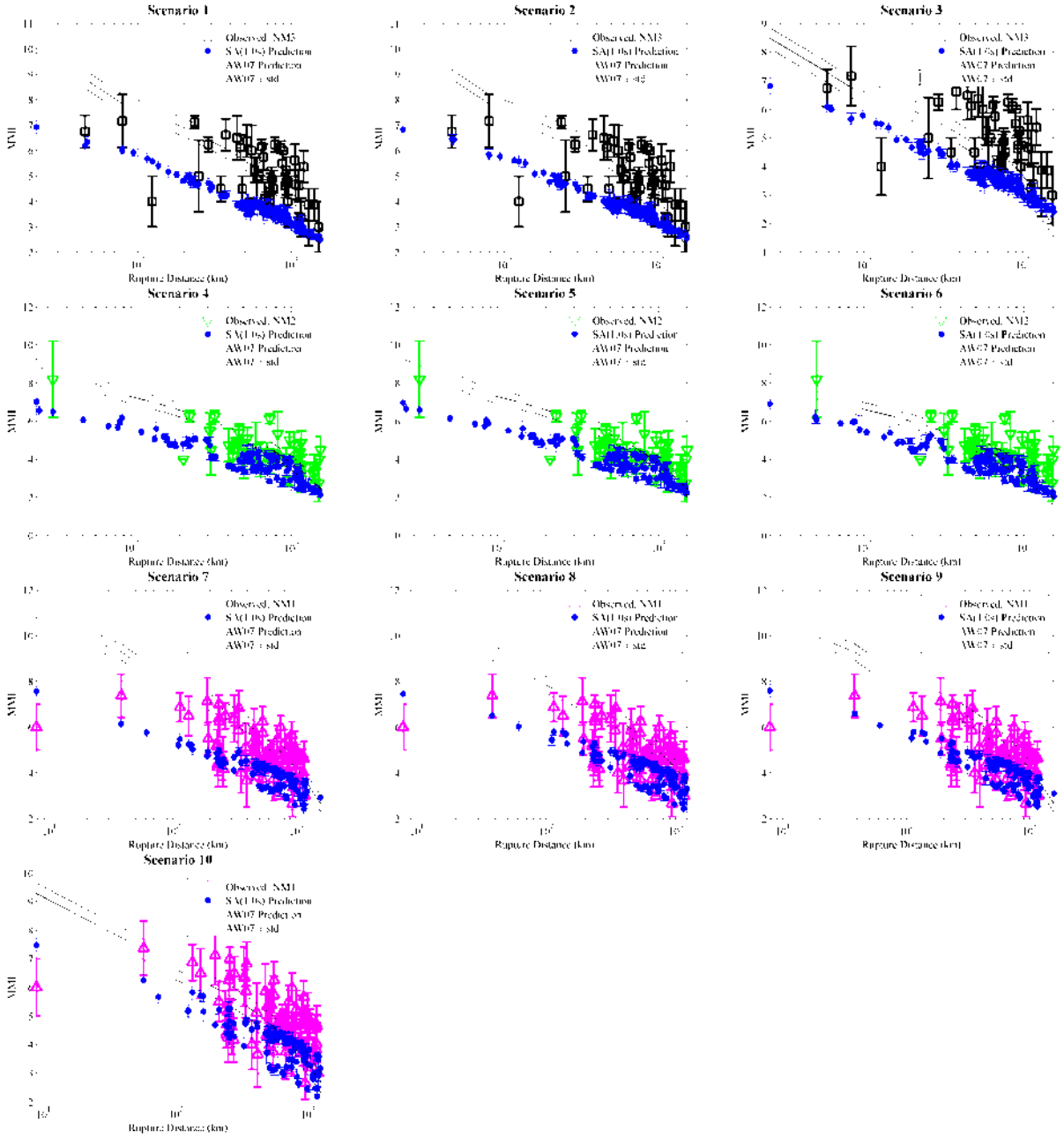

Figure 24. Converted MMI values for Scenarios 1 through 10 using simulated 1.0 s spectral accelerations and the DC11 GMICE. The average and one standard deviation of the converted MMI values for the geometric mean of the two horizontal components are calculated at each site over multiple source realizations and shown with filled circle and vertical bars. The empirical MMI values using the AW07 GMPE plus and minus one standard deviation are shown with solid and dashed lines. The observed MMIs for the three New Madrid events are plotted in magenta, green, and black. The vertical bars in the observations correspond to the standard deviation of the average (as interpreted by the four experts) MMI values.

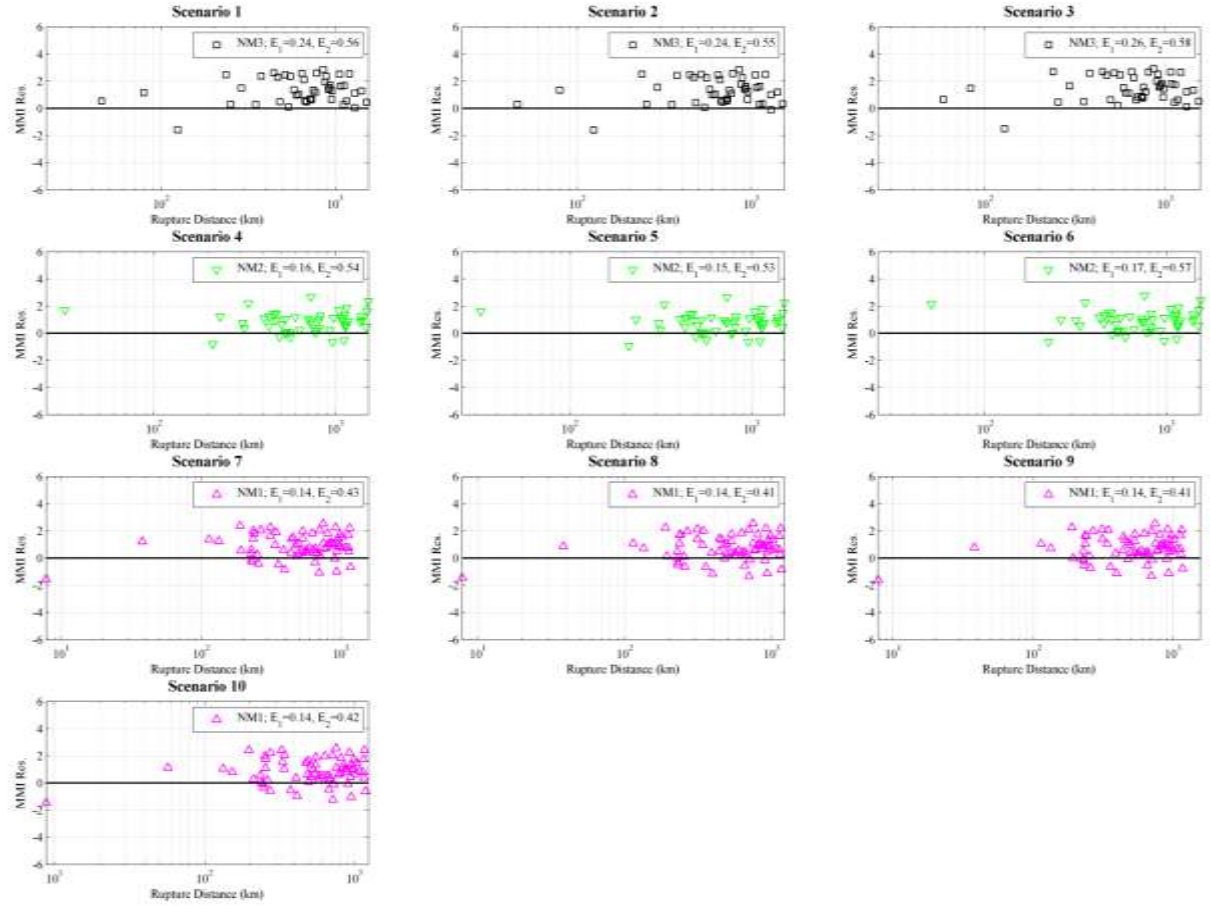

Figure 25. Residuals associated with Figure 24 showing the difference between observed intensities and median predicted ones for NM1, NM2, and NM3 events. The errors listed in the plots legends refer to the root mean square (RMS) error between observed and simulated intensities (E_1), and RMS error between observed intensities and prediction from the AW07 attenuation model (E_2).

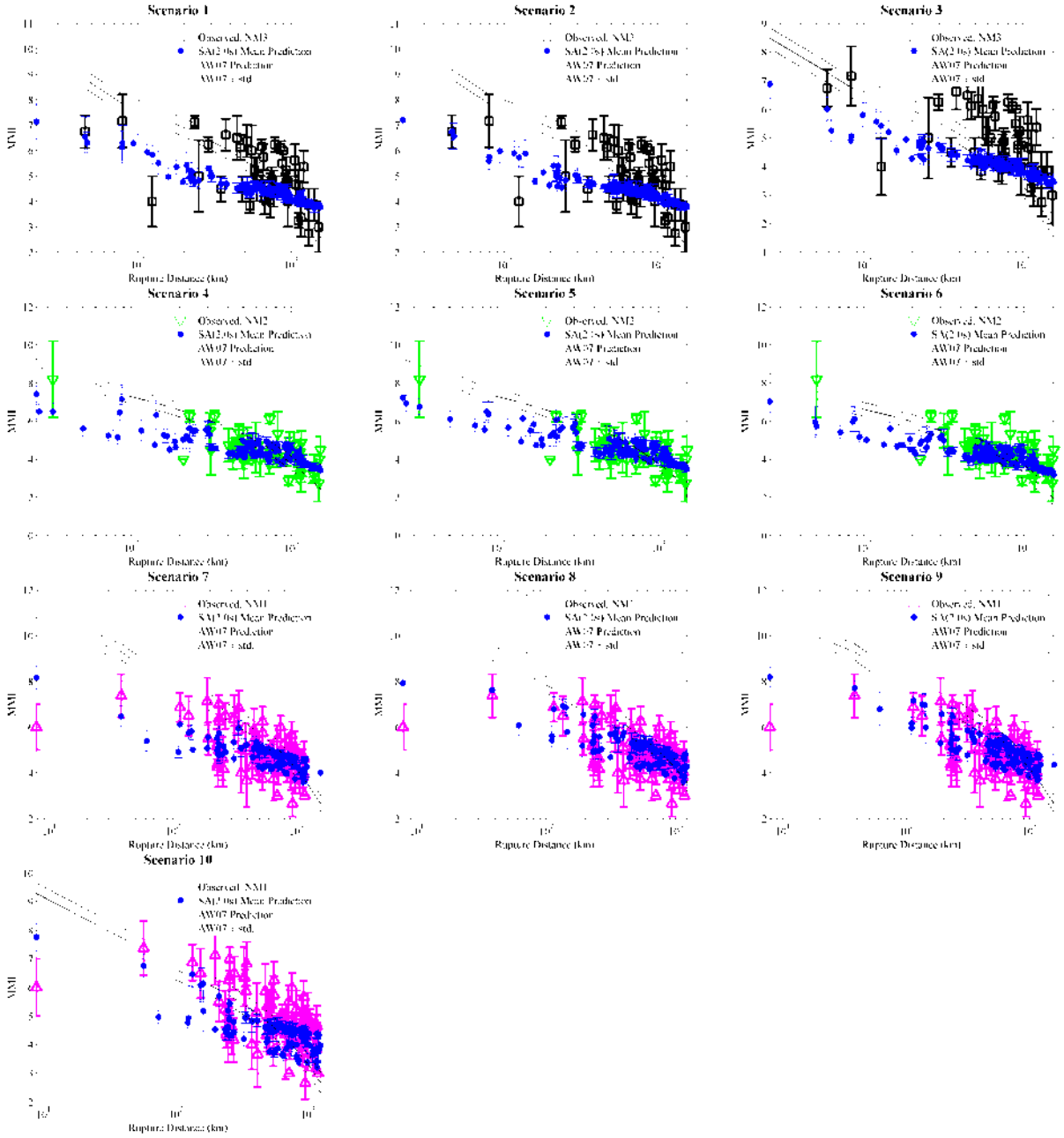

Figure 26. Converted MMI values for Scenarios 1 through 10 using simulated 2.0 s spectral accelerations and the AK07 GMICE where magnitude is considered unknown. The average and one standard deviation of the converted MMI values for the geometric mean of the two horizontal components are calculated at each site over multiple source realizations and shown with filled circle and vertical bars. The empirical MMI values using the AW07 GMPE plus and minus one standard deviation are shown with solid and dashed lines. The observed MMIs for the three New Madrid events are plotted in magenta, green, and black. The vertical bars in the observations correspond to the standard deviation of the average (as interpreted by the four experts) MMI values.

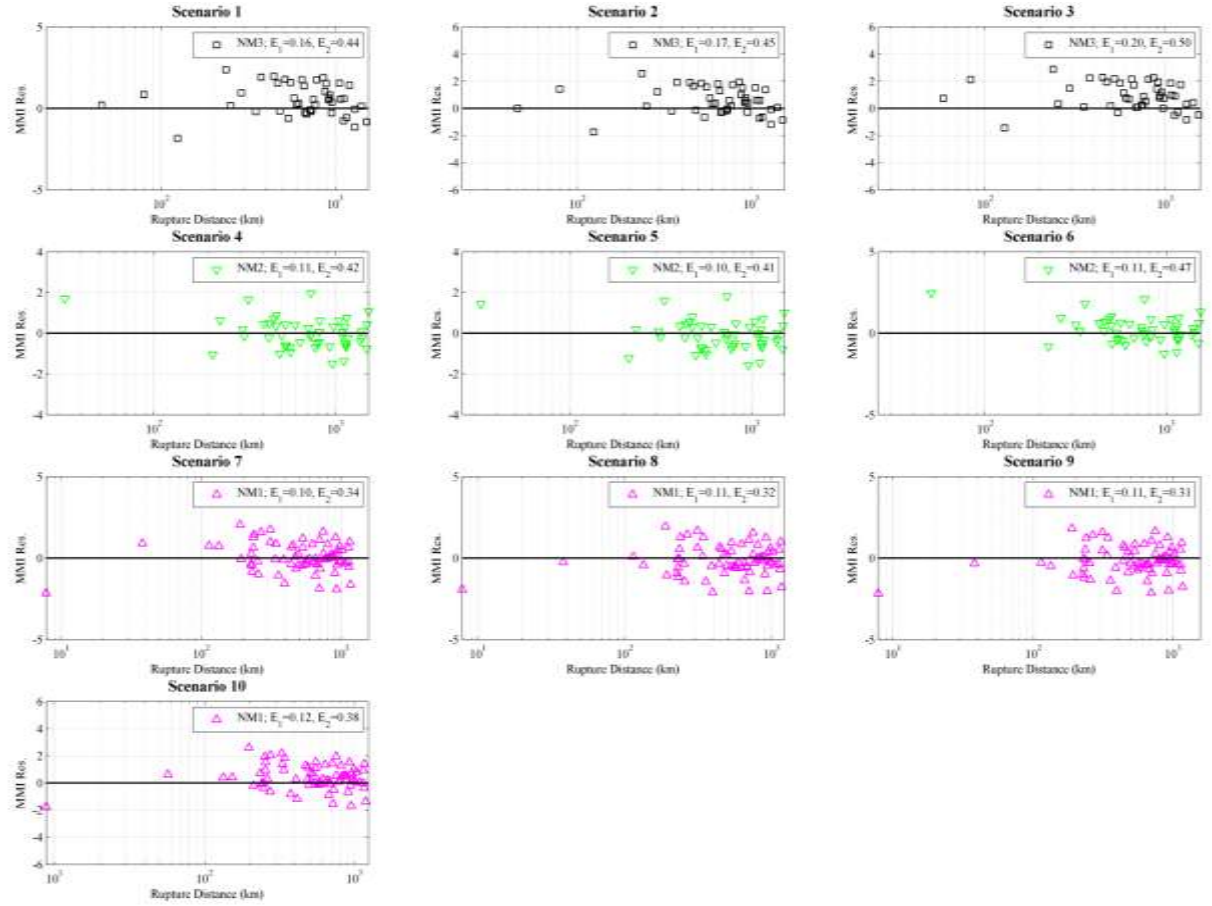

Figure 27. Residuals associated with Figure 26 showing the difference between observed intensities and median predicted ones for NM1, NM2, and NM3 events. The errors listed in the plots legends refer to the root mean square (RMS) error between observed and simulated intensities (E_1), and RMS error between observed intensities and prediction from the AW07 attenuation model (E_2).

Table 6. The RMS error between observed and simulated intensities using the AK07 GMICE. Minimum errors are marked in green.

Scenario	Fault Segment	Event Code	M_W	Length (km)	Width (km)	Atkinson and Kaka (2007) - AK07					
						PGA	PGV	SA (0.3 s)	SA (1.0 s)	SA (2.0 s)	Mean
1	Central	NM3	7.6	60	40	0.3295	0.1566	0.3455	0.2314	0.1609	0.2576
2			7.6	60	40	0.3218	0.1560	0.3380	0.2283	0.1650	0.2536
3			7.0	30	22	0.3837	0.2001	0.3969	0.2629	0.1983	0.3011
4	Northern	NM2	7.4	70	22	0.2396	0.1059	0.2563	0.1489	0.1056	0.1831
5			7.4	70	22	0.2333	0.1067	0.2497	0.1433	0.1044	0.1787
6			7.0	40	15	0.2806	0.1188	0.2957	0.1680	0.1125	0.2103
7	Southern	NM1	7.7	140	22	0.2166	0.1071	0.2274	0.1490	0.1030	0.1691
8			7.7	140	22	0.2026	0.1326	0.2146	0.1396	0.1071	0.1647
9			7.7	140	22	0.2043	0.1247	0.2171	0.1393	0.1074	0.1645
10			7.0	40	15	0.2507	0.1221	0.2614	0.1609	0.1167	0.1927

Table 7. The RMS error between observed and simulated intensities using the DC11 GMICE. Minimum errors are marked in green.

Scenario	Fault Segment	Event Code	M_W	Length (km)	Width (km)	Donguka and Cramer (2011) - DC11					
						PGA	PGV	SA (0.3 s)	SA (1.0 s)	SA (2.0 s)	Mean
1	Central	NM3	7.6	60	40	0.184	0.1722	0.3192	0.2409	0.1519	0.2220
2			7.6	60	40	0.1787	0.1864	0.3105	0.2362	0.1533	0.2202
3			7.0	30	22	0.2402	0.1452	0.3718	0.2578	0.1427	0.2465
4	Northern	NM2	7.4	70	22	0.1186	0.1912	0.2334	0.1573	0.1766	0.1795
5			7.4	70	22	0.1159	0.2067	0.2265	0.1506	0.1835	0.1810
6			7.0	40	15	0.1496	0.1483	0.2727	0.1666	0.1551	0.1847
7	Southern	NM1	7.7	140	22	0.1184	0.1588	0.2036	0.1448	0.1436	0.1564
8			7.7	140	22	0.1139	0.2006	0.1903	0.1359	0.155	0.1624
9			7.7	140	22	0.1133	0.196	0.1926	0.1356	0.155	0.1617
10			7.0	40	15	0.1465	0.1232	0.2385	0.145	0.1244	0.1613

4.6 Comparison of Simulation-based Intensities with Ramirez-Guzman et al. (2015) Results

Figure 28 shows the simulation-based estimates of the intensities of NM3 obtained by Ramirez-Guzman et al. (2015) using the AK07 and DC11 GMICE compared not with the observations but with the predictions of the Bakun and Hopper (2004) intensity attenuation model for two magnitudes, 7.6 and 7.0. These simulations show trends similar to those we see in even numbered Figures 20-26. Figure 29 shows

the trend of MMI values with distance predicted from Sa at 1.0 and 2.0 seconds using DC11 and AK07 and is comparable to Figure 28.

The trends for the other two events in Figures 20-26, NM2 (second row, northern segment) and NM1 (third and fourth rows, southern segment) are similar to those for NM3. We have already noted in Figure 4 that the attenuation with distance for NM3, the central thrust faulting event, is more dispersed in the distance range of 200 to 1200 km than it is for the two strike-slip events NM1 and NM2. Despite this difference between the events in the observations, we do not see this difference between the events in our simulations. Similarly, we do not see evidence for this difference between NM3 (their Figure 12) and NM1 (their Figure 9) in the results of Ramirez-Guzman et al. (2015). We conclude that the MMI estimates derived for our 1D simulations of NM3, and those derived by Ramirez-Guzman et al. (2015) from their 3D simulations of NM3, are not compatible with the observed intensities of that event.

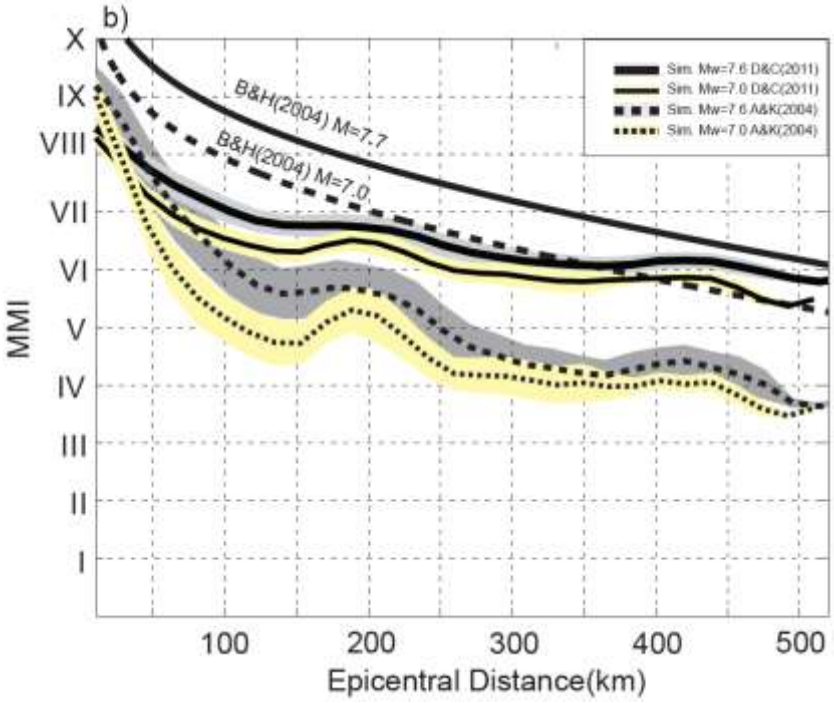

Figure 28. MMI attenuation for NM3 events from simulations using the AK07 and DC11 GMICEs compared with the predictions of the Bakun and Hopper (2004) model for two magnitudes: 7.6 and 7.0. (Source: Ramirez-Guzman et al., 2015).

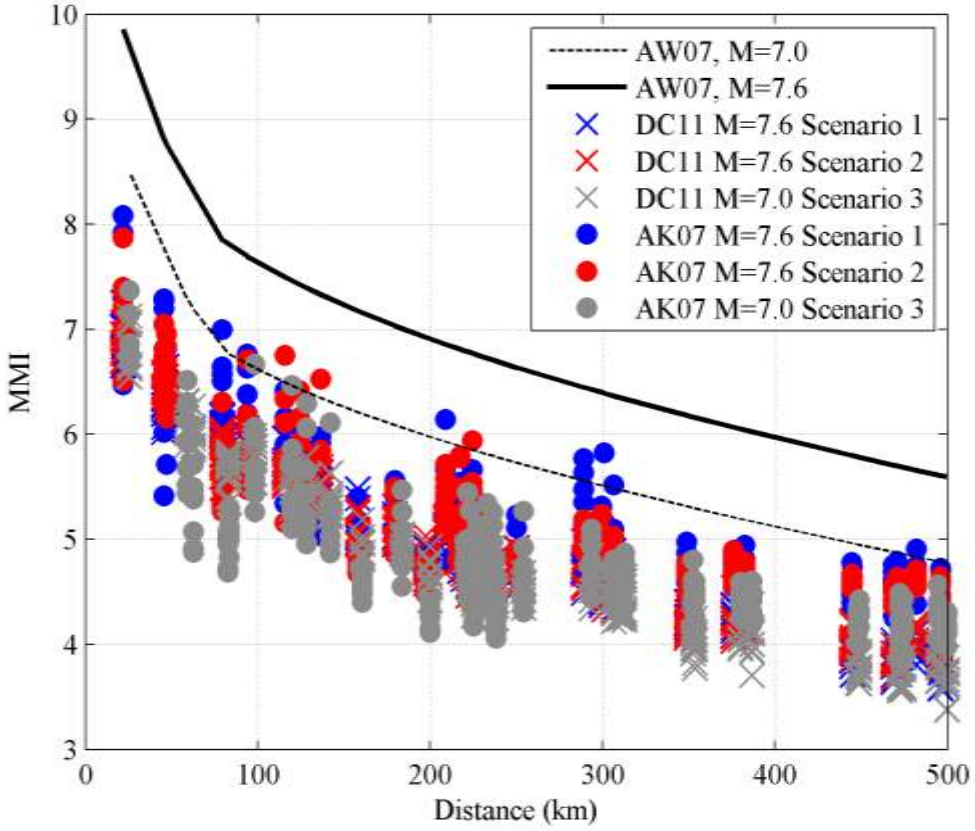

Figure 29. MMI attenuation for NM3 events (scenarios 1 through 3) from simulations using the DC11 for T=1.0 sec and AK07 for T = 2.0 sec Sa compared with the predictions of the AW07 model for two magnitudes 7.6 and 7.0.

5. Conclusions

The historic 1811 and 1812 earthquakes in the New Madrid Seismic Zone have large uncertainties whose values range between 7.1 and 8.0 (Petersen et al., 2008). Such uncertainty in the ground motion level affects the seismic hazard at regional and local levels. For this reason, improvements in our knowledge of the historic events' magnitudes offer an alternative to previous work on seismic hazard in the area.

This objective of this project is to provide improved estimates of the magnitudes of the three main events of the sequence by comparing MMI values derived from broadband simulations with the observed intensities. This research complements the work of Ramirez-Guzman et al. (2015) where they used 3D simulations out to distances of about 500 km. Our research used 1D simulations out to 1,800 km to span the entire region over which MMI intensities were reported.

Hough and Page (2011) corrected their intensities for site effects. We checked these corrected intensities for bias using the Wald and Allen (2007) method of estimating V_{S30} as a measure of site amplification.

We found no residual dependence of the observed MMI on V_{S30} after correcting the observed MMI for distance using the Atkinson and Wald (2007) intensity prediction equation. We also found no evidence for a regional dependence of residual intensity on distance from the New Madrid Seismic zone in the site condition corrected MMI data. We inspected the observed MMI data for the attenuation of intensities with distance and compared them with Bakun and Hopper (2004) model 3 and the Atkinson and Wald (2007). Predicted intensities from Atkinson and Wald (2007) show a better agreement with the observed MMI data.

We used the Southern California Earthquake Center (SCEC) Broadband Simulation Platform (BBP) to perform the simulations. We used two ground motion intensity correlation equations (GMICEs) to estimate MMI from the ground motion simulations so that they could be compared with the observed intensities. These two GMICEs include the Atkinson and Kaka (2007) and Dangkua and Cramer (2011). Our simulations consisted of multiple scenarios with two magnitudes for each branch of the New Madrid fault. The two magnitudes for scenario events include a magnitude 7.0 and a larger magnitude for each fault branch and we compared simulations of larger magnitudes with those of magnitude 7 scenario events. For the larger magnitudes, the NM1 scenarios (December 16, 1811) had a magnitude of 7.7, the NM2 scenarios (January 23, 1812) had a magnitude of 7.4, and the NM3 scenarios (February 7, 1812) had a magnitude of 7.6. Although there is a large degree of discrepancy between the observed and simulated intensities, there is a slight preference for the larger magnitudes, which are systematically higher than those described by Hough and Page (2011) and comparable to those reported by Cramer and Boyd (2014).

The dispersion of the observed MMI intensity for NM3, the central thrust faulting event, is much larger in the distance range of 200 to 1200 km than it is for the two strike-slip events (NM1 and NM2). Despite this difference between the events in the observations, we do not see this difference between the events in our simulations. Similarly, we do not see evidence for this difference between NM3 and NM1 in the results of Ramirez-Guzman et al. (2015). We conclude that there may be factors influencing the observed MMI intensities of the three events that our simulations are not modeling.

6. Acknowledgements

We would like to thank Robert Graves from the U.S. Geological Survey for providing codes, information, and guidance in the broadband simulation process. In addition, we thank Tom Jordan, Phil Maechling, and Fabio Silvia for providing access to the SCEC Broadband Strong Ground Motion Simulation Platform and for providing computational resources on the High Performance Computing units of the University of Southern California. We also thank Leonardo Ramirez-Guzman for his useful comments on this report. This research was supported by the U.S. Geological Survey (USGS), Department of the Interior, under USGS award number G14AP00008.

7. References

Allen, T. I., and D. J. Wald (2007). Topographic Slope as a Proxy for Seismic Site Conditions (Vs30) and Amplification around the Globe, U.S. Geological Survey, *Open File Report 2007-1357*, 69 pp.

Allen, T. I. and D. J. Wald (2009). On the Use of High-Resolution Topographic Data as a Proxy for Seismic Site Conditions (VS30), *Bull. Seism. Soc. Am.*, Vol. 99, No. 2A, pp. 935-943.

Atkinson, G., and D. Boore (2006). Earthquake ground-motion prediction equations for eastern North America, *Bull. Seismol. Soc. Am*. 96, 2181–2205

Atkinson, G. and S. Kaka (2007). Relationships between felt intensity and instrumental ground motions for earthquakes in the central United States and California. *Bull. Seism. Soc. Am.*, 97, 497-510.

Atkinson, G. M., and D. J. Wald (2007) "Did You Feel It?" intensity data: A surprisingly good measure of earthquake ground motion, *Seism. Res. Lett*. 78, 362-368

Bakun, W.H, and M.G. Hopper (2004). Magnitudes and Locations of the 1811-1812 New Madrid, Missouri, and the 1886 Charleston, South Carolina, Earthquake, *Bull. Seismol. Soc. Am.*, 94-1, 64–75.

Bakun, W. H., A. C. Johnston, and M. G. Hopper (2002). Modified Mercalli intensities (MMI) for large earthquakes near New Madrid, Missouri, in 1811–1812 and near Charleston, South Carolina, in 1886, *U.S. Geol. Surv. Open-File Rept. 02-184,* 31 pp.

Bakun, W. H. Wentworth, C. M. (1997). Estimating earthquake location and magnitude from seismic intensity data, *Bull. Seism. Soc. Am.,* 87, 1502- 1521

Beresnev, I. A. and G. M. Atkinson (1997). Modeling finite-fault radiation from the ω^n spectrum, *Bull. Seism. Soc. Am.*, 87, 67-84.

Boore, D. M. (1983), Stochastic Simulation of High-frequency Ground Motions Based on Seismological Models of the Radiated Spectra, *Bull. Seismol. Soc. Am.*, 73, 1865–1894.

Cramer, C.H., and O.S. Boyd (2014). Why the New Madrid earthquakes are M7-8 and the Charleston earthquake is ~M7, *Bull. Seis. Soc. Am.*, 104 (4).

Dangkua, D.T., and C.H. Cramer (2011). Felt Intensity versus Instrumental Ground Motion: A Difference between California and Eastern North America?, *Bull. Seismol. Soc. Am.*, 101-4, 1847–1858

Farr, T. G., and M. Kobrick (2000). Shuttle Radar Topography Mission produces a wealth of data, *EOS Trans. AGU,* 81, 583-585.

Frankel, A. (1995). Simulating strong motions of large earthquakes using recordings of small earthquakes: The Loma Prieta mainshock as a test case, *Bull. Seismol. Soc. Am.*, 85, 1144–1160.

Graves, R.W., and A. Pitarka (2010). Broadband Ground-Motion Simulation Using a Hybrid Approach, *Bull. Seismol. Soc. Am.*, 100-5A, 2095–2123.

Hartzell, S., S. Harmsen, A. Frankel, and S. Larsen (1999). Calculation of broadband time histories of ground motion: Comparison of methods and validation using strong-ground motion from the 1994 Northridge earthquake, *Bull. Seismol. Soc. Am.*, 89, 1484–1504.

Hosseini, S. M., S. Pezeshk, A. Haji-Soltani, and M. Chapman. (2015). Investigation of Attenuation of The Fourier Amplitude in the Caribbean Region. *Bull. Seismol. Soc. Am.*, 105 (2A), April, 734-744

Hosseini, S. M., and S. Pezeshk. (2015). A Synthetic Study into the Nature and Solution of Nonuniqueness in Surface-Wave Inverse Problems *Bull. Seismol. Soc. Am.*, 105, pp. 3167-3179

Hough, S.E., Armbruster, J.G., Seeber, L., and J.F. Hough (2000). On the Modified Mercalli intensities and magnitudes of the 1811-1812 New Madrid earthquakes, *J. Geophys. Res.*, 105-B10,23839-23864.

Hough, S. E., and M. Page (2011). Toward a consistent model for strain accrual and release for the New Madrid Seismic Zone, central United States, *J. Geophys. Res*. 116, B03311.

Johnston, A. C. (1996). Seismic moment assessment of earthquakes in stable continental regions III, New Madrid 1811–1812, Charleston1886, and Lisbon 1755, *Geophys. J. Int*. 126, 314–344.

Kaka, S. and G. Atkinson (2004). Relationships between instrumental intensity and ground motion parameters in eastern North America. *Bull. Seism. Soc. Am.*, 94, 1728-1736.

Kanter, L. R. (1994). Tectonic interpretation of stable continental crust. Chapter 2 in The Earthquakes of Stable Continental Regions, ed. A. C. Johnston, K. J. Coppersmith, L. R. Kanter, and C. A. Cornell, vol. 1, 1–98. Report for Electric Power Research Institute (EPRI), Palo Alto, CA, EPRI TR 102261.

Leonard, M. (2010). Earthquake fault scaling: Self-consistent relating of rupture length, width, average displacement, and moment release, *Bull. Seismol. Soc. Am.* 100, no. 5A, 1971–1988

Macpherson, K. A., E. W. Woolery, Z. Wang, and P. Liu (2010). Three dimensional long-period ground-motion simulations in the upper Mississippi embayment, *Seismol. Res. Lett*. 8, no. 2, 391–405.

Maechling, P. J., F. Silva, S. Callaghan, and T. H. Jordan (2015), SCEC Broadband Platform: System Architecture and Software Implementation, *Seismol. Res. Lett.*, 86, no. 1, doi: 10.1785/0220140125

Mueller, K., S. E. Hough, and R. Bilham (2004), Analysing the 1811‐1812 New Madrid earthquakes with recent instrumentally recorded aftershocks, *Nature*, 429, 284‐288, doi:10.1038/nature02557.

Nuttli, O.W. (1973). The Mississippi Valley earthquakes of 1811 and 1812: intensities, ground motion, and magnitudes, *Bull. Seismol. Soc. Am.* 63, 227-248.

Petersen, M. D., A. D. Frankel, S. C. Harmsen, C. S. Mueller, K. M. Haller, R. L. Wheeler, R. L. Wesson, Y. Zeng, O. S. Boyd, D. M. Perkins, N. Luco, E. H. Field, C. J. Wills, and K. S. Rukstales (2008). Documentation for the 2008 Update of the United States National Seismic Hazard Maps. *USGS Open-File Report 2008–1128*, 119 pp.

Pezeshk, S., J. Pujol and M. Hosseini (2014). Reducing Uncertainties in the Velocities Determined by Inversion of Phase Velocity Dispersion Curves by Using Synthetic Seismograms , *USGS Final Report G13AP00057*, http://earthquake.usgs.gov/research/external/reports/G13AP00057.pdf

Pezeshk, S., A. Zandieh, and B. Tavakoli. (2011). Hybrid Empirical Ground-Motion Prediction Equations for Eastern North America Using NGA Models and Updated Seismological Parameters. *Bull. Seismol. Soc. Am.*, 101(4), pp.1859-1870, August 2011, doi: 10.1785/0120100144

Ramirez-Guzman, L., R.W. Graves, K. B. Olsen, O. S. Boyd, C. Cramer, S. Hartzell, S. Ni, P. Somerville, R. A. Williams, and J. Zhong (2015). Ground-Motion Simulations of 1811–1812 New Madrid Earthquakes, Central United States, *Bull. Seism. Soc. Am.*, 105 (4), 1961-1988.

Somerville, P.G., N. Collins, N. Abrahamson, R. Graves and C. Saikia (2001). Earthquake source scaling and ground motion attenuation relations for the central and eastern United States. Final Report to the U.S. Geological Survey, Contract No. 99HQGR0098.

Tuttle, M. P., Schweig, E. S., Sims, J. D., Lafferty, R. H., Wolf, L. W., & Haynes, M. L., (2002). The earthquake potential of the New Madrid seismic zone, *Bull. Seism. Soc. Am.*, 92, 2080-2089.

Wald, D. J., P. S. Earle, and V. Quitoriano (2004). Topographic Slope as a Proxy for Seismic Site Correction and Amplification, *EOS. Trans. AGU*, 85(47), F1424.

Wald, D. J., and T. I. Allen (2007). Topographic slope as a proxy for seismic site conditions and amplification, *Bull. Seism. Soc. Am.*, Vol. 97, No. 5, 1379-1395.

Wang, C. Y. and Herrmann, R. B. (1980). A numerical study of P-, SV-, and SH-wave generation in a plane layered medium, *Bull. Seism. Soc. Am.*, 70, 1015- 1036.

Appendix A. Historic Intensity Measures of Individual Experts Overlain on V_{S30} data in CEUS

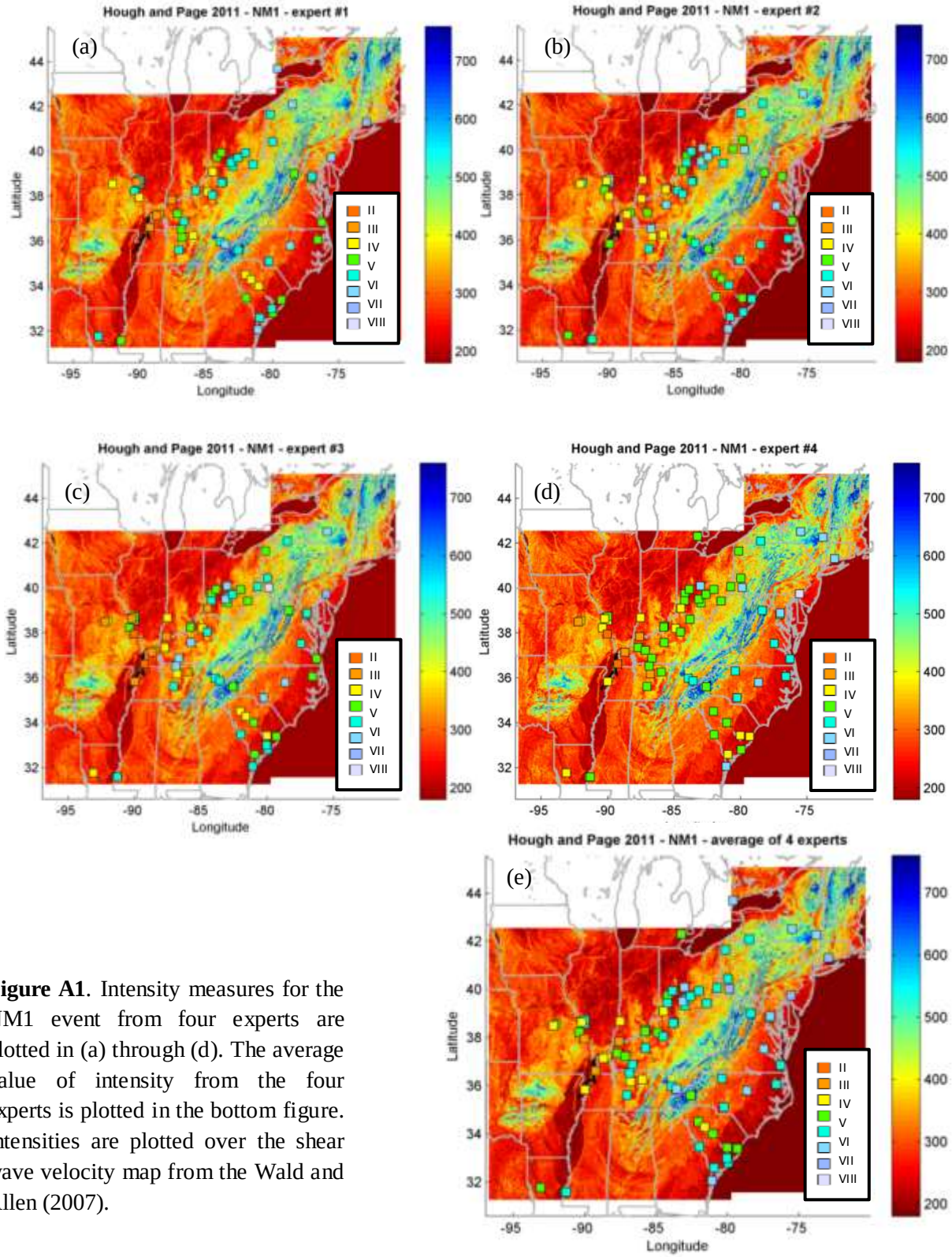

Figure A1. Intensity measures for the NM1 event from four experts are plotted in (a) through (d). The average value of intensity from the four experts is plotted in the bottom figure. Intensities are plotted over the shear wave velocity map from the Wald and Allen (2007).

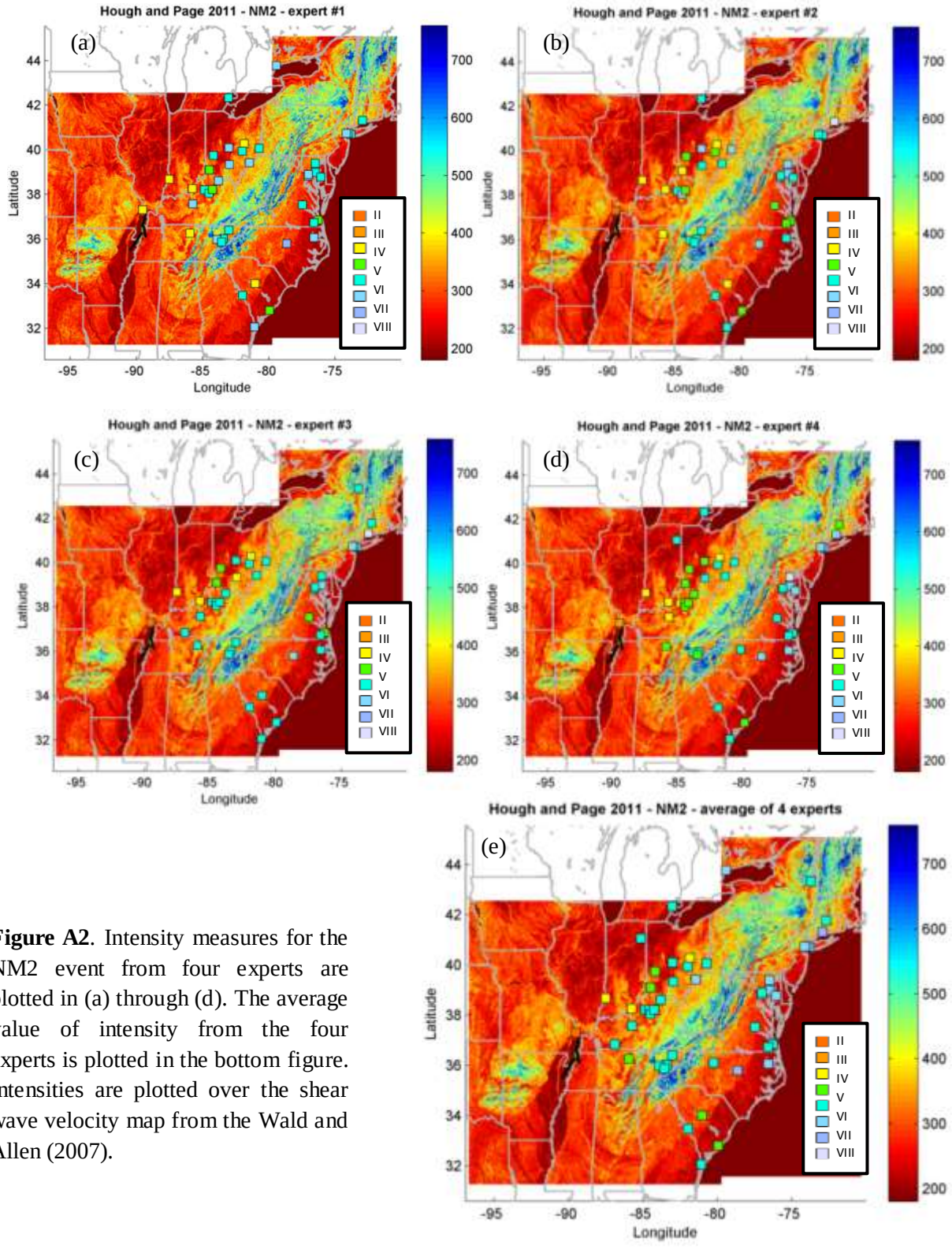

Figure A2. Intensity measures for the NM2 event from four experts are plotted in (a) through (d). The average value of intensity from the four experts is plotted in the bottom figure. Intensities are plotted over the shear wave velocity map from the Wald and Allen (2007).

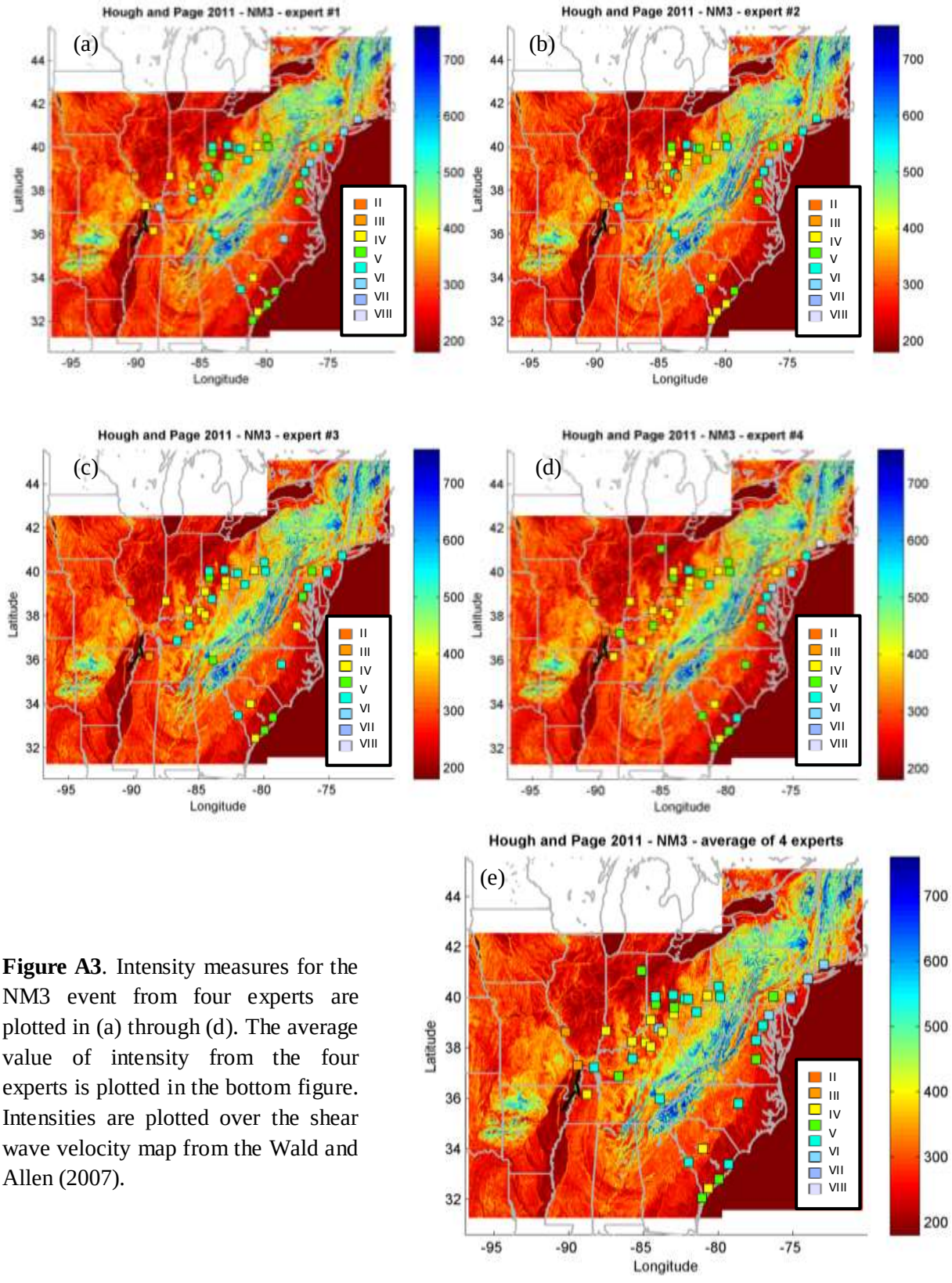

Figure A3. Intensity measures for the NM3 event from four experts are plotted in (a) through (d). The average value of intensity from the four experts is plotted in the bottom figure. Intensities are plotted over the shear wave velocity map from the Wald and Allen (2007).

Appendix B. Kinematic Rupture Models for Earthquake Scenarios 2 through 10

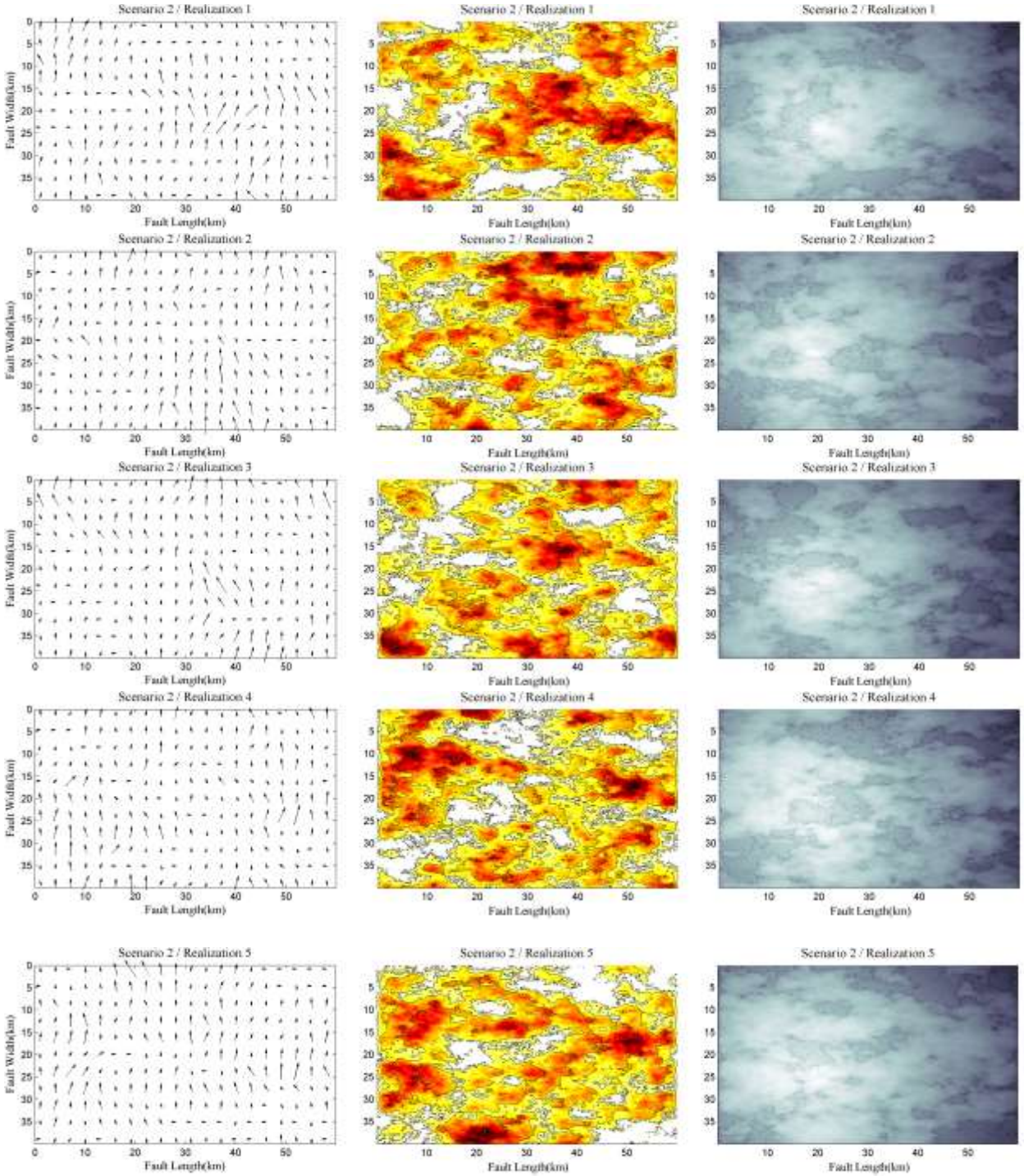

Figure B1. Kinematic rupture model developed for Central branch of New Madrid fault with M=7.6 (scenario 2). The left panel shows the distribution of average rake angles on each sub-fault over the fault plane. The middle panel shows the slip distribution with rupture front contours at 1 s intervals superimposed, and the right panel shows the distribution of slip rise time.

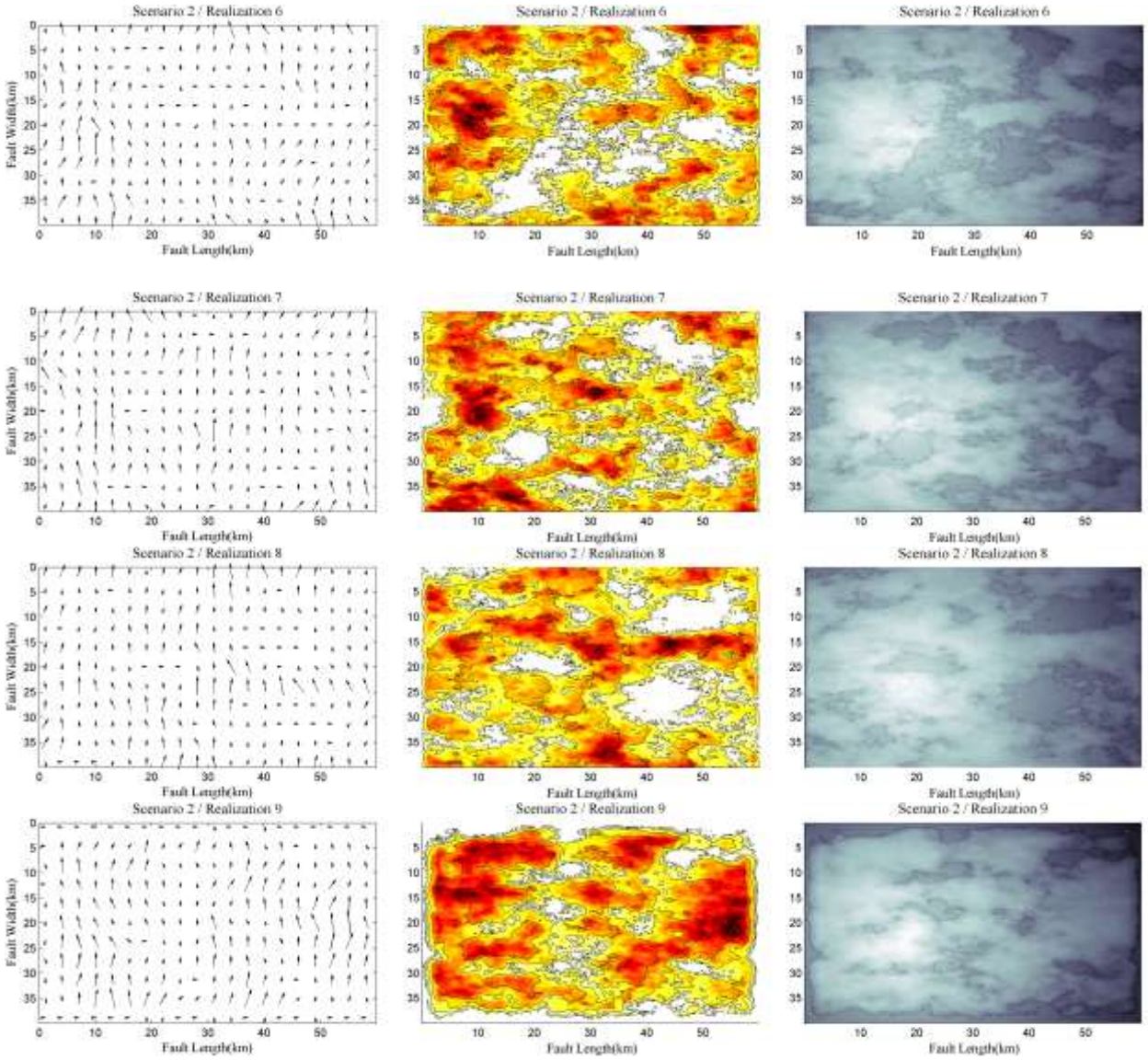

Figure B1. Continued.

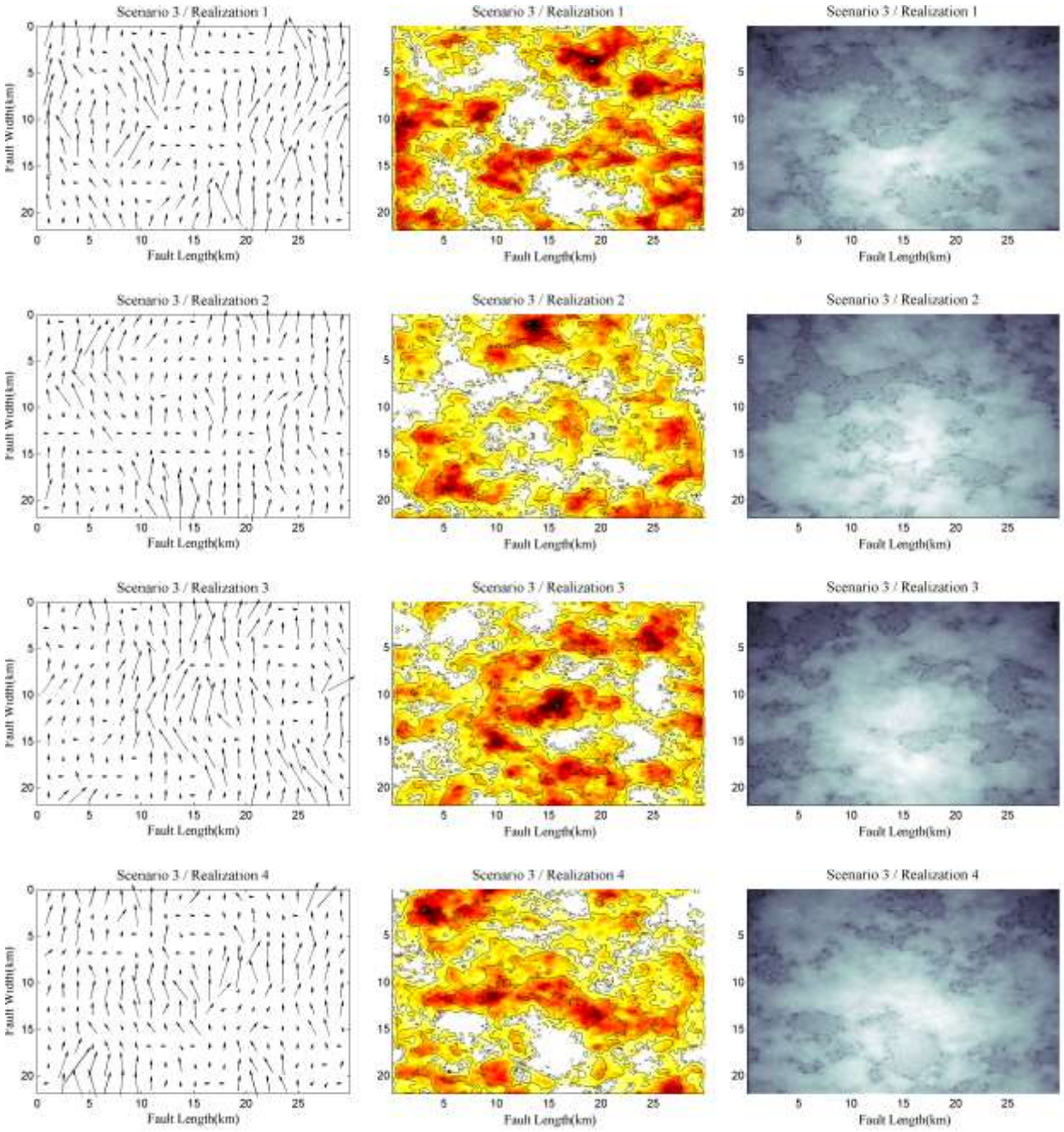

Figure B2. Kinematic rupture model developed for Central branch of New Madrid fault with M=7.0 (scenario 3). The left panel shows the distribution of average rake angles on each sub-fault over the fault plane. The middle panel shows the slip distribution with rupture front contours at 1 s intervals superimposed, and the right panel shows the distribution of slip rise time.

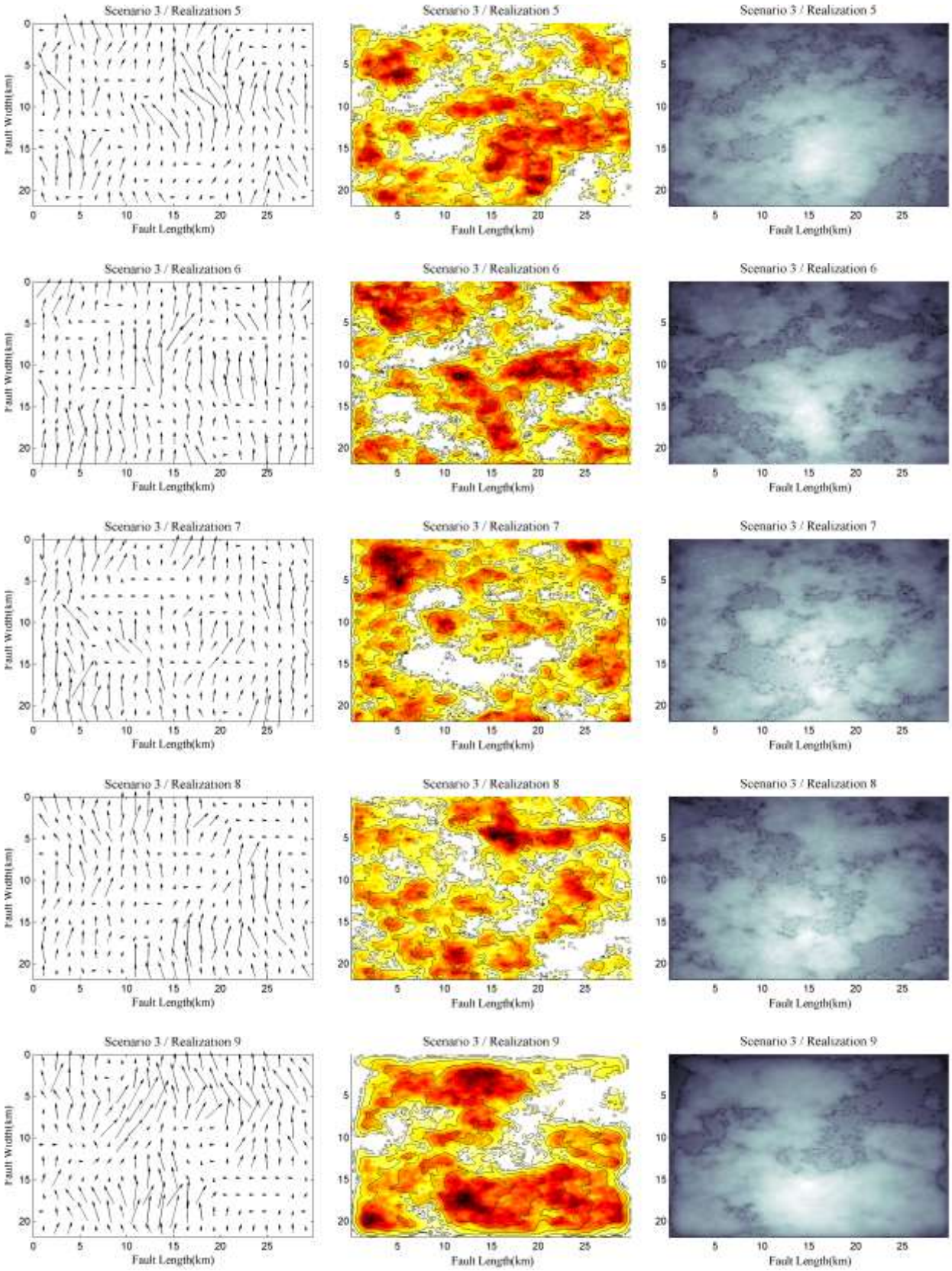

Figure B2. Continued.

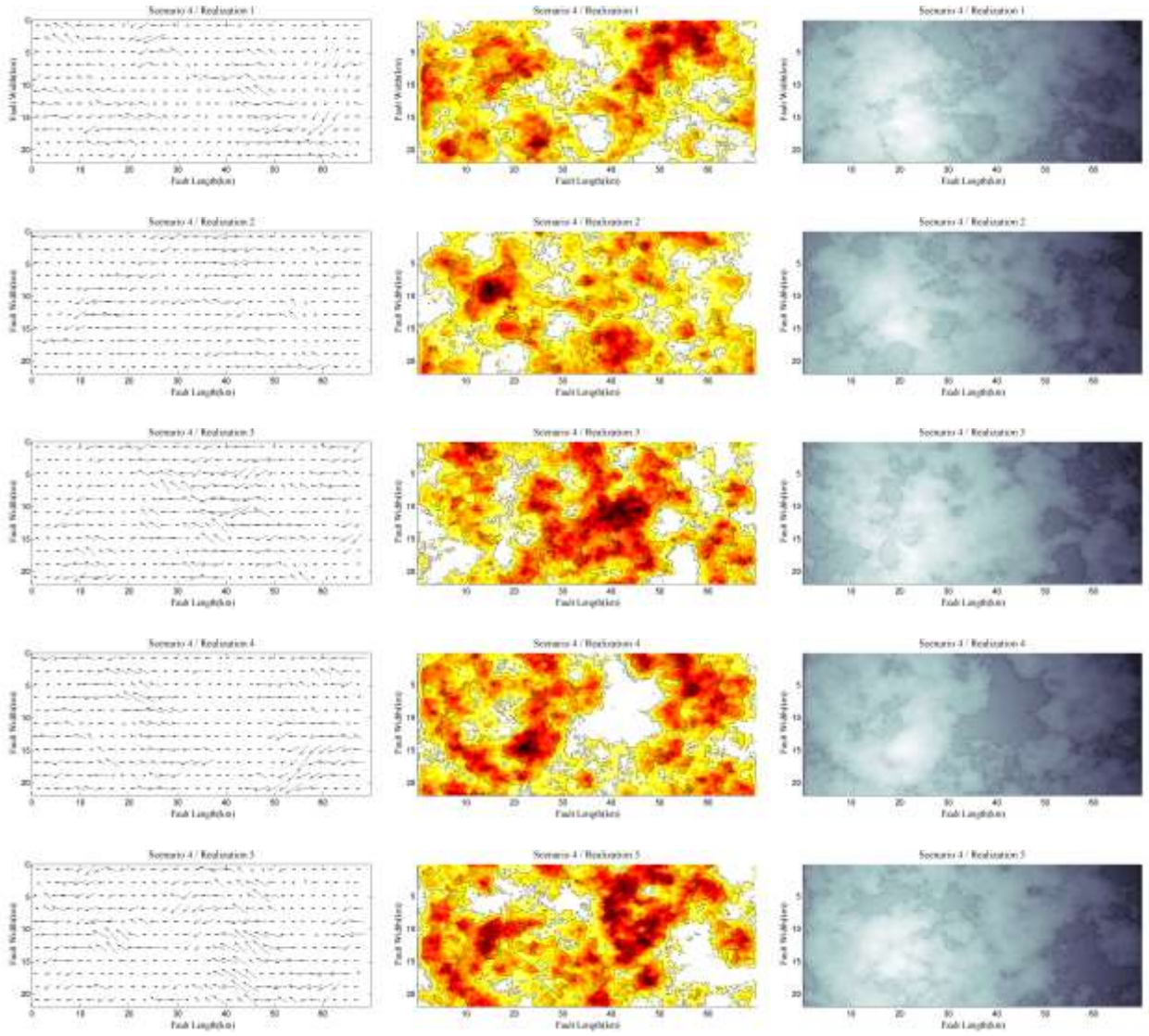

Figure B3. Kinematic rupture model developed for northern branch of New Madrid fault with M=7.4 (scenario 4). The left panel shows the distribution of average rake angles on each sub-fault over the fault plane. The middle panel shows the slip distribution with rupture front contours at 1 s intervals superimposed, and the right panel shows the distribution of slip rise time.

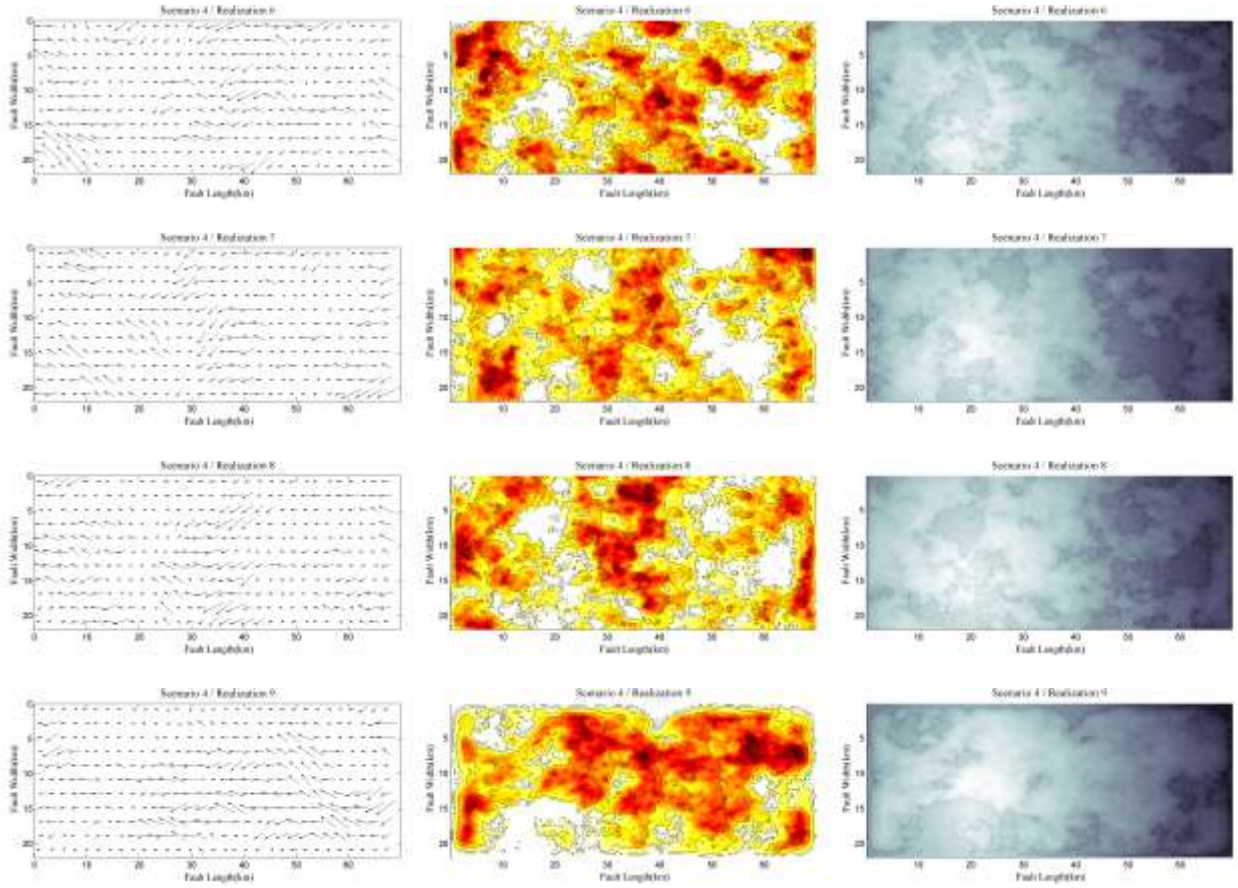

Figure B3. Continued.

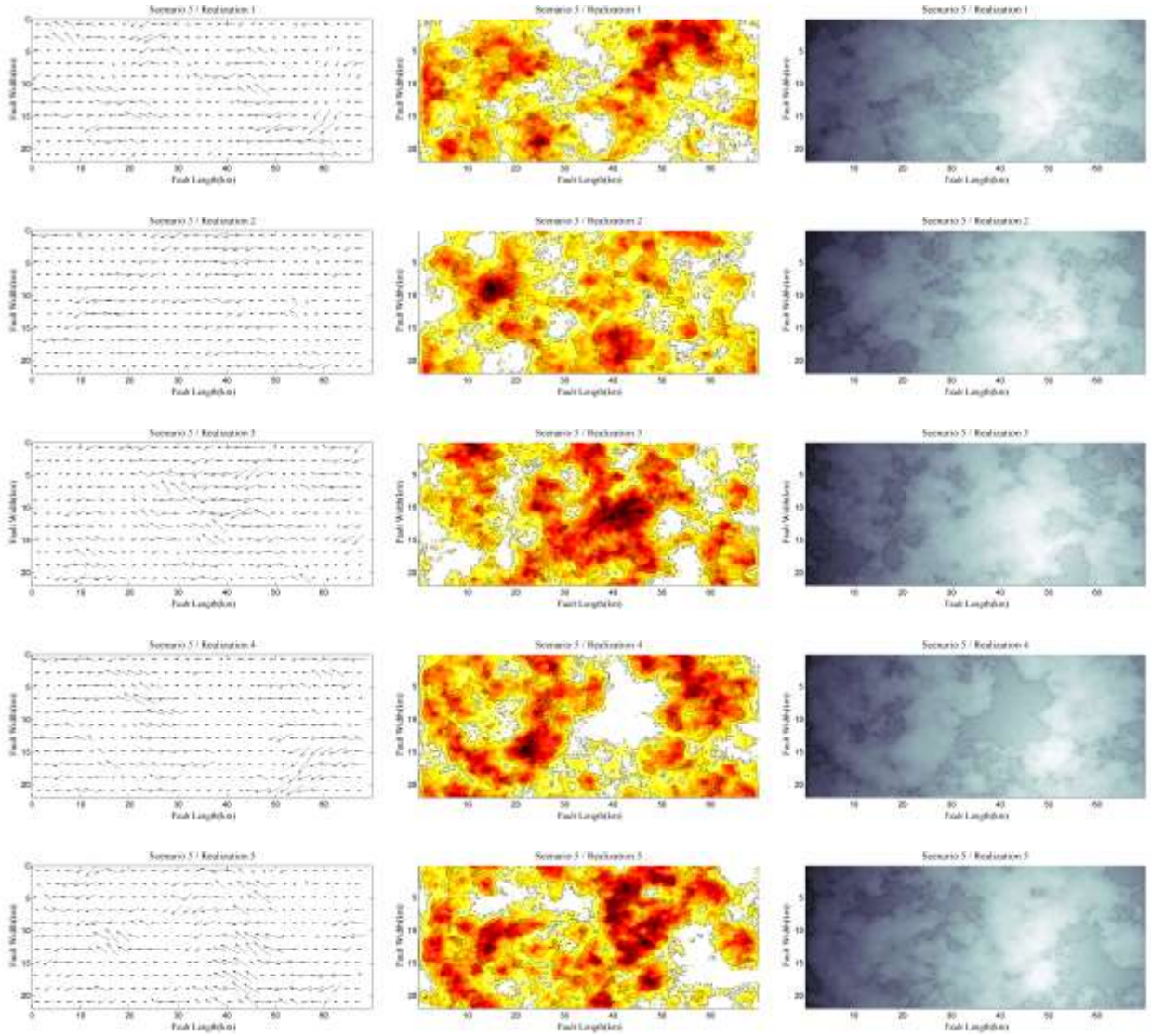

Figure B4. Kinematic rupture model developed for northern branch of New Madrid fault with M=7.4 (scenario 5). The left panel shows the distribution of average rake angles on each sub-fault over the fault plane. The middle panel shows the slip distribution with rupture front contours at 1 s intervals superimposed, and the right panel shows the distribution of slip rise time.

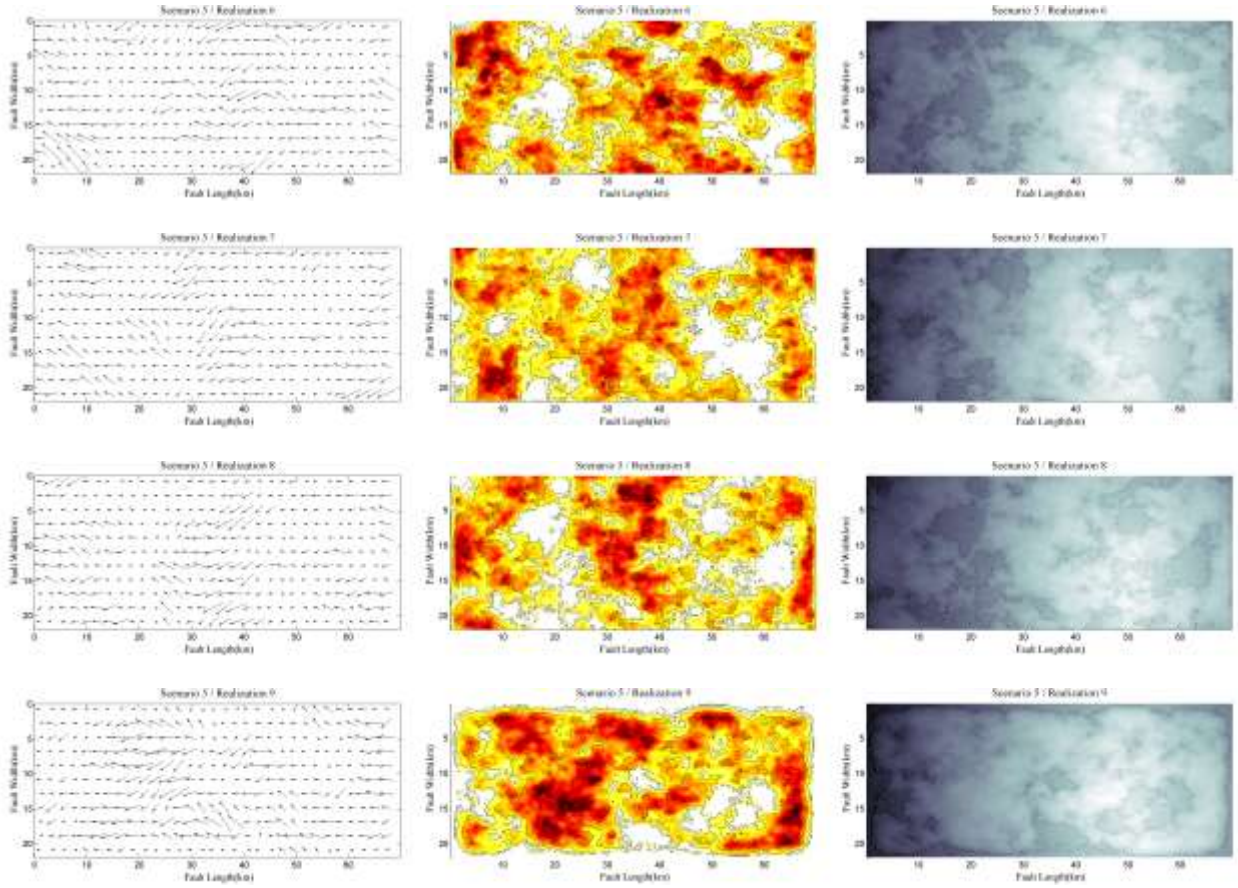

Figure B4. Continued.

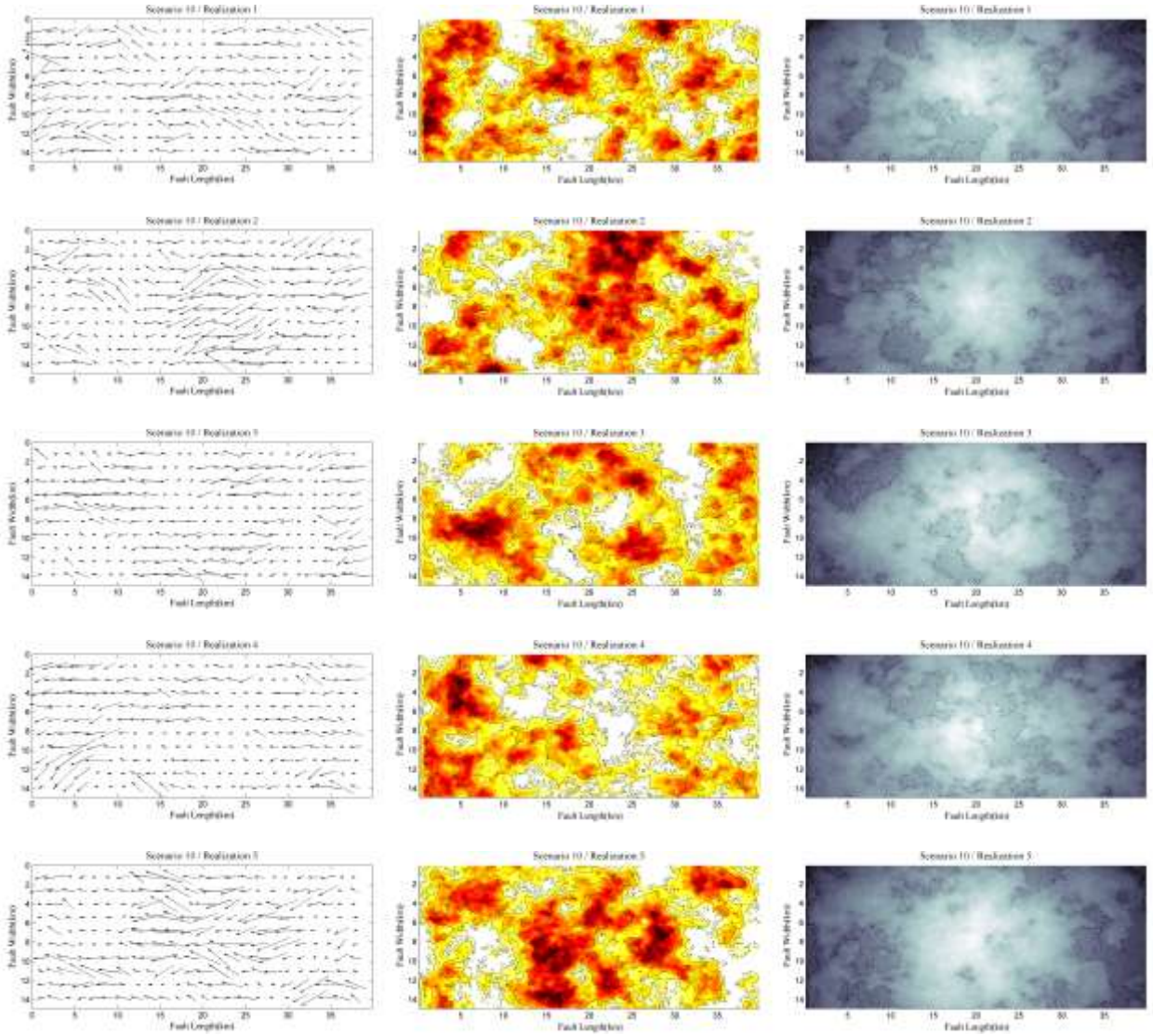

Figure B5. Kinematic rupture model developed for Northern branch of New Madrid fault with M=7.0 (scenario 6). The left panel shows the distribution of average rake angles on each sub-fault over the fault plane. The middle panel shows the slip distribution with rupture front contours at 1 s intervals superimposed, and the right panel shows the distribution of slip rise time.

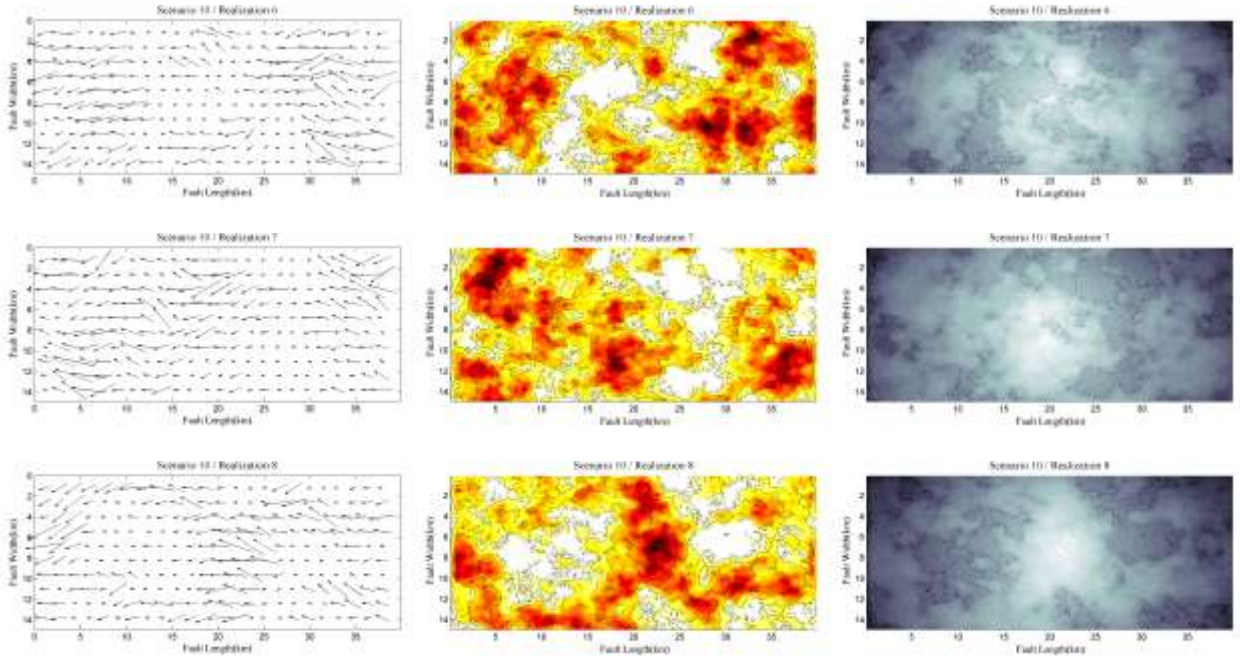

Figure B5. Continued

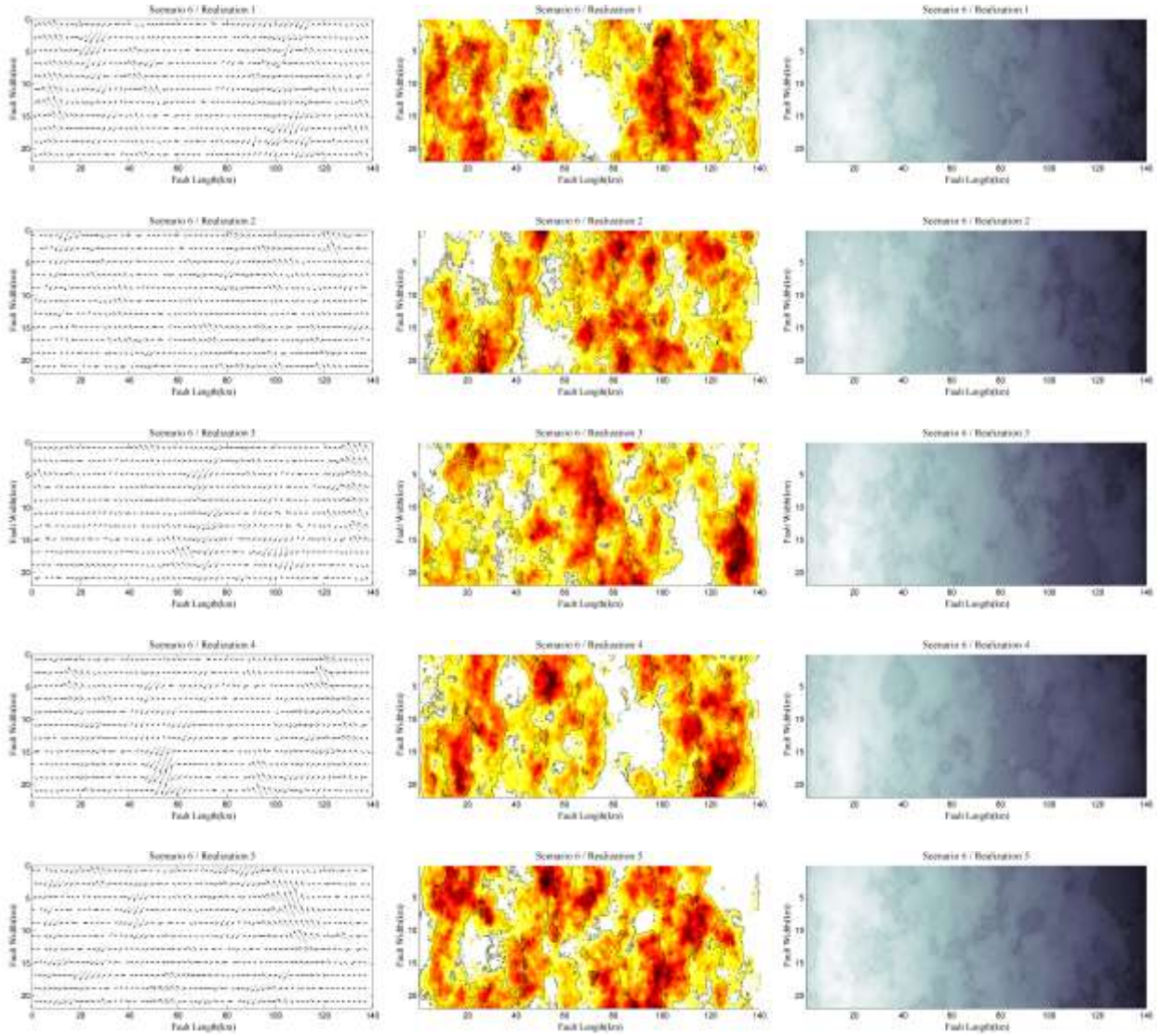

Figure B6. Kinematic rupture model developed for southern branch of New Madrid fault with M=7.7 (scenario 7). The left panel shows the distribution of average rake angles on each sub-fault over the fault plane. The middle panel shows the slip distribution with rupture front contours at 1 s intervals superimposed, and the right panel shows the distribution of slip rise time.

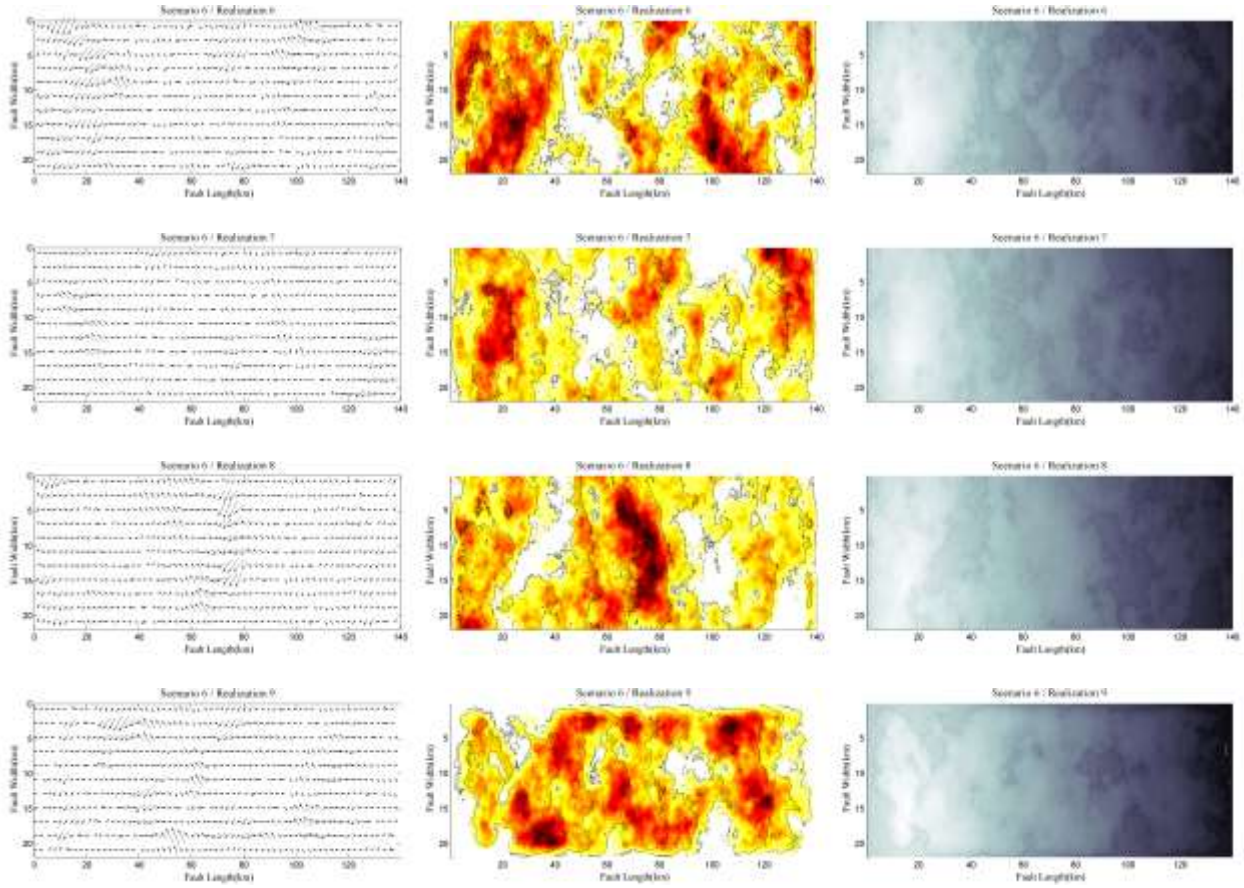

Figure B6. Continued.

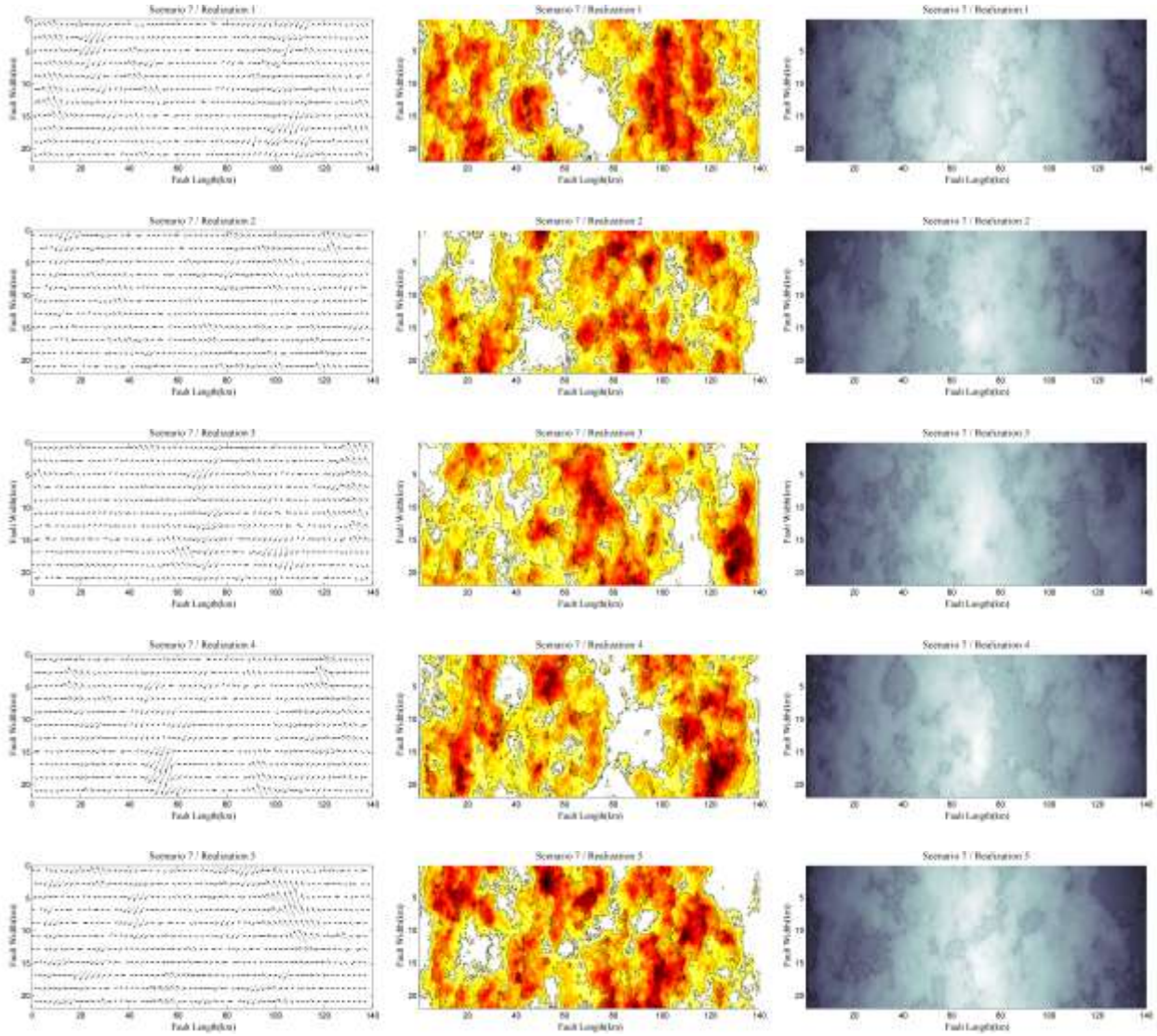

Figure B7. Kinematic rupture model developed for southern branch of New Madrid fault with M=7.7 (scenario 8). The left panel shows the distribution of average rake angles on each sub-fault over the fault plane. The middle panel shows the slip distribution with rupture front contours at 1 s intervals superimposed, and the right panel shows the distribution of slip rise time.

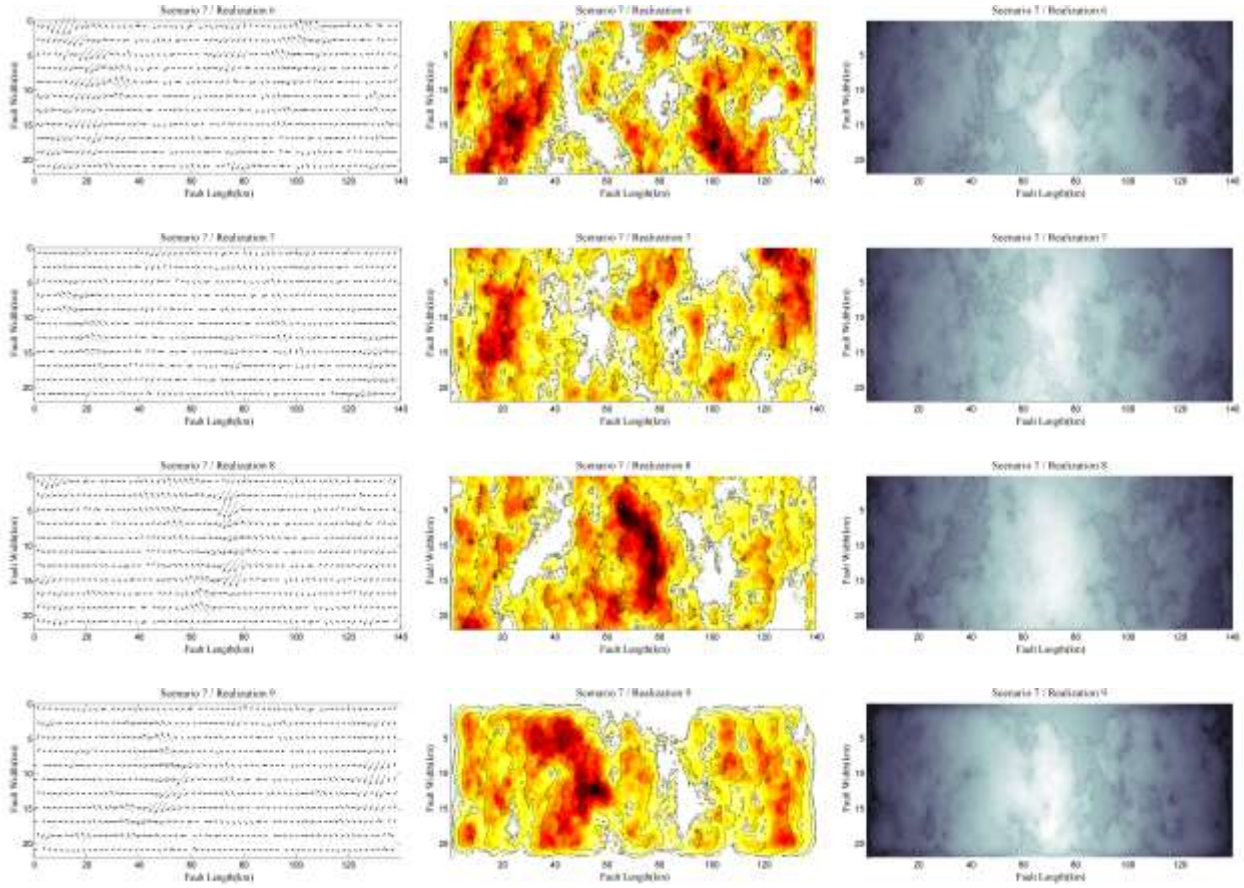

Figure B7. Continued.

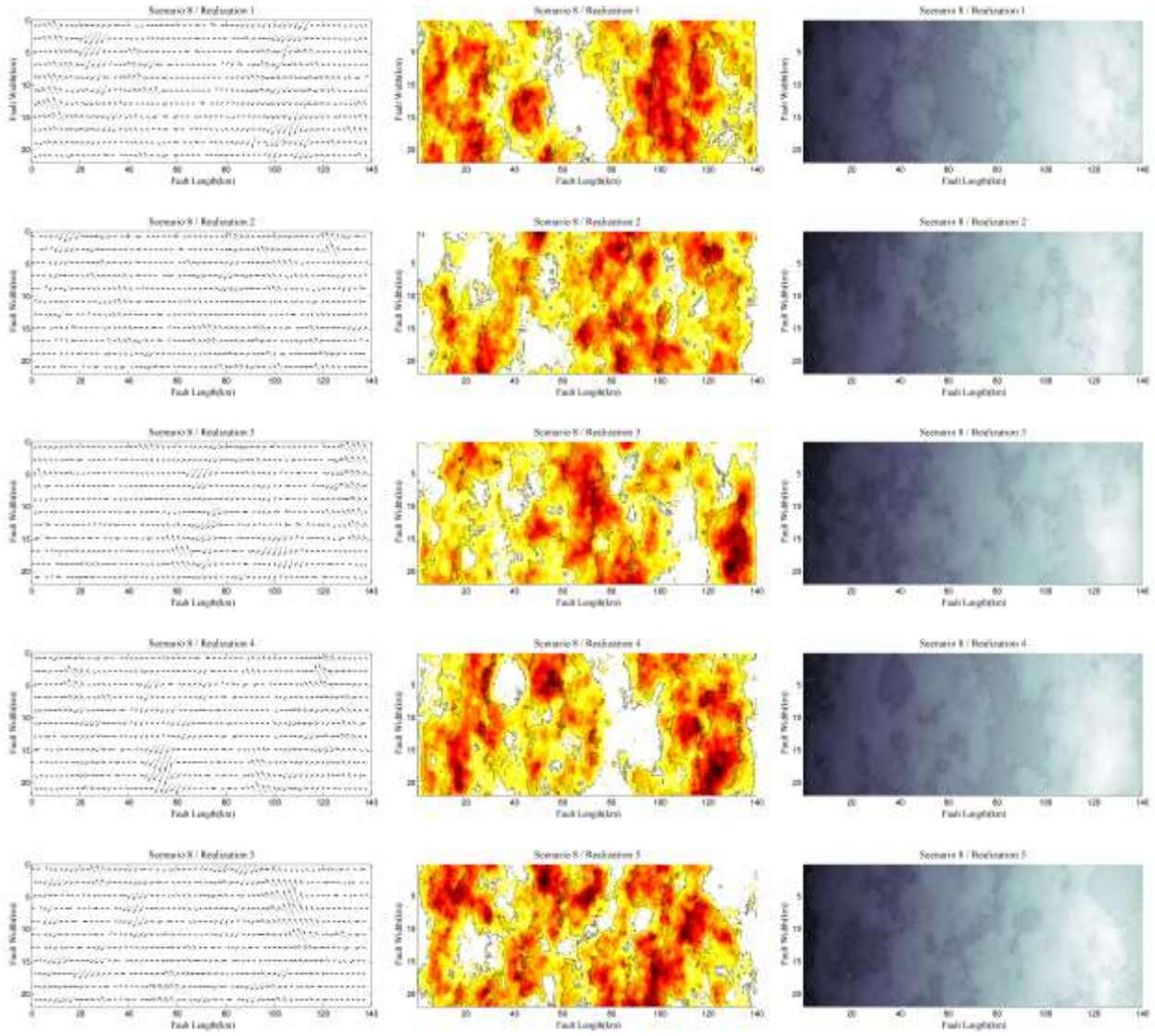

Figure B8. Kinematic rupture model developed for southern branch of New Madrid fault with M=7.7 (scenario 9). The left panel shows the distribution of average rake angles on each sub-fault over the fault plane. The middle panel shows the slip distribution with rupture front contours at 1 s intervals superimposed, and the right panel shows the distribution of slip rise time.

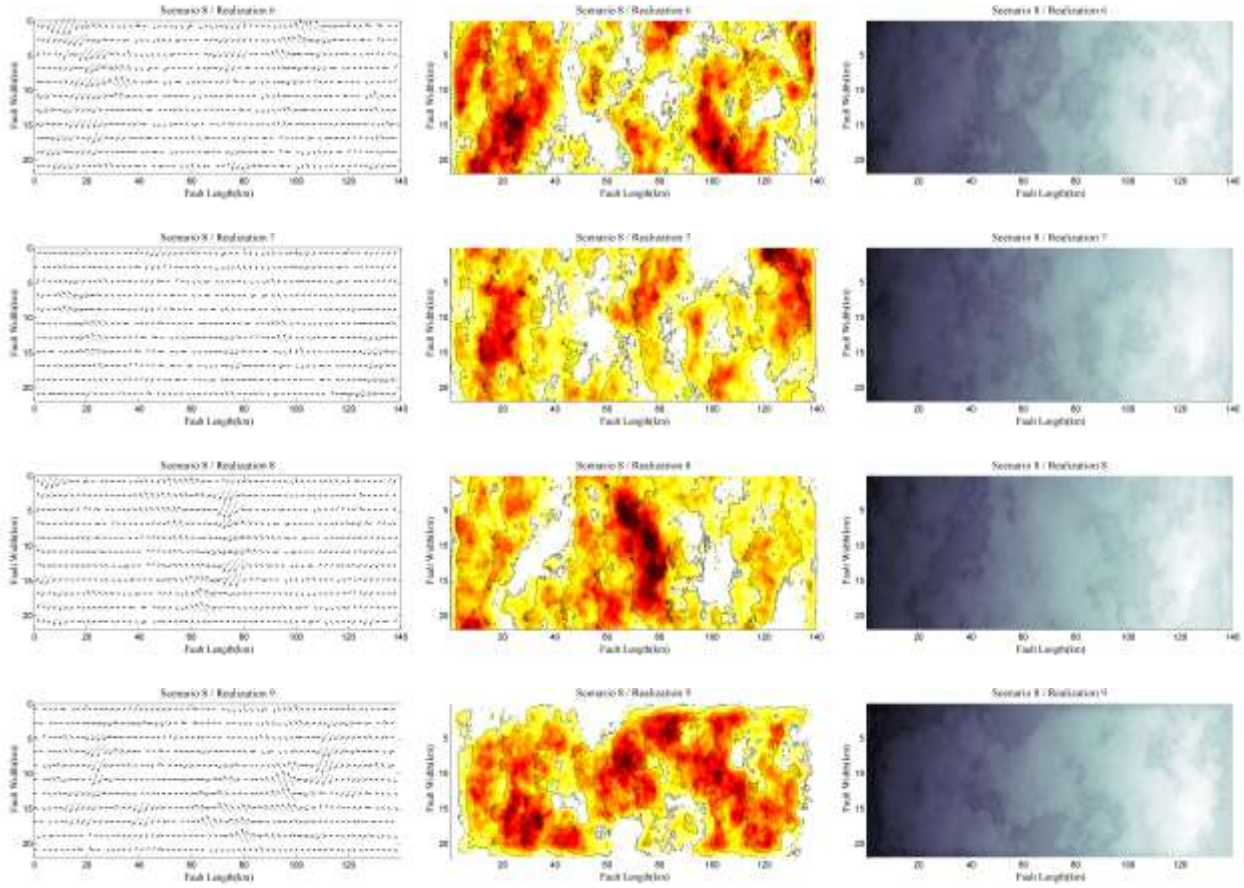

Figure B8. Continued.

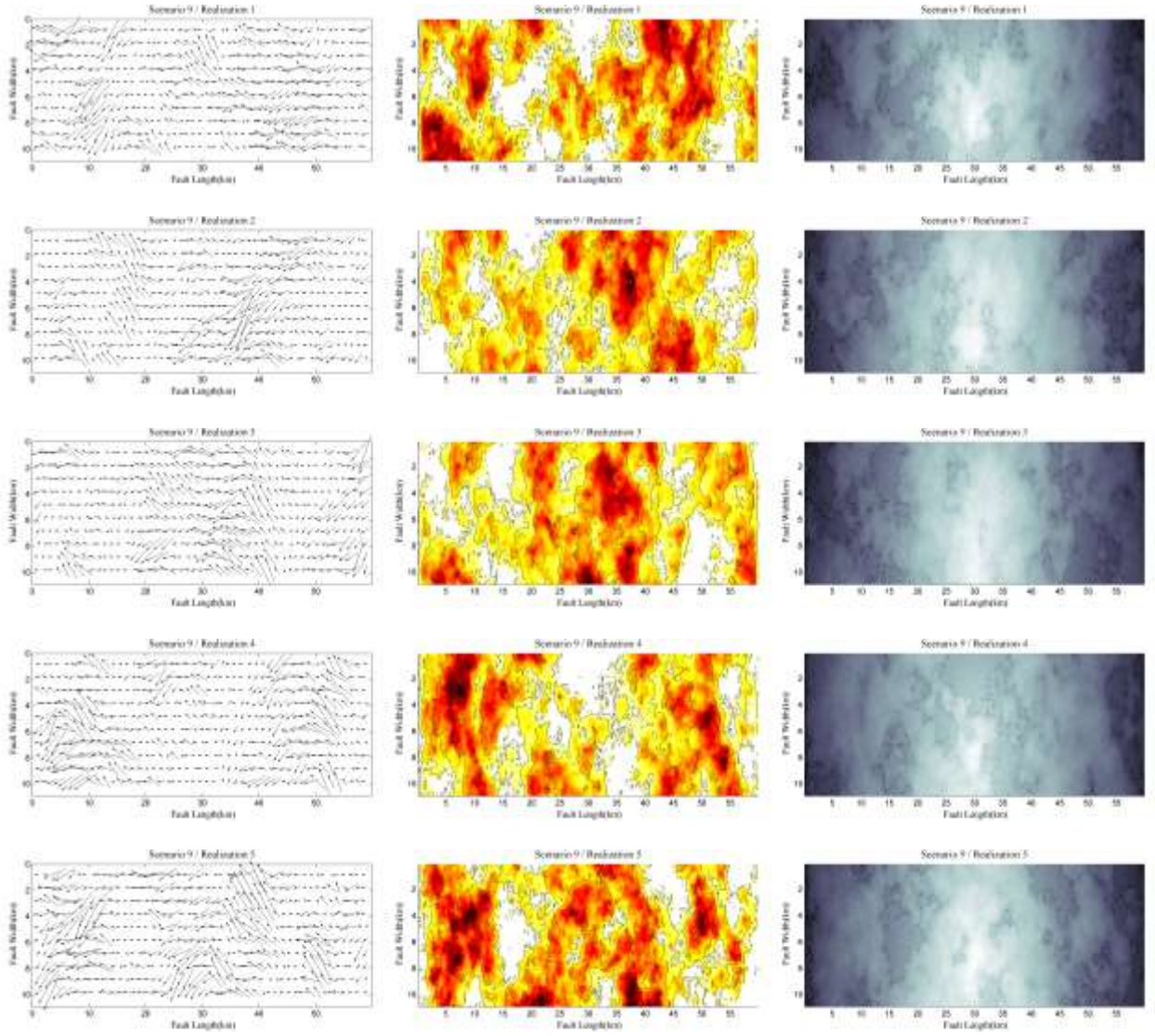

Figure B9. Kinematic rupture model developed for southern branch of New Madrid fault with M=7.0 (scenario 10). The left panel shows the distribution of average rake angles on each sub-fault over the fault plane. The middle panel shows the slip distribution with rupture front contours at 1 s intervals superimposed, and the right panel shows the distribution of slip rise time.

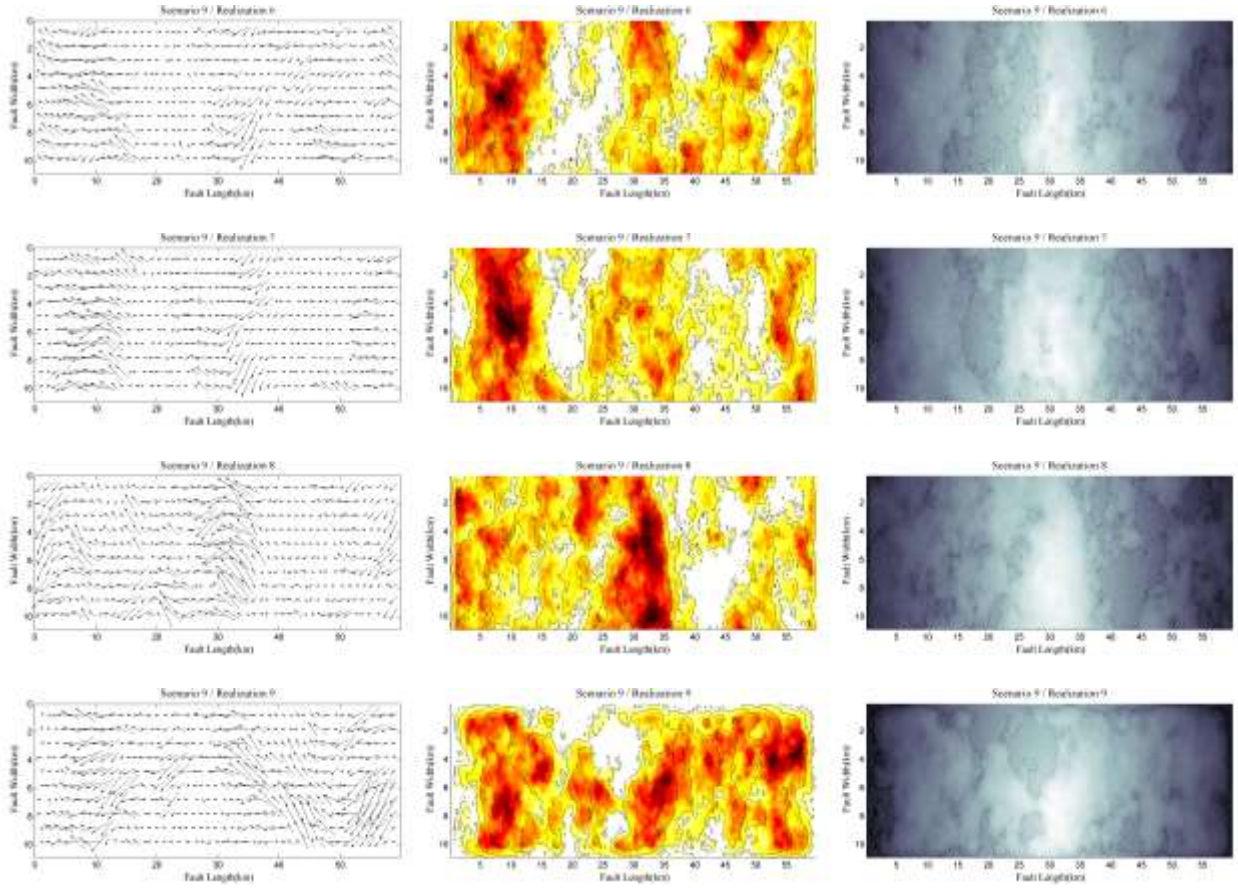

Figure B9. Continued.

Appendix C. Comparison of Estimated MMI Intensities from Simulations with Observations

Even numbered figures show comparison of intensities estimated from simulations with observed intensities, and odd numbered figures show difference residuals between estimated and observed intensities. The figures are shown for each of two GMICE (AK07 and DC11), and for each GMICE there are separate comparisons for intensities estimated from PGA, PGV and response spectral periods at 0.3, 1.0, and 2.0 seconds.

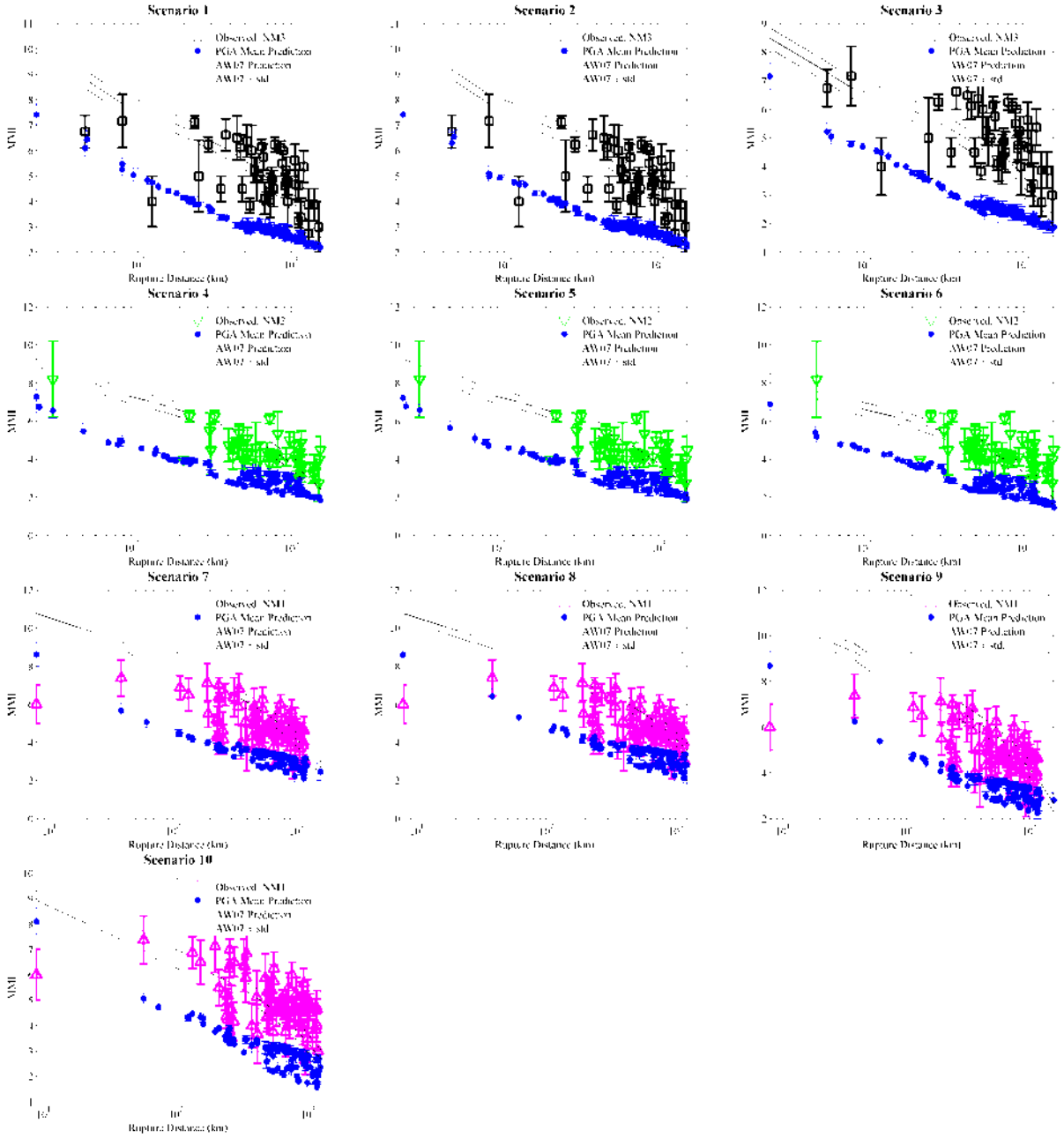

Figure C1. Converted MMI values for Scenarios 1 through 10 using simulated PGAs and the AK07 GMICE where magnitude is considered unknown. The average and one standard deviation of the converted MMI values for the geometric mean of the two horizontal components are calculated at each site over multiple source realizations and shown with filled circle and vertical bars. The empirical MMI values using the AW07 GMPE plus and minus one standard deviation are shown with solid and dashed lines. The observed MMIs for the three New Madrid events are plotted in magenta, green, and black. The vertical bars in the observations correspond to the standard deviation of the average (as interpreted by the four experts) MMI values.

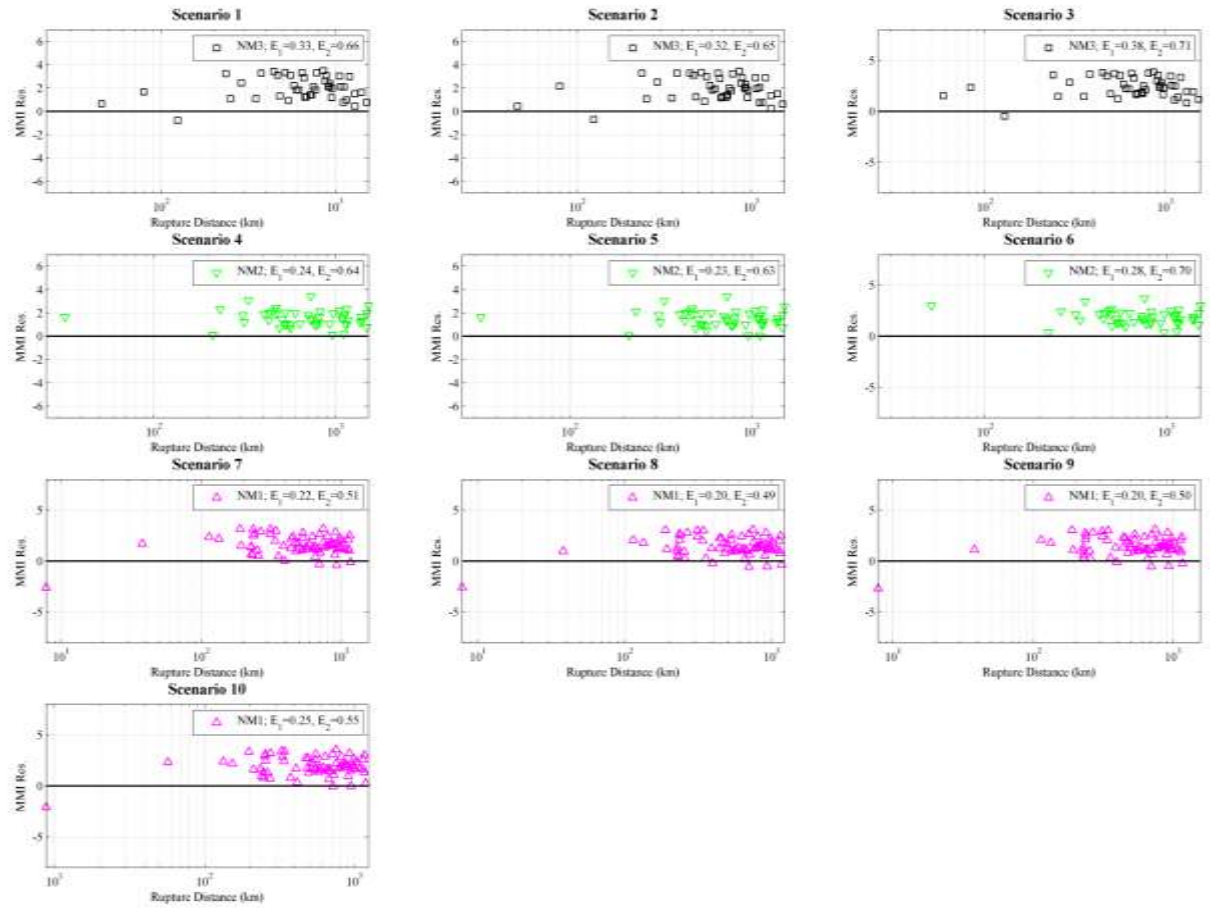

Figure C2. Residuals associated with Figure C1 showing the difference between observed intensities and median predicted ones for NM1, NM2, and NM3 events. The errors listed in the plots legends refer to the root mean square (RMS) error between observed and simulated intensities (E_1), and RMS error between observed intensities and prediction from the AW07 attenuation model (E_2).

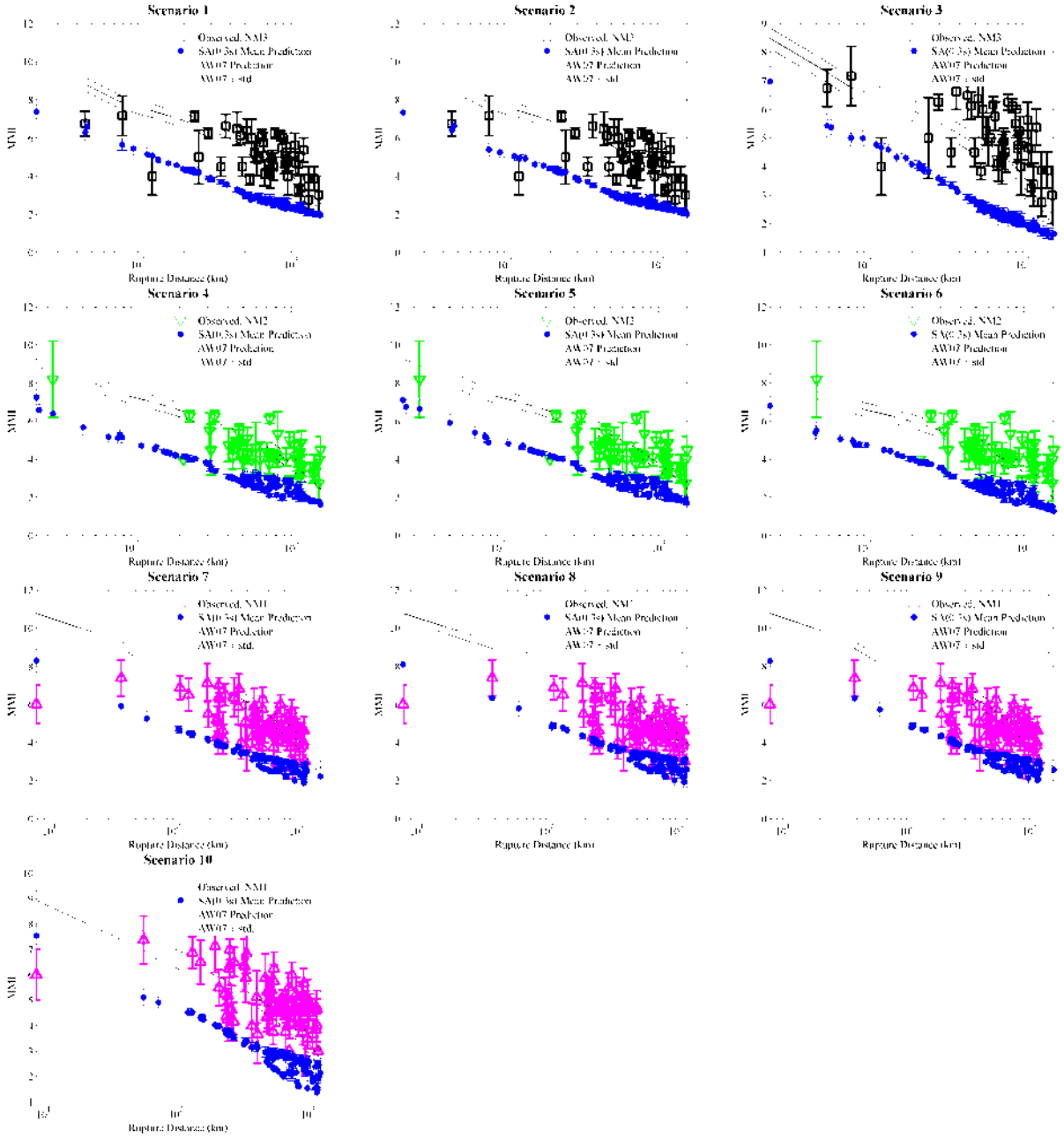

Figure C3. Converted MMI values for Scenarios 1 through 10 using simulated 0.3 sec spectral accelerations and the AK07 GMICE where magnitude is considered unknown. The average and one standard deviation of the converted MMI values for the geometric mean of the two horizontal components are calculated at each site over multiple source realizations and shown with filled circle and vertical bars. The empirical MMI values using the AW07 GMPE plus and minus one standard deviation are shown with solid and dashed lines. The observed MMIs for the three New Madrid events are plotted in magenta, green, and black. The vertical bars in the observations correspond to the standard deviation of the average (as interpreted by the four experts) MMI values.

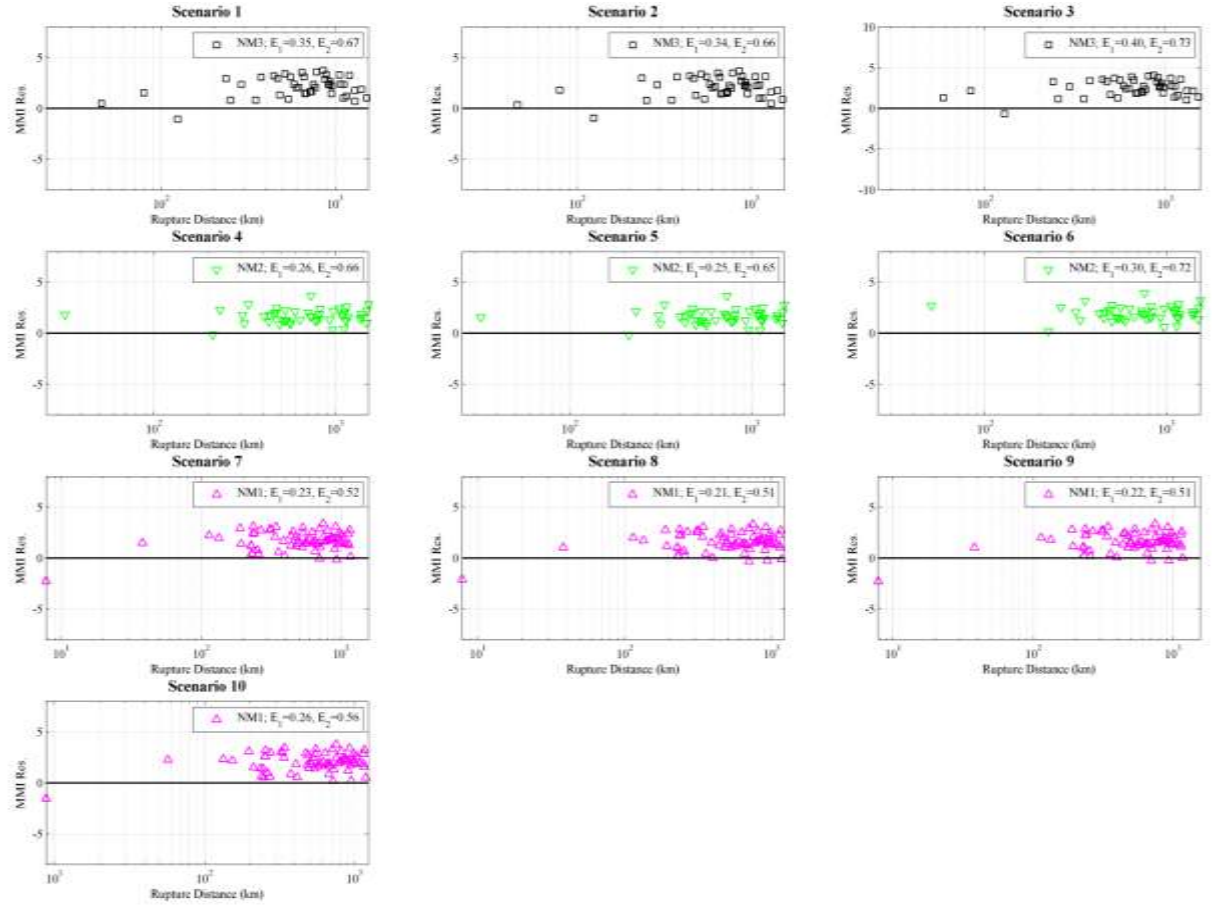

Figure C4. Residuals associated with Figure C3 showing the difference between observed intensities and median predicted ones for NM1, NM2, and NM3 events. The errors listed in the plots legends refer to the root mean square (RMS) error between observed and simulated intensities (E_1), and RMS error between observed intensities and prediction from the AW07 attenuation model (E_2).

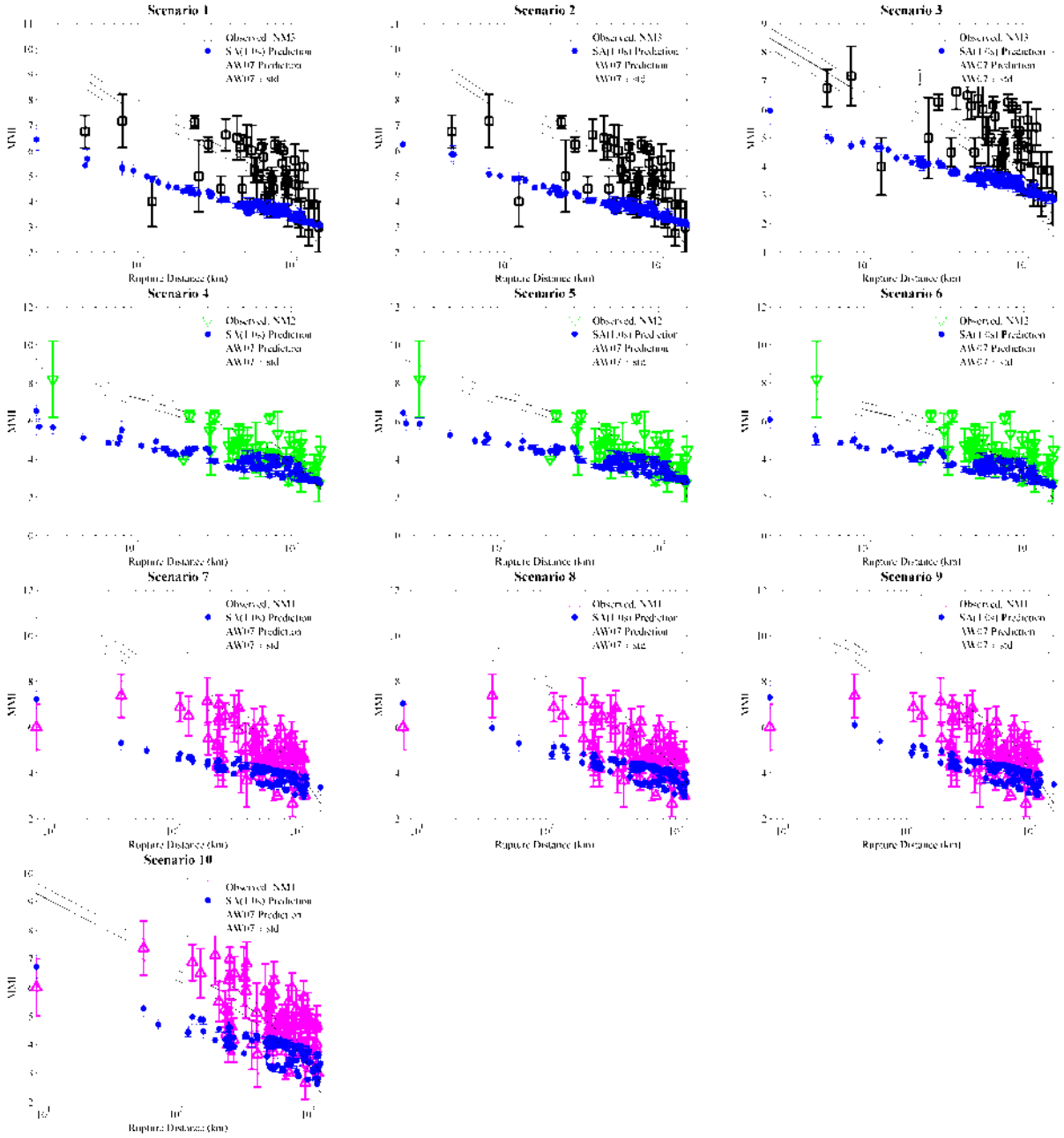

Figure C5. Converted MMI values for Scenarios 1 through 10 using simulated 1.0 s spectral accelerations and the AK07 GMICE where magnitude is considered unknown. The average and one standard deviation of the converted MMI values for the geometric mean of the two horizontal components are calculated at each site over multiple source realizations and shown with filled circle and vertical bars. The empirical MMI values using the AW07 GMPE plus and minus one standard deviation are shown with solid and dashed lines. The observed MMIs for the three New Madrid events are plotted in magenta, green, and black. The vertical bars in the observations correspond to the standard deviation of the average (as interpreted by the four experts) MMI values.

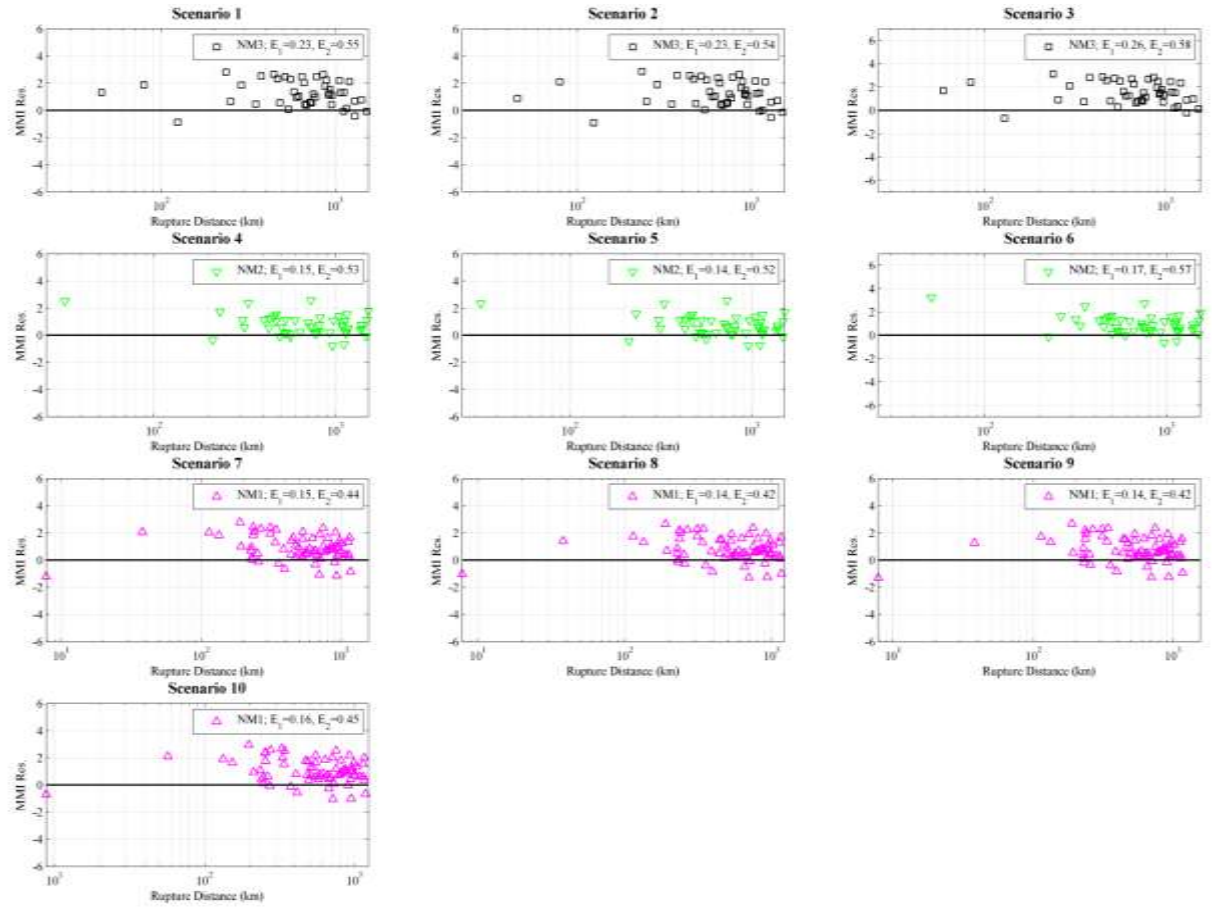

Figure C6. Residuals associated with Figure C5 showing the difference between observed intensities and median predicted ones for NM1, NM2, and NM3 events. The errors listed in the plots legends refer to the root mean square (RMS) error between observed and simulated intensities (E_1), and RMS error between observed intensities and prediction from the AW07 attenuation model (E_2).

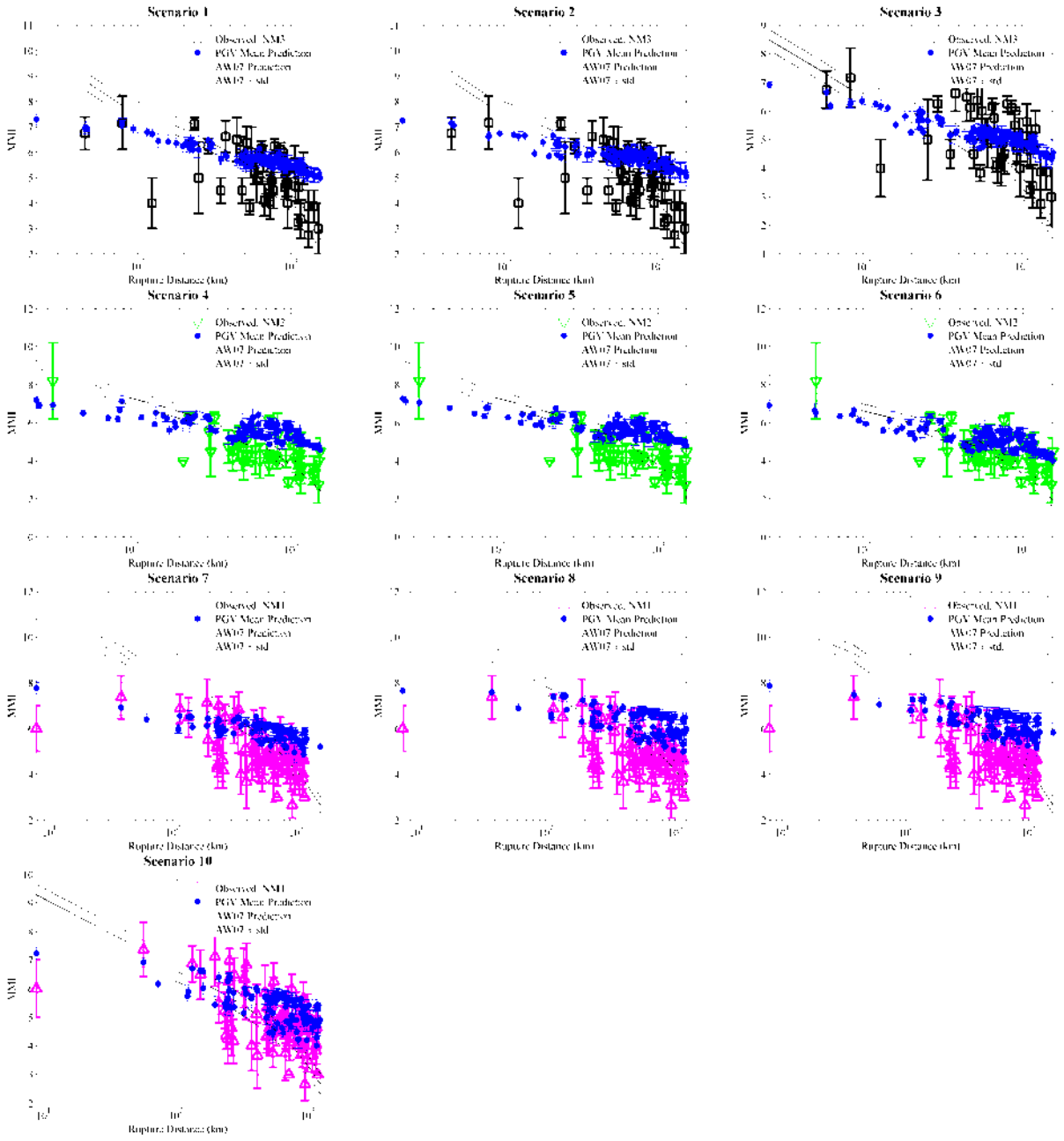

Figure C7. Converted MMI values for Scenarios 1 through 10 using simulated PGVs and the DC11 GMICE. The average and one standard deviation of the converted MMI values for the geometric mean of the two horizontal components are calculated at each site over multiple source realizations and shown with filled circle and vertical bars. The empirical MMI values using the AW07 GMPE plus and minus one standard deviation are shown with solid and dashed lines. The observed MMIs for the three New Madrid events are plotted in magenta, green, and black. The vertical bars in the observations correspond to the standard deviation of the average (as interpreted by the four experts) MMI values.

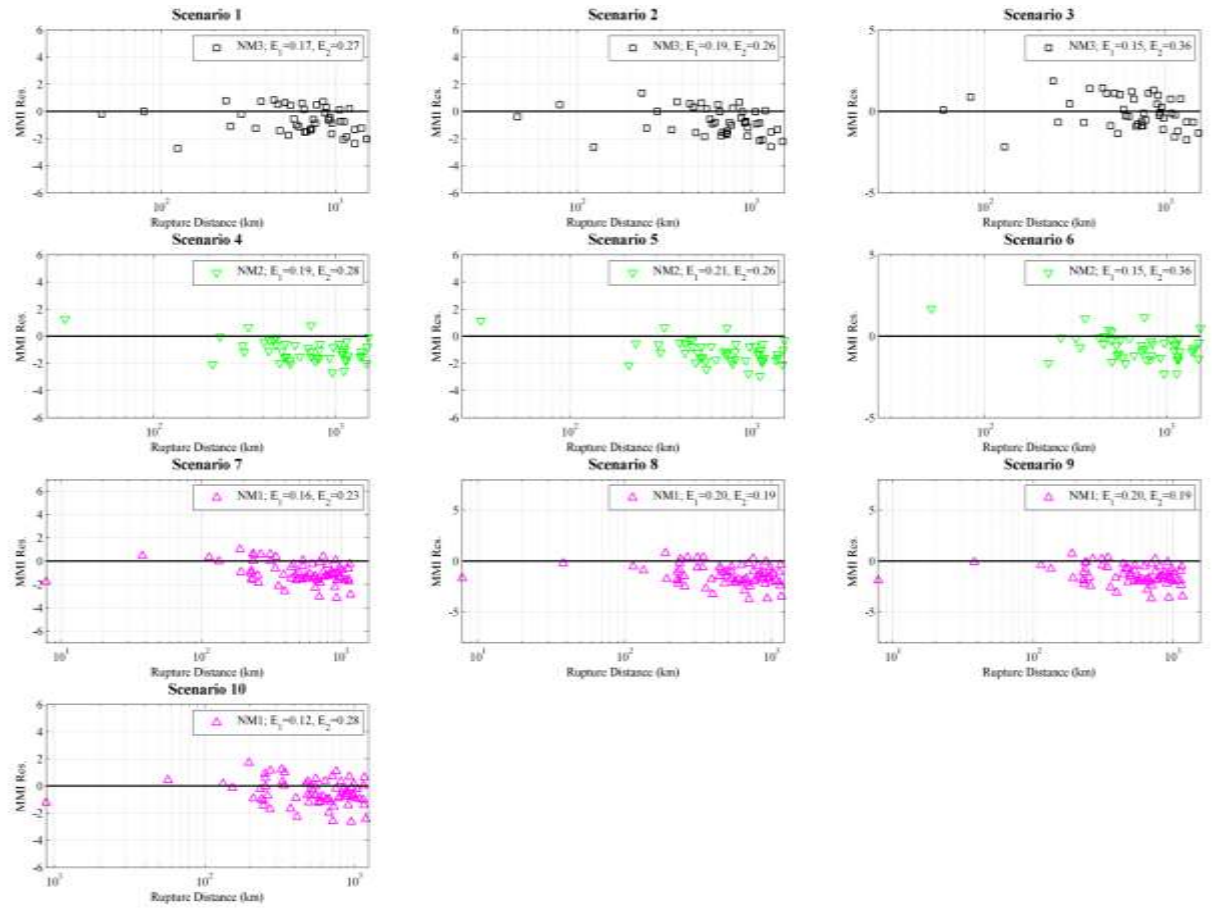

Figure C8. Residuals associated with Figure C7 showing the difference between observed intensities and median predicted ones for NM1, NM2, and NM3 events. The errors listed in the plots legends refer to the root mean square (RMS) error between observed and simulated intensities (E_1), and RMS error between observed intensities and prediction from the AW07 attenuation model (E_2).

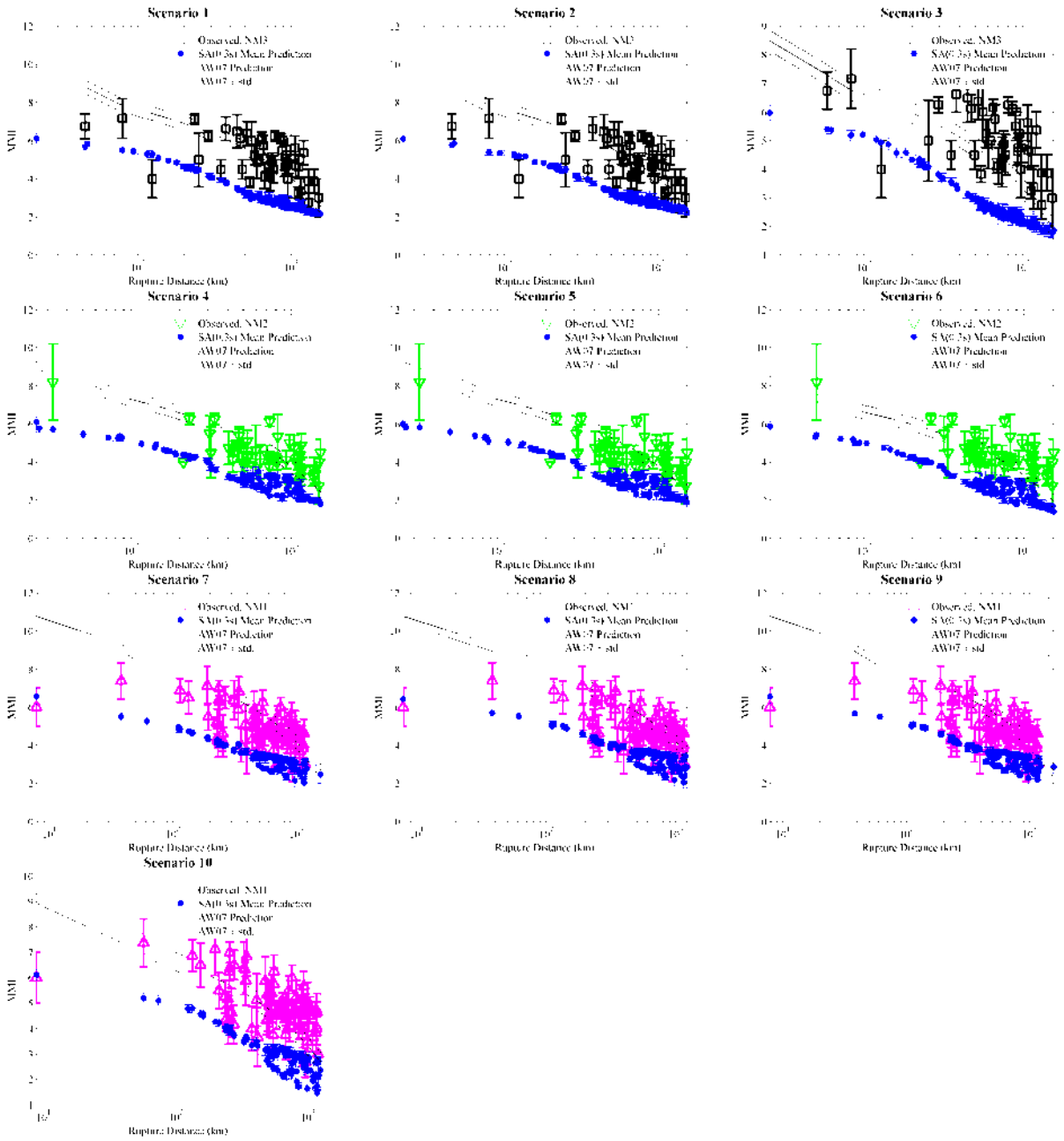

Figure C9. Converted MMI values for Scenarios 1 through 10 using simulated 0.3 s spectral accelerations and the DC11 GMICE. The average and one standard deviation of the converted MMI values for the geometric mean of the two horizontal components are calculated at each site over multiple source realizations and shown with filled circle and vertical bars. The empirical MMI values using the AW07 GMPE plus and minus one standard deviation are shown with solid and dashed lines. The observed MMIs for the three New Madrid events are plotted in magenta, green, and black. The vertical bars in the observations correspond to the standard deviation of the average (as interpreted by the four experts) MMI values.

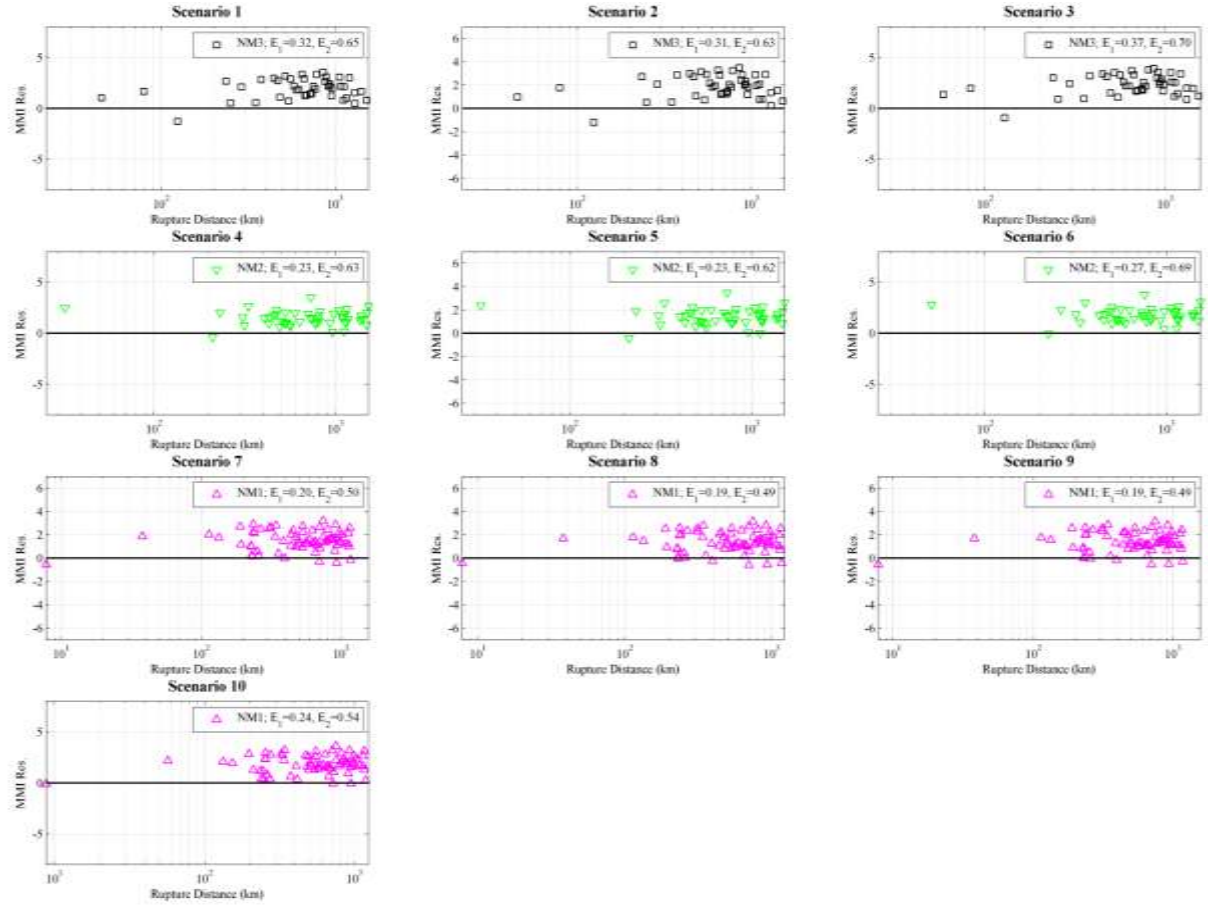

Figure C10. Residuals associated with Figure C9 showing the difference between observed intensities and median predicted ones for NM1, NM2, and NM3 events. The errors listed in the plots legends refer to the root mean square (RMS) error between observed and simulated intensities (E_1), and RMS error between observed intensities and prediction from the AW07 attenuation model (E_2).

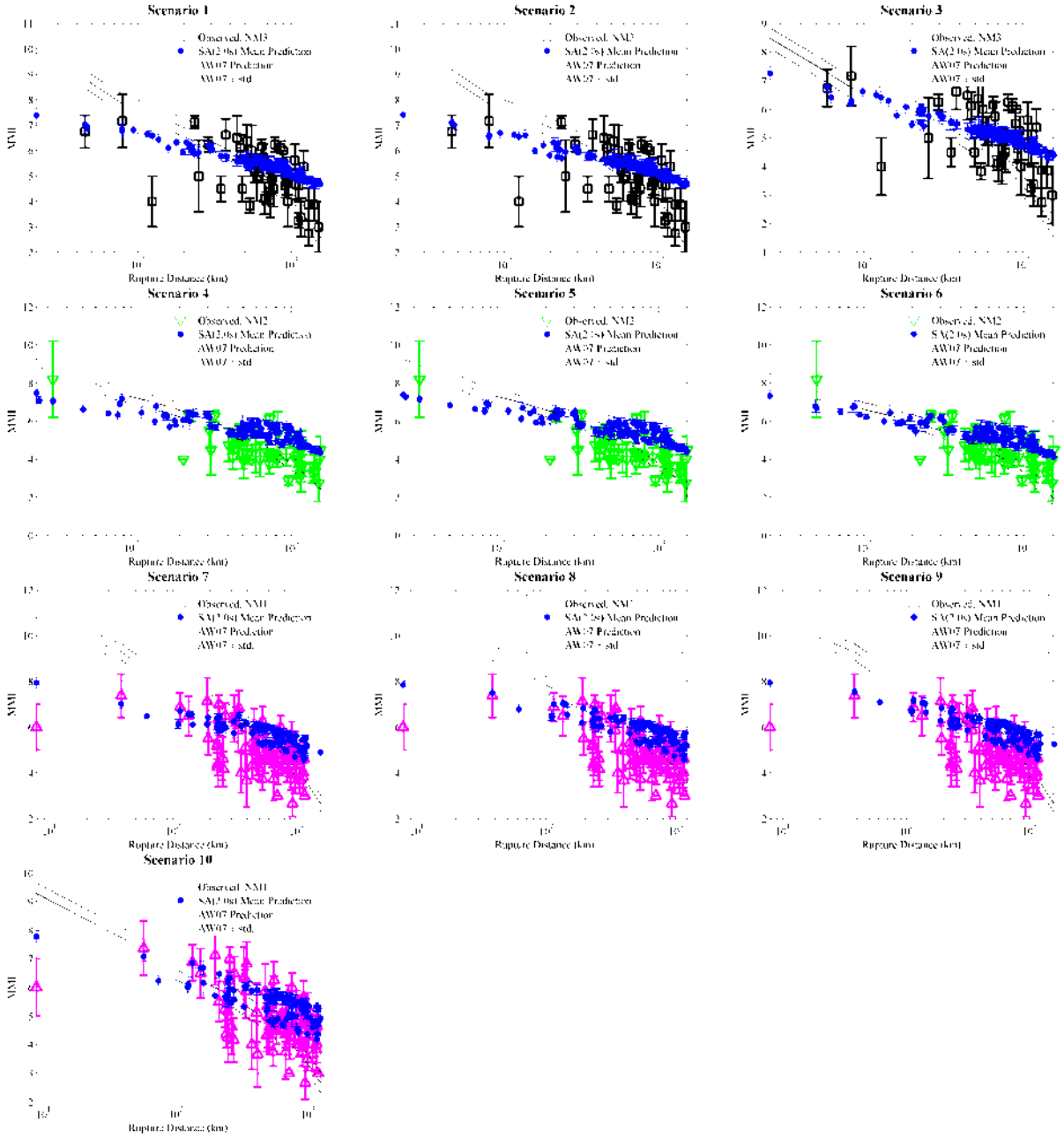

Figure C11. Converted MMI values for Scenarios 1 through 10 using simulated 2.0 s spectral accelerations and the DC11 GMICE. The average and one standard deviation of the converted MMI values for the geometric mean of the two horizontal components are calculated at each site over multiple source realizations and shown with filled circle and vertical bars. The empirical MMI values using the AW07 GMPE plus and minus one standard deviation are shown with solid and dashed lines. The observed MMIs for the three New Madrid events are plotted in magenta, green, and black. The vertical bars in the observations correspond to the standard deviation of the average (as interpreted by the four experts) MMI values.

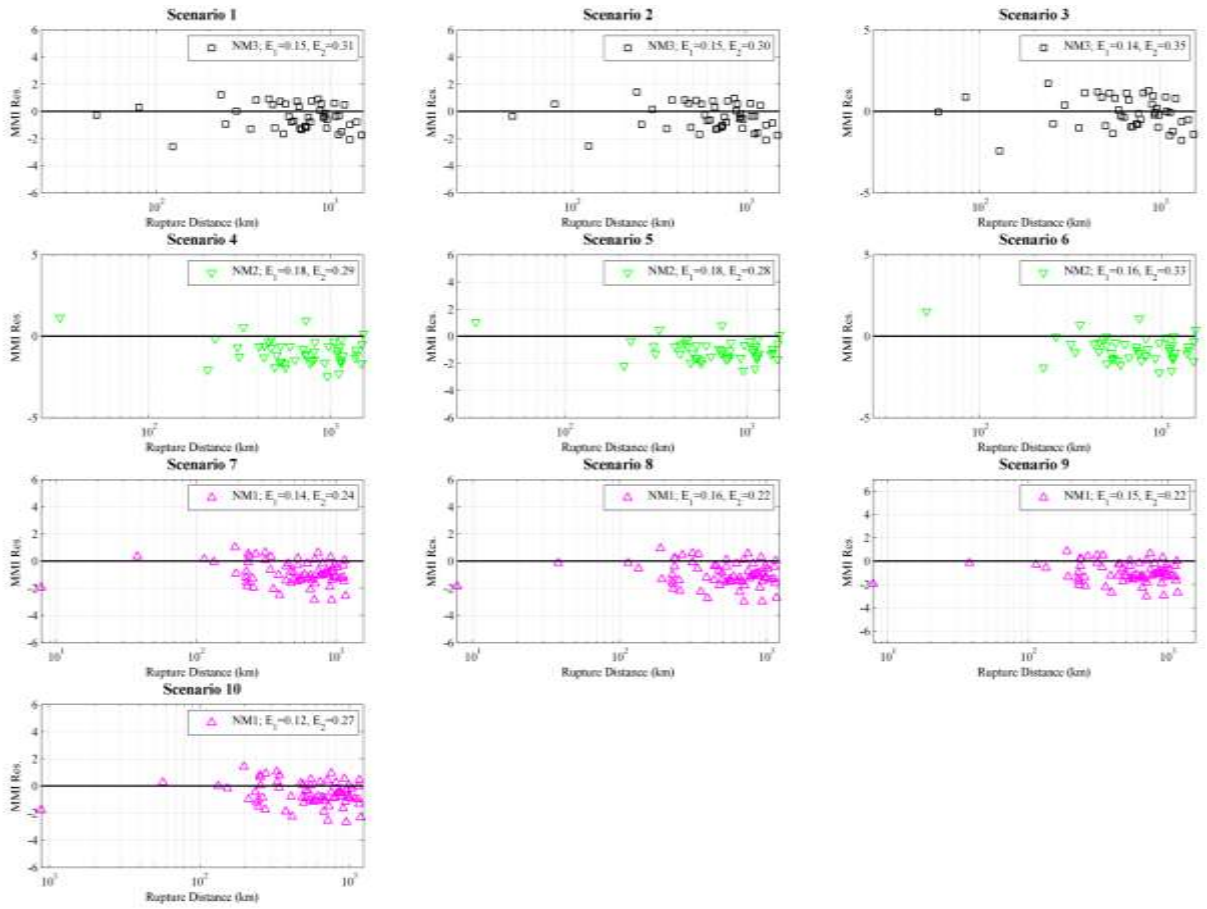

Figure C12. Residuals associated with Figure C11 showing the difference between observed intensities and median predicted ones for NM1, NM2, and NM3 events. The errors listed in the plots legends refer to the root mean square (RMS) error between observed and simulated intensities (E_1), and RMS error between observed intensities and prediction from the AW07 attenuation model (E_2).